6-22-2017

Design and Fabrication of High Performance ZnO/perovskite Nano-array based Monolithic Catalysts for Automotive Emission Control

Sibo Wang
Materials Science & Engineering, University of Connecticut, sibo1314@gmail.com

Design and Fabrication of High Performance ZnO/perovskite Nano-array based Monolithic Catalysts for Automotive Emission Control

Sibo Wang, Ph.D.

University of Connecticut, 2017

Monolithic catalyst, usually composed of honeycomb substrate and wash-coated powder-form catalysts on its channel surface, represents a unique class of functional devices that has been adapted in current industries, particularly in automotive industry as catalytic converters for engine emission aftertreatment purpose. The powder wash-coat based monolithic catalyst lacks well-defined structural configuration in particulate size, shape and distribution, leading to usually compromised materials utilization efficiency and catalytic activity. Thus, it is necessary to develop new generation of high performance monolithic catalysts to meet the increasingly stringent emission regulation. Perovskite materials have been studied as potential candidate of automotive catalysts for decades, with their excellent thermal stability and redox ability allowing them being promising catalysts for heterogeneous catalytic reactions at high temperature. In this dissertation, we introduce design and manufacturing of large-scale high performance ZnO/perovskite nano-array based monolithic catalysts. Detailed discussions are focused on catalytic activity enhancement via rational materials selection and structural manipulation. Noble metal incorporation, acid treatment effect and hydrothermal stability are further studied. The Pt incorporated catalysts exhibit good catalytic performance towards propane oxidation with good hydrothermal stability. The acid treated perovskite nano-array catalysts possess enhanced low temperature activity due to the evolution of nanostructure and surface chemistry. With the successful demonstration of industrially-relevant integration strategy, ZnO/perovskite nano-array catalysts show promise as a new type of monolithic catalysts for automotive emission control.

Design and Fabrication of High Performance ZnO/perovskite Nano-array based Monolithic Catalysts for Automotive Emission Control

Sibo Wang

B.S., Jilin University, 2011

A Dissertation

Submitted in Partial Fulfillment of the

Requirements for the Degree of

Doctor of Philosophy

at the

University of Connecticut

2017

APPROVAL PAGE

Doctor of Philosophy Dissertation

Design and Fabrication of High Performance ZnO/perovskite Nano-array based Monolithic Catalysts for Automotive Emission Control

Presented by

Sibo Wang, B.S.

Major Advisor _____

Puxian Gao

Associate Advisor _____

Brian Willis

Associate Advisor _____

Ramamurthy Ramprasad

Associate Advisor _____

Serge M. Nakhmanson

Associate Advisor _____

Avinash M. Dongare

University of Connecticut

2017

Acknowledgement

With grateful heart, I would like to acknowledge my advisor, Prof. Puxian Gao, who helped me during my Ph.D. education. His expertise, understanding, generous guidance and support made it possible for me to work on a topic that was of great interest to me. It was a pleasure working with him and it was an honor being his student.

I would also thank my associate advisors, Prof. Willis and Prof. Ramprasad for their generous support, valuable comments and insightful criticism.

I am highly and thoroughly grateful to research staff in IMS who ever trained me on operating experiment instruments and the administrative staff who helped me in daily life.

I am grateful to my collaborator Prof. Steven. L. Suib, Ran Miao, Sheng-Yu Chen from Chemistry of UConn for helping me perform the H_2S adsorption test, Prof. Tianfeng Lu and Yunchao Wu from Mechanical Engineering for helping me with the experimental simulation, Dr. Chang-Yong Nam from Brookhaven National Laboratory for helping me prepare sample, Prof. Jun Ding, Wen Xiao from National University of Singapore for helping me do the XPS characterization. I would also like to thank my labmates, Dr. Yanbing. Guo, Dr. Wenxiang Tang, Dr. Shoucheng Du, Dr. Son Hoang, Dr. Zheng Ren, Sanka Piyadasa, Mingwan Zhang, Bo Zhang, Xingxu Lu, Junfei Weng for their generous help and valuable advices in my research.

I would like to express my genuine gratitude to my family- my father, mother, sisters and brothers, particularly my wife, for their support during my life.

Finally, I would like to acknowledge the financial support from U.S. Department of Energy, U.S. National Science Foundation, UConn FEI fellowship and UConn Technology Incubation Program.

University of Connecticut

2017

Table of Contents

Acknowledgement ..... **iv**
Table of Contents ..... **vi**
CHAPTER 1 ..... **1**
Introduction **1**
1.1: Exhaust Aftertreatment System **1**
1.2: Monolithic Catalyst **2**
1.2.1: Structure of Commercial Monolithic Catalyst 2
1.2.2: State-of-the-art coating Process 5
1.3: Introduction of Nano-array based Monolithic Catalyst **8**
1.3.1: 1-D Nanostructures Enhanced Heterogeneous Catalysis 8
1.3.2: Metal Oxides Nano-array Integrated Monolithic Catalyst 9
1.3.3: Materials Selection and Structural Design 11
1.4: Motivation and Background of the Research **12**
1.4.1: Low Temperature Combustion and 150°C Challenge 14
1.4.2: Catalytic Properties of Lanthanum based Perovskite Oxides 16
1.4.3 Role of Defect in Perovskite 18

1.5: Dissertation Objectives 20

CHAPTER 2 24

Experiment and Characterization 24

2.1: Experimental Set-up 25

2.1.1: Substrate and Precursors 25

2.1.2: Hydrothermal Synthesis 26

2.1.3: Perovskite Deposition 27

2.2: Structural Characterization 29

2.2.1: Electron Microscopes 29

2.2.2: X-ray Photoelectron Spectroscopy 31

2.2.3: X-ray Diffraction 32

2.2.4: Temperature Programmed Reduction of H_2 33

2.2.5: Temperature Programmed Desorption of O_2 34

2.3: Catalytic Activity Characterization 35

CHAPTER 3 38

ZnO/perovskite Core/shell Nanorod Array based Monolithic Catalysts for Low Temperature Propane Oxidation 38

3.1: Introduction 38

3.2: Experimental 40

3.2.1: Precursor and Substrate 40

3.2.2: Hydrothermal Synthesis of ZnO Nanorod Array 41

3.2.3: Perovskite Nanofilm Deposition 41

3.3: Result and Discussion 42

3.4: Conclusion 52

CHAPTER 4 56

Pt Loaded ZnO/perovskite Nano-array Catalysts: Enhanced Low Temperature Activity and Hydrothermal Stability 56

4.1: Introduction 56

4.2: Experimental 57

4.2.1: Co-deposition of Perovskite and Platinum Nanoparticles 58

4.2.2: Atomic-Layer-Deposition of Platinum on ZnO/perovskite Nano-array 59

4.3: Result and Discussion 59

4.4: Conclusion 65

CHAPTER 5 67

Enhanced Metallic Nano-Pt Dispersion on Mesoporous Perovskite Nanotube Arrays for Efficient Low Temperature Propane Oxidation 67

5.1: Introduction 67

5.2: Experimental 69

5.2.1: ZnO/$LaMnO_3$-Pt Core/shell Nanorod Array Integration 70

5.2.2: Mesoporous $LaMnO_3$-Pt Nanotube Array Fabrication 71

5.2.3: Catalytic propane oxidation 71

5.3: Result and Discussion 72

5.4: Conclusion 84

CHAPTER 6 ..... **89**
Hydrothermal Based Scalable Continuous Flow Synthesis of ZnO Nanorod Arrays in 3-D Ceramic Honeycomb Substrate **89**
6.1: Introduction **89**
6.2: Experimental **91**
6.2.1: Precursors, Substrate and Setup 91
6.2.2: Hydrothermal based Continuous Flow Synthesis 92
6.2.3: Computational Fluid Dynamic 94
6.3: Result and Discussion **94**
6.4: Conclusion **106**
CHAPTER 7 ..... **109**
Summary and Outlook **109**
7.1. Summary **109**
7.2. Outlook and Suggestion **113**
RESUME **116**
PUBLICATIONS **121**

CHAPTER 1

Introduction

1.1: Exhaust Aftertreatment System

The emission from fuel based internal combustion engines on motor vehicles is composed of multiple toxic components including hydrocarbons (HCs), carbon monoxide (CO), nitrogen oxides (NO_x), particulate matter, sulfur oxides (SO_x), and volatile organic compounds (VOCs), which may contribute to various diseases for human beings and leads to severe environmental issues such as greenhouse effect, acid rain and haze. [1] Thus, exhaust aftertreatment system must be mounted on every vehicle to reduce the emission of toxic gas according to the emission regulation. [2] One of the most important devices in aftertreatment system is catalytic converter which can convert the HCs, CO, NO_x, and particulates to non-toxic gas through a sequence of catalytic reactions over noble metal/metal oxides catalysts. For many vehicles, the catalytic converters are mounted near the engine's exhaust manifold so that they can be heated up quickly to reach their operating temperature (light-off temperature) after the engine ignition. In typical vehicles equipped with catalytic converters, most of the pollution released at tailpipe comes from the first five minutes of engine operation because the converters cannot acquire sufficient heat from engine during this time. However, keeping catalytic converters too close to exhaust manifold leads them to work at very high temperature in most time, which results in gradual deactivation of catalysts inside the converters due to the agglomeration of active sites. Due to the high energy density enabled by fuel based combustion systems which so far cannot be achieved

by alternative technologies, exhaust aftertreatment technology is still be of tremendous significance in energy and environmental fields.[3]

1.2: Monolithic Catalyst

The major device in a catalytic converter is the monolithic catalyst. It is comprised of two components: (1) three-dimensional monolithic honeycomb substrate, and (2) catalyst attached on the channel wall surface of substrate. In this section, we will introduce the commercial monolithic catalyst and the state-of-the-art wash-coating method for fabricating monolithic catalysts.

1.2.1: Structure of Commercial Monolithic Catalyst

Figure 1-1 presents a commercial monolithic cordierite substrate purchased from Corning, Inc.. Such ceramic substrates are obtained through extrusion process. [4] The bulk density is 223 g/L. The surface area is 36.2 m^2/cm^3. The hydraulic diameter (channel diameter) is 0.97 mm. The substrate has multiple straight and parallel channels (600 cell per square inch) traverse the direction of length. The composition of cordierite that has been confirmed by x-ray diffraction is $2MgO{\cdot}2Al_2O_3{\cdot}5SiO_2$. The open frontal area to cross-sectional area is 0.86, which is able to reduce the pressure loss of gas flow through the substrate and minimize the efficiency loss in vehicles. Typical morphology of cordierite revealed by scanning electron microscope (SEM) is a porous structure with pore size ranging from hundreds of nanometers to a few micron meters. The introduction of surface roughness and pores can increase the surface area and facilitate the dispersion of catalysts on such a monolithic support.

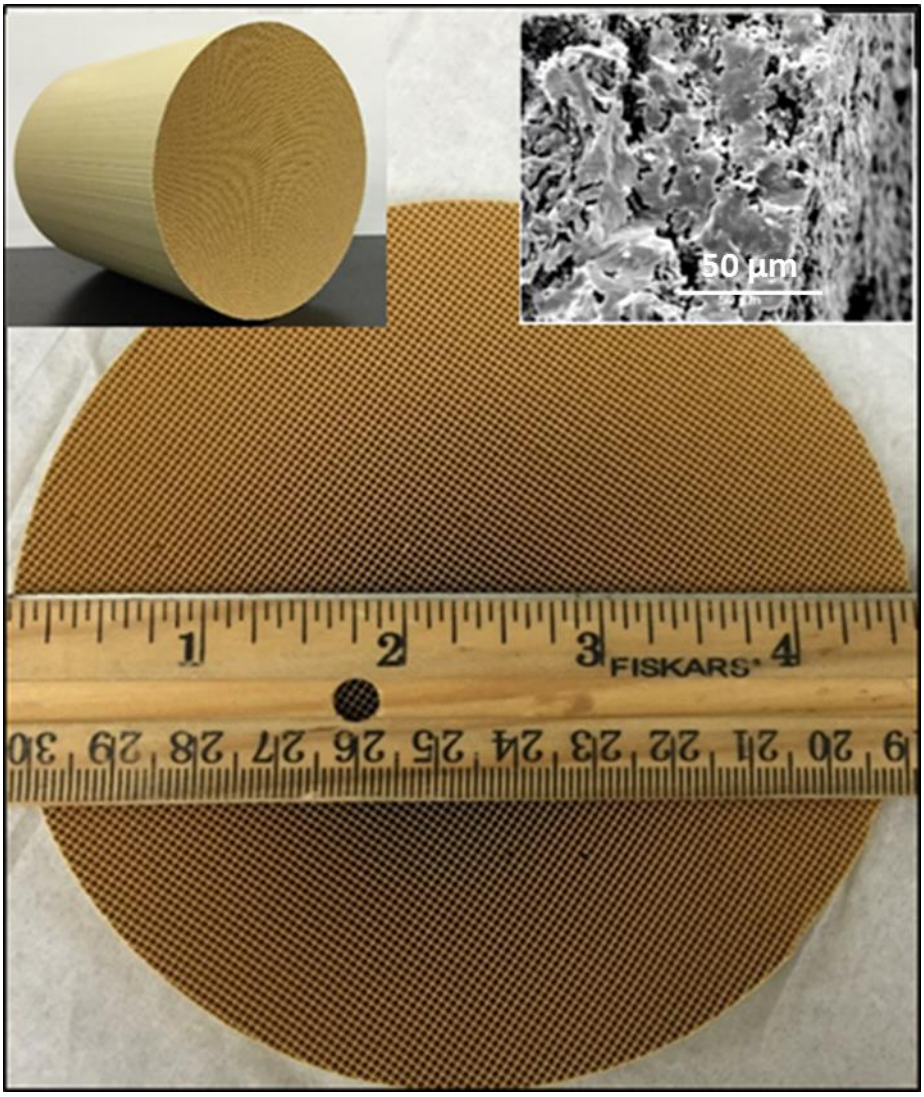

Figure 1-1. Monolithic catalyst support with parallel channels across it. The inset on top-right presents the microstructure of substrate.

The typical morphology of commercial powder-form catalyst on honeycomb substrate is shown in **Figure 1-2**. The side view SEM image clearly presents a layer of catalyst on the internal surface of a channel. The thickness of catalyst ranges from 80 µm up to 250 µm at the corners of channel. At higher magnification, the catalyst is composed of particles with a wide range of diameter. However, dispersing the powder catalyst in water under sonication may split

the particles into much smaller particles. **Figure 1-2 (c)** shows a typical transmission electron microscope image of the powder catalyst which presents large particles that are assembled by a number of crystalline metal and metal oxide nanoparticles. This explains why commercial monolithic catalysts usually possess high surface area (>100 m^2/g). Generally, the powder catalyst is of relatively poor mechanical stability and can be easily removed from honeycomb substrate. However, with the help of binder, it can be immobilized on the substrate surface and bear the pressure variation of gas floww. Traditional powder-form catalyst lacks well-defined geometric configuration that could be preferred for specific crystal planes that are of higher reactivity than the others. On the other hand, the catalytic activity could be compromised due to difficult diffusion of reactants to active sites and poor interaction between gas phase and solid catalysts. The small crystallites may also easily agglomerate due to sintering at high operating temperature, which results in gradual deterioration of catalytic activity. Thus, it is necessary to load more catalyst on monolith to compensate the deactivation in order to guarantee sufficient activity in long-term usage.

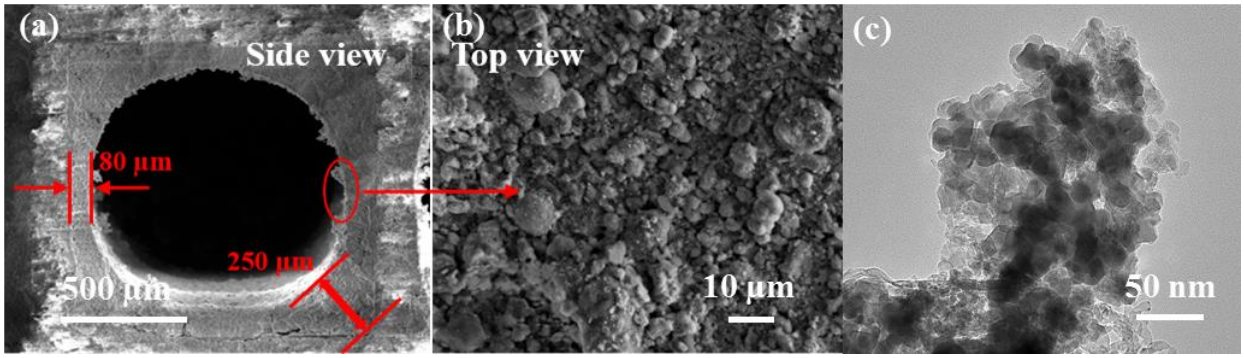

Figure 1-2. (a) side-view and (b) top-view SEM image of powder-form catalyst on the wall surface of honeycomb substrate. (c) Nanostructures revealed by TEM image.

1.2.2: State-of-the-art coating Process

The monolithic catalyst presented in **Figure 1-2 (a)** holds all the catalytically active components on the surface of substrate, making easier diffusion of reactant molecules to the active sites. Preparation of monolithic catalysts is usually carried out through a state-of-the-art slurry coating process. The first step of this process is preparing materials to be coated through wet-mill since the particle size should be controlled comparable to the pore size of substrate (5 μm). Then a slurry is prepared by adding acid to adjust pH between 3 and 4. For most of the monolithic catalysts, a secondary support, which can be either alumina or silica, should be coated together to increase the dispersion of active components. Since the particles with large diameter are difficult to be immobilized on the support, it is necessary to use some binder agent in slurry to strength the binding. In the second step, the monolith is dipped into slurry for 1 minute and then taken out for drying. The excess slurry in channels is usually removed by pressurized air because extra coating can block the channels and lead to pressure drop when the gas flows through the substrate.

The monolith is then drying in air. The detail of drying process has been described by T.A. Nijhuis and presented in **Figure 1-3**. [5] First, the catalyst, support and binder particles all suspend in slurry, then the large particles contact with each other as the liquid vaporizes (**Figure 1-3 (c)**). At last, the binder particles preferentially segregate at the interface between catalyst/support particles by capillary forces. After the drying process, the monolith must go through calcination at around 450°C to obtain a robust coating layer. For same products needing high loading of catalyst, the dip-coating process can be repeated after the monolith becomes dry. However, the second coating may lead to partial loss of catalyst that has been loaded on monolith. Thus, the industrial coating technique tends to minimize the number of coating cycles.

Other dip-coating processes also include colloidal deposition and sol-gel deposition. The basic coating procedures for them are quite similar to slurry coating except for the preparation of coating solution. The sol-gel solution contains the precursors of catalysts/supports other than particles. Both colloidal and sol-gel depositions are usually used in a pore-filling method, which means that the obtained catalysts mainly stay in the pore of substrate other than forming a layer of coating on the surface of substrate. This type of monolithic catalysts has an intact open frontal area and does not reduce the gas flow pressure. However, the loading amount of pore filling method is significantly limited by total pore volume of substrate, making it not suitable for those monolithic catalysts requiring high catalyst loading.

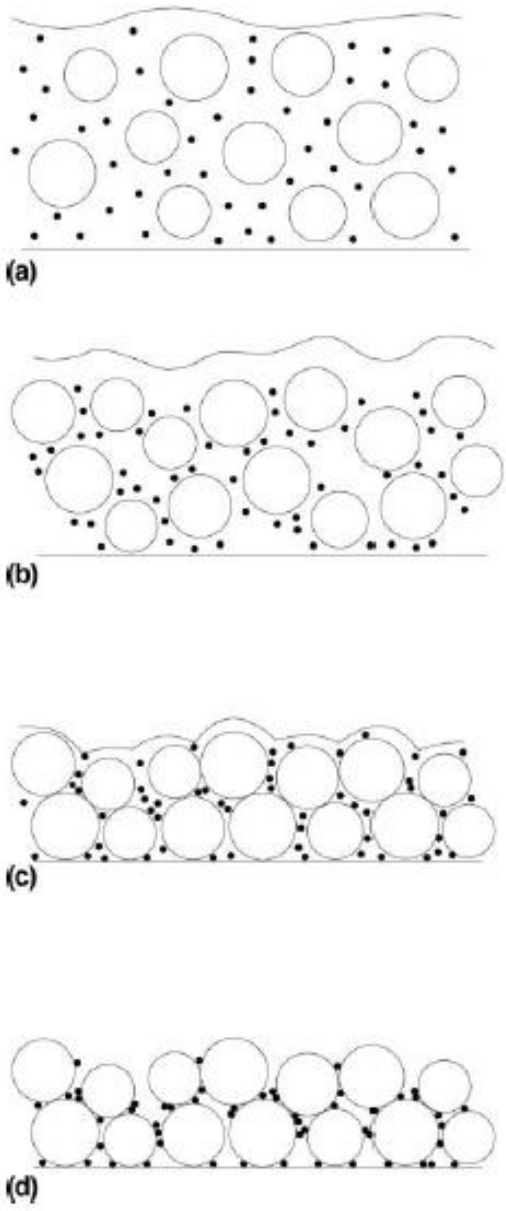

Figure 1-3. Schematic illustration of the drying step in a typical slurry dip-coating process. Large white circles: materials to be coated; black dots: binder. [5]

1.3: Introduction of Nano-array based Monolithic Catalyst

Nanostructures can be classified into 0D (nanoparticles), 1D (nanowires, nanofibers, nanotubes, etc.), 2D (nanofilm, nanopletes, nanodiskettes, etc.) based on the number of dimensions less than 100 nm. Assemblies of nanostructures in a 3-D nano-array configuration with well-defined geometric size, shape and alignment represent a promising technology for meeting the ever-increasing demands of fabricating high-performance devices featuring cost-effectiveness, structural sophistication and multi-functional enabling. In this section, we will focus on 1-D nanostructure array based monolithic catalyst for automotive emission control.

1.3.1: 1-D Nanostructures Enhanced Heterogeneous Catalysis

With the fast development of synthesis techniques, the ever-growing discoveries and improving understandings of new properties of nanostructures, study of nanotechnology has been triggered in a variety of applications including energy conversion and storage, exhaust emission control, environmental sensing and monitoring. 1-D nanostructure can exhibit unique properties in heterogeneous catalysis that are hardly observed in other nanostructures. In light harvesting and energy storage devices, 1-D metal oxide nanostructures have been found to facilitate charge transport along axial direction, shorten the pathways for fast and sufficient ion diffusion with reduced internal resistance. [6, 7, 8] Thus, great effort is being focused on design and fabrication of 1-D nanostructures integrated electrode. Moreover, 1-D nanostructured metal oxides can exhibit enhanced catalytic performance towards reducing toxic gases such as CO oxidation. This enhancement is strongly associated with the better catalytic activity of crystal planes that are preferentially exposed in 1-D nanostructures. For example, CeO_2 nanorod was reported to be more reactive than other nanostructure counterparts toward CO oxidation because of its

predominantly exposed catalytically active crystal planes in {001} {110}. [9] Co_3O_4 nanorods also preferentially expose their {110} plane, which enables the presence of more catalytic active Co^{3+} species on the surface of nanorods. These findings draw great attention on 1-D metal oxides nanostructure in heterogeneous catalysis and demonstrate the importance of morphology control in design of metal oxides based catalysts for efficient automotive emission control.

1.3.2: Metal Oxides Nano-array Integrated Monolithic Catalyst

Fast-forward to the 21st century, the rational assembly of various nanostructural entities into microscale or even macroscale architectures in a well-defined hierarchical fashion is becoming more and more popular. As an example, nanostructure array (nano-array) has become increasingly important in meeting societal demands for nanotechnology. It not only presents a new grand challenge to bring the scientific discovery to realistic societal implications, but also builds up a usable platform collectively implemented by assembly of functional nanostructural components. These nanoscale architectural assemblies allow us fully utilizing their unique technological advantages such as metal-support interaction at interface, [10] fast electron transport properties in optoelectronics [11, 12] and high surface area in environmental remediation. [13, 14] The monolithic devices enabled by 1-D nanostructure assembly have been suggested to reduce the agglomeration of active sites, which improves the spatial utilization efficiency in a confined space. It thus offers greater chance of interaction between the active surface of nano-array and the target phases such as toxic gas and organic pollutant in a heterogeneous catalytic reaction [15] or electrolyte in energy conversion system. [16] By using different metal salt precursors and tuning the growth conditions, ZnO nanorod array, TiO_2 nanorod array, CeO_2 nanotube array, and Co_3O_4 nanowire array can be cost-effectively integrated on the wall surface of 3-D honeycomb

substrate featuring impressive high surface area, thermal stability and mechanical robustness. The low temperature hydrothermal integration strategy is able to manipulate nano-array's size, shape, structure and thus the tailored multifunctional catalytic performance towards exhaust emission control. From the catalytic gas reaction viewpoint, densely-packed nano-array catalysts with ordered macropores between individual nanostructures provide a shorter diffusion pathway and thus improved gas–solid phase interaction. For example, Guo et.al. demonstrated that replacing the wash-coated power-form catalysts with integrated nano-array catalysts on commercialized honeycomb substrate is able to significantly improve the surface area and spatial usage, reduce the agglomeration of catalytic active phase and enhance the materials utilization efficiency. [17] Moreover, when hierarchically decorated with functional components or properly doped with other transition metals into the structure lattice, nano-array catalysts are able to exhibit enhanced catalytic performance. For example, Ren reported that a series of spinel $M_xCo_{3-x}O4$ (M = Co, Ni, Zn) nano-array catalysts have been monolithically integrated on 3-D honeycomb substrate via the low temperature hydrothermal approach. [18, 19] These monolithic nano-array catalysts demonstrated significantly enhanced catalytic performance towards hydrocarbon combustion. Interestingly, doping of Ni into Co_3O_4 nano-array was discovered to promote the activity of lattice oxygen and the formation of catalytically favorable but less thermally stable carbonate species on the surface, which are responsible for the enhanced reaction kinetics. From the industrial manufacturing perspective, the effective self-assembly of nano-array without usage of binders and avoiding multiple coating processes can significantly lower the cost of large-scale manufacturing, which provides a potentially promising route for cost-effective and scalable manufacturing. Therefore, 3-D metal oxides nano-array integration puts forth a new strategy to design high performance catalysts for automotive emission control.

1.3.3: Materials Selection and Structural Design

The performance of nano-array integrated devices is intimately correlated with a variety of factors such as device substrate selection, nanostructure composition and dimensions, and geometrical distribution of nanoarchitecture(s). Therefore, towards further improved the performance of monolithic nano-array catalysts with ultrahigh efficiency, long service lifetime and function diversity, the most adopted strategies in recent decades can be classified into three categories: (1) proper screen and selection of material based on appropriate physical/chemical properties for optimized functions and performance; (2) combination of multiple material components to enable unexpected but enhanced functional performance and explore possible synergistic effects; (3) design of sophisticated hierarchical structures using either similar or dissimilar nanoscale building blocks of precisely controlled geometry and dimensionality to realize possible functionality optimization. As presented in **Figure 1-4**, versatile synthetic approaches of nano-array provide an essential platform comprising a three-fold diversity in material, component and structure. This versatile diversity allows for design of high performance functional nano-array based monolithic catalysts aiming at high-efficiency and sustained catalytic exhaust aftertreament.

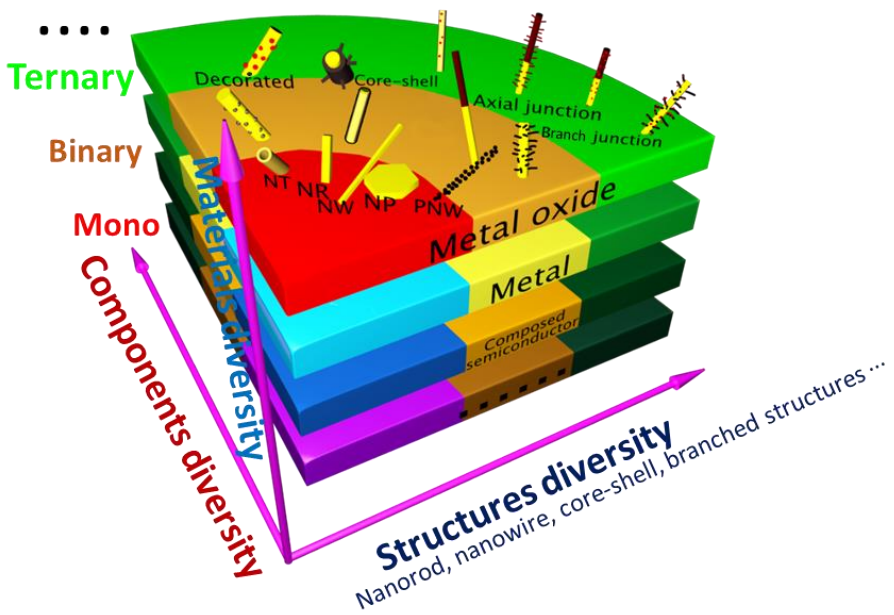

Figure 1-4. A platform illustration for designing nano-array integrated monolithic catalysts

1.4: Motivation and Background of the Research

As more increasingly stringent emission regulations are being implemented globally, it is necessary to design compatible monolithic catalysts with improved catalytic performance. While pursuing energy efficiency and critical materials saving, as well as environmental pollution control, the green and fuel-efficient low temperature combustion (LTC) technology represents a promising approach to be adopted as an upcoming solution. [20, 21] This, however, is in need of a compatible catalytic aftertreatment technology that can address the lack of low temperature catalytic activity in commercially available catalysts during cold start of automotive engines. As the core part of catalytic converter, the state-of-the-art wash-coating based monolithic catalysts are used in current automotive industry. Monolithic catalysts are usually fabricated by depositing catalytically active metal oxides and noble metals nanoparticles (e.g., Pt, Rh, Pd) on uniformly

dispersed Al_2O_3 or SiO_2 support to achieve a mechanically stable coating on the channel surfaces of honeycomb substrate. [22] However, these traditional monolithic catalysts are lack of well-defined microstructure configurations in particular size, shape and distribution, leading to usually compromised dispersion of active components and catalytic activity. In addition, the inevitable activity deterioration due to sintering effect requires a high material usage in support, binder and catalysts to guarantee a long-term functional stability of catalytic converter in exhaust stream. This undoubtedly lowers the materials utilization efficiency and increases the cost. Recently, our research group has invented and developed a new alternative to the wash-coating catalytic converter technology, namely metal oxide nano-array based monolithic catalysts. Our work has shown their potential as the next generation high-efficiency monolithic catalysts featuring enhanced gas-solid phases interactions, catalytic performance and stability, as well as low materials usage.[17, 18] However, the origin of enhanced catalytic activity in nano-array catalysts remains unknown, and more effort should be contributed to the scientific understanding of the correlation between structure of catalysts and the catalytic activity. In addition, is the low temperature activity of nano-array catalysts able to increase while precious group metals (PGM) usage reduces at the same time? Furthermore, the challenging scalable manufacturing of nano-array catalysts holds the promise to bridge the laboratory demonstration to industrial-relevant application. To face these challenges, it is urgent to design new generation nano-array based monolithic catalysts in aftertreament system with the purposes of enhancing the catalytic activity at low temperature and improving the materials utilization efficiency.

1.4.1: Low Temperature Combustion and 150°C Challenge

As important power source for automobiles, diesel engine combustion features fuel economy and low emission of CO_2. However, diesel engine gives a high emission of particulate matters (PM) and NO_x, which are responsible for the environmental issues such as smoky haze and acid rain. Therefore, the emission standards of PM and NO_x are becoming progressively stringent in Europe and United States. Since the energy density provided by diesel engine cannot be reached by other alternatives, developing green combustion process comes to first priority in order to meet the lower emission limits. [23] Low temperature combustion (LTC) technologies including homogeneous charge compression ignition (HCCI) combustion and premixed charge compression ignition (PCCI) combustion are being widely studied in diesel engine combustion. [24] Shown in **Figure 1-5** is a plot of local equivalence ratio vs. flame temperature for different combustion mechanisms. [25] Soot abundant regime is located in fuel-rich zone while NO_x abundant regime is in higher flame temperature range. Conventional diesel engine combustion shows a tradeoff between soot formation and NO_x release. However, the LTC takes place in low equivalence ratio regime to avoid the formation of soot and in low flame temperature to circumvent formation of NO_x.

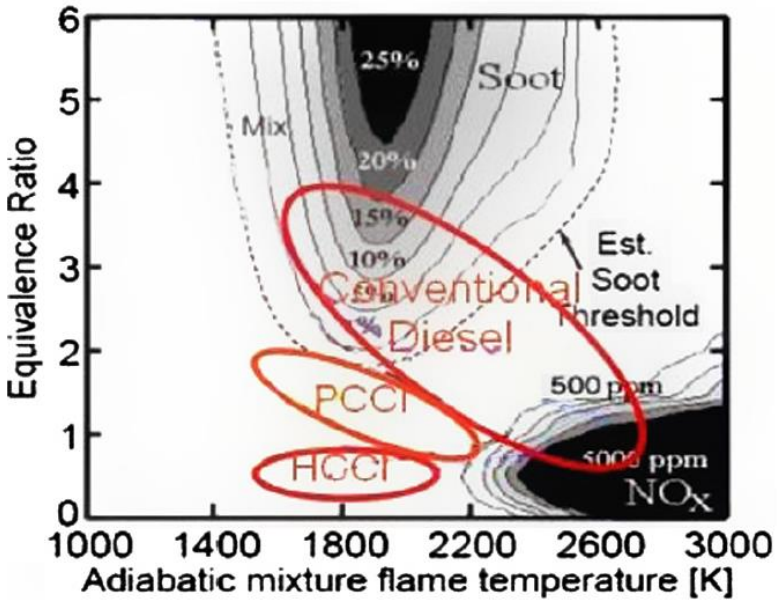

Figure 1-5. Plot of local equivalence ratio vs. flame temperature in low temperature combustion [24]

Generally, the LTC utilizes a more homogeneous fuel-air mixture to reduce the PM and NO_x formation, which, at the same time, gives rise to higher emission of CO and NMOG (non-methane organic gas). The lower flame temperature in the engine cylinder also leads to a lower exhaust temperature, which requires the aftertreatment system to operate at low temperature for CO and NMOG oxidation since the activation energy for catalyst usually comes from exhaust's heat. At the beginning of engine ignition, vehicle must undergo a cold start in which the temperature of monolithic catalyst rapidly ramps from room temperature to light-off temperature (50% conversion of exhaust). During this step, the emissions are responsible for major contributor to the total emissions over the entire drive cycle. Therefore, to meet the challenge posed by advanced LTC technology, it is necessary to develop compatible catalysts which can work at low temperature for CO and hydrocarbons (HCs) oxidation. US DRIVE proposed that

the temperature for catalyst to be active (90% efficiency) must be lowered to 150°C or below based on the exhaust temperature of future engine, which is named "150°C challenge".[21]

1.4.2: Catalytic Properties of Lanthanum based Perovskite Oxides

Perovskite-type materials (ABO_3), especially lanthanum based oxides have been widely investigated in the past decade as catalysts for nitric oxides removal, hydrocarbons oxidation and soot oxidation due to their good catalytic activity. [26, 27, 28] The ideal perovskite crystal unit cell is cubic from Pm3m space group, where A-site cation is 12-fold coordinated oxygen and B-site cation is 6-fold coordinated with oxygen. For lanthanum based perovskites, the B-site is usually occupied by the transition metal elements that exhibit multiple valence state. Thus, the B-site cations can be reduced to low valance state in reducing atmosphere and oxidized to high valence state in oxidizing atmosphere. Perovskite oxides, as promising catalysts, have an important advantage that they are able to accommodate a variety of external elements without destroying the structure. The dopants substitute either A site or B site cations, affecting the valence state of cations and changing the redox and surface properties of perovskite oxides. [29, 30] As a common sense, the exhaust from engine includes higher amount of water vapor. It could lead to agglomeration of active phase of catalysts during long-term operation at high temperature, which is accompanied by reducing surface area under sintering effect. However, the current synthetic approaches usually yield perovskite catalysts with low surface area which even suffers severe decrease after hydrothermal ageing. For example, the surface area of $LaMnO_3$ catalyst drops from 21.8 to 5.0 m^2/g after hydrothermally aged at 800˚C for 12 h. [31] Thus, poor surface area, or in another word, poor dispersion of active sites is one of the major hurdle for pursuing high performance perovskite catalysts for automotive emission control. Moreover, though perovskite

based catalysts show great activity for nitric oxides removal and CO oxidation, their activity for low temperature hydrocarbons oxidation, especially propane oxidation, is still a great challenge. [32, 33] Lanthanum based perovskite catalysts usually exhibit high activation energy and high light-off temperature for propane oxidation even incorporated with noble metal. For example, Pd incorporated $La_{0.9}Sr_{0.1}CoO_3$ shows T_{50} of 340˚C although γ-Al_2O_3 has been used as support to improve its surface area.[34]

In summary, lanthanum based perovskite catalysts are lack of low temperature activity for HCs oxidation due to their poor surface area and high activation energy. The current synthetic approach cannot meet the requirement of design of high-efficiency perovskite catalysts. To address these issues, nano-array technology may guide us to a new direction to pursue highly efficient perovskite based monolithic catalysts for LTC exhaust aftertreament. As a family of ternary or more complex compounds, perovskite structures have been much less accomplished than binary or elemental matters so far in terms of synthetic fabrication of 1-D nanostructures.[35] Logically, it has been rather challenging to directly synthesize 1-D perovskite nanostructure array on 3-D honeycomb substrate. As an alternative route, we will use ZnO nanorod array as the secondary support to fabricate large-scale lanthanum perovskite based nano-array catalysts. ZnO nanorods array can be fabricated through low temperature (<100°C) hydrothermal method which features merits in cost-effectiveness and environmental benignity. We believe ZnO/perovskite nano-array based monolithic catalysts possess unique catalytic properties that hardly observed in conventional perovskite catalysts.

1.4.3 Role of Defect in Perovskite

One of the advantages of perovskite based catalysts is their tunable redox ability through introducing the defects in ideal perovskite crystal structure. A-site substitution with other elements and A or B site cation deficiency are two methods to introducing defects. Since the stoichiometry of perovskite is fixed at ABO_3, substituting A-site cations with others having valence different than that of A leads to charge compensation by changing the valence of B-site cations. [36] For example, substitution of Sr^{2+} in $LaMnO_3$ and $LaCoO_3$ must yield partial change of Mn^{3+} to Mn^{4+} and Co^{3+} to Co^{4+}. Thus, the structure distortion and unstable species with higher valance state enable the perovskite to be more easily reduced. Shown in **Figure 1-6 (a)** [37], the peak in 150-530°C is associated with the reduction of Mn^{4+} to Mn^{3+}. The reduction region and peak intensity is dependent on the Sr^{2+} substitution degree. With higher substitution ratio, the reduction peak shits to lower temperature and becomes more intensive. Moreover, the peak in 550-930°C, which is assigned to Mn^{3+} to Mn^{2+}, also shits to lower temperature with increasing Sr^{2+} substitution because Sr substitution lowers the crystallinity of perovskite structure. Meanwhile, part of charge imbalance caused by A-site substitution will be neutralized by formation of oxygen vacancies. As shown in **Figure 1-6 (b)** [38], the low temperature peak (<400°C) is associated with desorption of surface chemisorbed oxygen species (α-oxygen). The desorption intensity significantly increases with substitution of A-site cations, which indicates the surface oxygen defect population is increased. Based on the Mars Van Krevelen mechanism, the population of surface oxygen vacancies is an important parameter to determine the catalytic activity of metal oxides catalysts in oxidation reactions. Thus, A-site substitution can be used as reliable approach for tuning the catalytic activity of perovskite oxides for oxidation reactions.

Besides the A-site substitution, A-site or B-site cations deficiency also yields the increased redox ability of perovskite oxides. For example, the A-site cation deficiency must be compensated by either formation of Mn^{4+} or oxygen vacancies to maintain the charge balance. K. Huang, et.al reported a method to enhance the catalytic activity of $La_{0.5}Sr_{0.5}MnO_3$ catalyst through acid etching.[39] The diluted acid selectively removes partial A-site La cations. As the consequence, both the surface Mn^{4+} and oxygen vacancies populations are significantly increased compared to fresh catalyst.

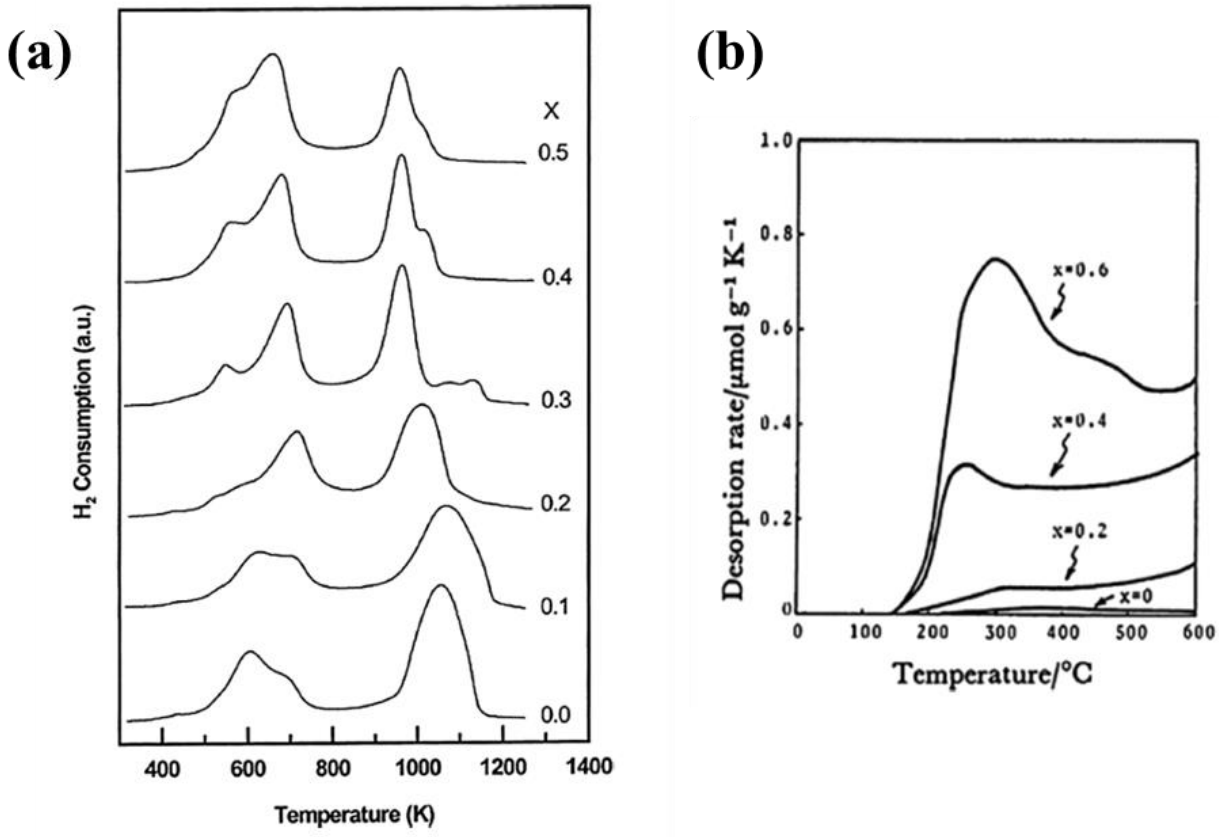

Figure 1-6. (a) Temperature-programmed reduction profiles of $La_{1-x}Sr_xMnO_3$, (b) temperature-programmed-desorption of oxygen of $La_{1-x}Sr_xCoO_3$.

1.5: Dissertation Objectives

The overall objective of this dissertation is to develop a new type of perovskite based nano-array catalysts with well-defined geometric configuration featuring improved catalytic activities, low materials usage, and enhanced hydrothermal stability. The essential purpose is to investigate the perovskite based monolithic catalysts as a potential candidate for low temperature combustion aftertreament. Specifically, this dissertation work will be focused on the following five tasks to:

1) Design and synthesize ZnO/perovskite core/shell nano-array based monolithic catalysts and test the catalytic activity for propane oxidation.

2) Study the catalytic activity and hydrothermal stability of Pt incorporated perovskite nano-array catalysts.

3) Enhance the low temperature activity of perovskite nano-array catalysts by structure modification and surface chemistry tuning.

4) Develop industrial relevant scalable manufacturing via hydrothermal based continuous flow synthesis.

Reference

1: A.A Abdel-Rahman, *International Journal of Energy Research*, ***1998***, *22*(6), pp.483-513.

2. All EPA Emission Standards, https://www.epa.gov/emission-standards-reference-guide

3. S. Pischinger, *Top Catal*. **2016**, 59, 834-844.

4. V. Tomašić, F. Jović, *Appl. Catal. A*, **2006**, *311*, pp.112-121.

5. T.A. Nijhuis, A.E. Beers, T. Vergunst, I. Hoek, F. Kapteijn, J.A. Moulijn, J.A., *Catal. Reviews*, 2001, 43, 345-380.

6. J. Jiang, Y. Li, J. Liu and X. Huang, *Nanoscale*, **2011**, 3, 45-58.

7. R. S. Devan, R. A. Patil, J. H. Lin and Y. R. Ma, *Adv. Funct. Mater*., **2012**, 22, 3326-3370.

8. P. Poudel and Q. Qiao, *Nanoscale*, **2012**, 4, 2826-2838.

9. K. Zhou, X. Wang, X. Sun, Q. Peng and Y. Li, *J. Catal*., **2005**, 229, 206-212.

10. X. Liu, M.-H. Liu, Y.-C. Luo, C.-Y. Mou, S. D. Lin, H. Cheng, J.-M. Chen, J.-F. Lee and T.-S. Lin, *J. Am. Chem. Soc*, **2012**, 134, 10251-10258.

11. H. Li, X. Wang, J. Xu, Q. Zhang, Y. Bando, D. Golberg, Y. Ma and T. Zhai, *Adv. Mater*., **2013**, 25, 3017-3037.

12. X. Sheng, D. He, J. Yang, K. Zhu and X. Feng, *Nano lett*., **2014**, 14, 1848-1852.

13. C. J. Lin, S.-J. Liao, L.-C. Kao and S. Y. H. Liou, J. *Hazard. Mater*., **2015**, 291, 9-17.

14. Z. Ren, Y. Guo and P.-X. Gao, *Catal. Today*, **2015**, 258, 441-453.

15. B. Weng, S. Liu, Z.-R. Tang and Y.-J. Xu, *Rsc Advances*, **2014**, 4, 12685-12700.

16. Liu, Z.-R. Tang, Y. Sun, J. C. Colmenares and Y.-J. Xu, *Chem. Soc. Rev*., **2015**, 44, 5053-5075.

17. Y. Guo, Z. Ren, W. Xiao, C. Liu, H. Sharma, H. Gao, A. Mhadeshwar, P.X. Gao, *Nano Energy*, **2013**, 2, 873-881.

18. Z. Ren, V. Botu, S. Wang, Y. Meng, W. Song, Y. Guo, R. Ramprasad, S. L. Suib and P. X. Gao, *Angew. Chem. Int. Ed*., **2014**, 53, 7223-7227.

19. Z. Ren, Z. Wu, W. Song, W. Xiao, Y. Guo, J. Ding, S. L. Suib and P.-X. Gao, *Appl. Catal. B*, **2016**, 180, 150-160.

20. S. Saxena, I.D. Bedoya, I.D., *Prog. Energy Combust.*, **2013**, 39,457-488.

21. M. Zammit, C. DiMaggio, C. Kim, C. Lambert, G. Muntean, C. Peden, J. Parks and K. Howden, "Future automotive aftertreatment solutions: the 150 C challenge workshop report," *US Drive Report*, Southfield, MI, **2013**.

22. Z. Ren, Y. Guo, P.X. Gao, Nano-array based monolithic catalysts: Concept, rational materials design and tunable catalytic performance. *Catal. Today*, **2015**, 258, 441-453.

23. G.K. Lilik, A.L. Boehman. *Energy & Fuels*, **2011**, 25, 1444–56.

24. S. Imtenan, M. Varman, H.H. Masjuki, M.A. Kalam, H. Sajjad, M.I. Arbab, I.R. Fattah, *Energy Convers. Manage*, **2014**, 80, 329-356.

25. K. Akihama, Y. Takatori, K. Inagaki, S. Sasaki, A.M. Dean, *SAE paper*, **2001**, 01–0655.

26. W.F. Libby, *Science*, **1971**, 171, 499.

27. R.J.H. Voorhoeve, J.P. Remeika, P.E. Freeland, B.T. Matthias, *Science*, **1972**, 177, 353.

28. P.K. Gallagher, D.W. Johnson, F. Jr, F. Schrey, *Mater. Res. Bull*. **1974**, 9, 1345.

29. S. Ponce, M.A. Peña, J. L. G Fierro, *Appl. Catal*., *B*, **2000**, 24, 193.

30. T. Nakamura, M. Misono, Y. Yoneda, Bull. *Chem. Soc. Jpn*. **1982**, 55, 394.

31. J. Chen, M. Shen, X. Wang, J. Wang, Y. Su, Z. Zhao, Catalysis Communications., 2013, 37, 105-108.

32. M. Alifanti, J. Kirchnerova, B. Delmon, D. Klvana, *Appl. Catal. A*, **2004**, 262, 167-176.

33. S. Royer, D. Duprez, F. Can, X. Courtois, C. Batiot-Dupeyrat, S. Laassiri, H. Alamdari, *Chem. Rev.,* **2014**, 114, 10292-10368.

34. C.H. Kim, G. Qi, K. Dahlberg, W. Li, *Science*, **2010**, 327, 1624-1627.

35. P.X. Gao, P. Shimpi, H. Gao, C. Liu, Y. Guo, W. Cai, Kuo-Ting Liao, Gregory Wrobel, Z. Zhang, Z. Ren, H.J. Lin, *Int. J. Mol. Sci.*, **2012**, 13, 7393-7423

36. R.J.H. Voorhoeve, J.P. Remeika, L.E. Trimble, *Ann. N. Y. Acad. Sci.*, **1976**, 272(1), 3-21.

37. S. Ponce, M.A. Pen˜a, J.L.G Fierro, *Appl. Catal.*, B, **2000**, 24, 193.

38. T. Nakamura, M. Misono, Y. Yoneda, *Bull. Chem. Soc. Jpn*. **1982**, 55, 394.

39. K. Huang, X. Chu, L. Yuan, W. Feng, X. Wu, X. Wang, S. Feng, *Chem. Commun*, **2014,** 50, 9200-9203.

CHAPTER 2

Experiment and Characterization

1-D nanostructures have only one dimension less than 100 nm. Currently, aqueous chemical reaction is the most convenient method to fabricate 1-D metal oxide nanostructures.[1] The driving force of hydrothermal growth of ZnO nanorods/nanowires is to minimize the free energy of entire reaction system.[2] The polar surfaces $\pm$(0001) terminated by Zn^{2+} or O^{2-} have high energy than other surfaces. Therefore, the adsorption rate of precursor molecules on these surface is much higher than on the other surface, making the nanostructures preferentially grow along c-axis. [3] For typical hydrothermal synthesis of ZnO nanorod array, a layer of ZnO seeds on substrate is essentially required before the reaction because the seeds enable the reaction to bypass the heterogeneous nucleation on substrate at the initial stage. The morphology of obtained ZnO nanorod array, especially the length to diameter ratio, is dominated by synthetic conditions including reaction temperature, initial precursor concentration and reaction time. [4] A uniform coverage of ZnO nanorod array on monolith is an essential prerequisite for highly dispersed perovskite coating on it. Perovskite deposition on 3-D ZnO nano-array is much more complicated than on bare monolith because subtle difference of solution concentration and viscosity may lead to completely different morphology of coating on individual nanostructure. To obtain ideal catalysts, compatible characterization over nano-array catalysts must be performed. The morphology and crystal structure of nano-array catalysts are characterized using electron microscopes. The chemical structures such as chemical formula surface cation and surface oxygen species are characterized by x-ray diffraction and various spectroscopes. The

catalytic activity of prepared nano-array catalysts is investigated using Fourier Transform Infrared Spectroscopy (FTIR) and Gas Chromatography (GC).

In this chapter, we will introduce the details of experiment setup, experimental procedure, characterization technique and instruments that have been used on nano-array catalysts.

2.1: Experimental Set-up

Hydrothermal synthesis of ZnO nanorod array and sol-gel deposition of perovskite via dip-coating process are two major steps of preparation of ZnO/perovskite nano-array based monolithic catalysts. In the following subsections, the substrate and precursors as well as the experiment procedure will be discussed.

2.1.1: Substrate and Precursors

(I) Ceramic honeycomb cordierite substrate ($2MgO{\cdot}2Al_2O_3{\cdot}5SiO_2$): the substrates are purchased from Corning Inc. They have multiple straight channels traversing the direction of length. The cell density is 600 cpsi. The hydraulic diameter of channels is 0.97. The substrates serve as carrier of catalysts and they will be used for hydrothermal growth of ZnO nano-array.

(II) Zinc acetate dihytrate [$Zn(CH_3COO)_2{\cdot}2H_2O$, 219.49 $g{\cdot}mol^{-1}$]: white solid chemical that used as Zn precursor in hydrothermal synthesis.

(III) Hexamethylenetetramine ($(CH_2)_6N_4$, HMT, 99%): white crystalline compound which is highly soluble in water. It's an important reactant for anisotropic growth of ZnO. It also acts as a weak base and pH buffer.

(IV) Lanthanum(III) nitrate hexahydrate ($La(NO_3)_3 \cdot 6H_2O$, 99%): white powder used as precursor of lanthanum cations in $LaMnO_3$ deposition.

(V) Manganese(II) nitrate tetrahydrate ($Mn(NO_3)_2 \cdot 4H_2O$, 99.98%): It is an inorganic compound with weak pink color. It is used as manganese precursor in $LaMnO_3$ deposition.

(VI) Tetraammineplatinum(II) nitrate ($[Pt(NH_3)_4](NO_3)_2$, 99.995%): it is white powder which is highly soluble in water. It is used as platinum precursor in co-deposition of perovskite and platinum nanoparticles on ZnO nano-array.

(VII) Strontium nitrate ($Sr(NO_3)_2$): it is an inorganic compound used as strontium precursor for $La_{0.8}Sr_{0.2}MnO_3$ film deposition.

(VIII) Dimethylformamide (DMF): it is an organic compound with formula $(CH_3)_2NC(O)H$. It is used as solvent for perovskite deposition. It is able to dissolve various metal oxide nitrate and surfactant for perovskite deposition.

(IX) Polyvinylpyrrolidone (PVP): it is a water-soluble polymer surfactant which can increase the viscosity of sol-gel solution.

2.1.2: Hydrothermal Synthesis

Hydrothermal synthesis is the first step to obtain ZnO/perovskite nano-array catalysts in this dissertation. The experiment is carried out in a glass reactor as presented in **Figure 2-1**. [4] 200 ml aqueous solution of zinc acetate and HMT (12.5 mM) is injected into glass reactor. The honeycomb substrate is horizontally immobilized at one side of the bottom in reactor. A magnetic stirring bar is located at the other side of bottom and shaking in high frequency. The

agitation creates an oscillating pressure between two ends of substrate and induces mass transport inside the channels. The glass reactor is incubated in an oil bath. The temperature is maintained at 90°C during the reaction. The solution should be refreshed every 6 h to facilitate the continually growth of ZnO nano-array. Since the reaction is accompanied by the formation of homogeneously nucleated nanostructures, the monolith must be rinsed with DI water before refreshing the growth solution. After the reaction, the monolith is dried in oven overnight before next step.

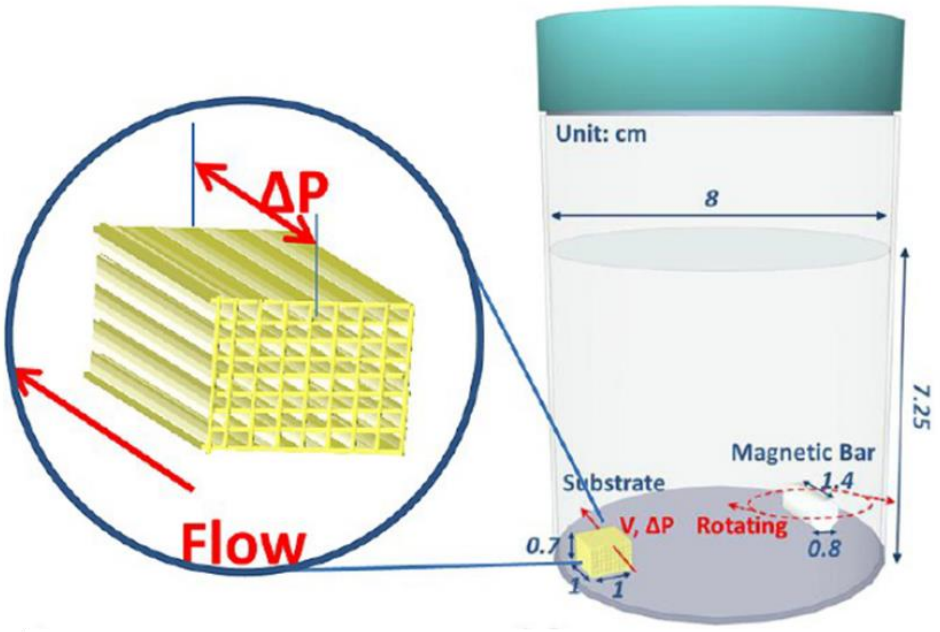

Figure 2-1. Mechanical agitation assisted hydrothermal synthesis of ZnO nano-array. [4]

2.1.3: Perovskite Deposition

Perovskite-type sol-gel solution aiming at $La_{0.8}Sr_{0.2}MnO_3$ is prepared by dissolving stoichiometric lanthanum(III) nitrate hexahydrate, strontium nitrate, manganese(II) nitrate

tetrahydrate (24 mM) in 20 ml N, N-Dimethylformamide (DMF) under sonication. 2 g polyvinylpyrrolidone (M.W 55,000) and 0.5 ml diethanolamine are dissolved in the other 20 ml DMF. These two solutions are mixed under vigorous stir at 60˚C and the solution turns dark brown. For co-deposition of perovskite and platinum nanoparticles, tetraamineplatinum nitrate should be added into sol-gel solution. The achieved solution must be aged for 24 hours before next process.

As presented in **Figure 2-2**, a piece of ZnO nano-array integrated monolith with dimension of 2cm × 2cm × 1cm is soaked in colloidal solution under sonication. Then the sample is transferred to a commercial kitchen use microwave oven for drying under the microwave irradiation. Microwave irradiation directly heats up the residual solution on the monolith and enhances the uniformity of coating across the channel length. After the sample becomes completely dry, it will be calcined at 350 ˚C for 5 minutes before next coating process. This step should be carried out to remove part of surfactant on the sample. The deposition procedure is repeated for a few cycles until the desired loading amount is acquired (15 wt%). The final thermal treatment is carried out at 700˚C for 2 h with ramping rate of 5˚C/min to increase the crystallinity of perovskite coating.

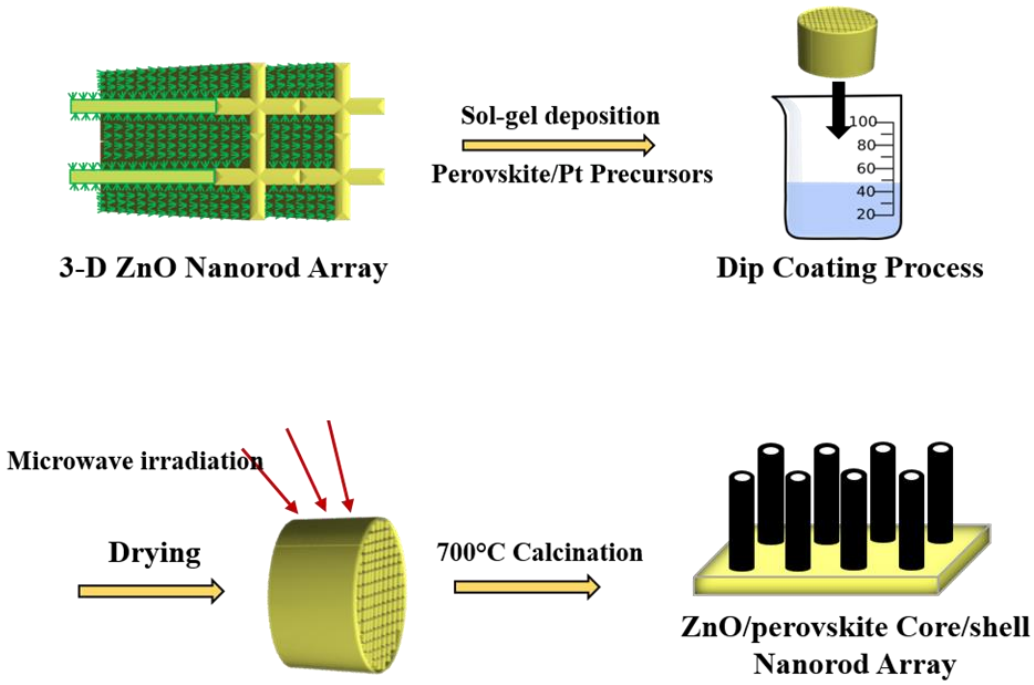

Figure 2-2. Schematic illustration of the dip-coating process of perovskite deposition on ZnO nano-array.

2.2: Structural Characterization

The physical and chemical structure of the nano-array catalysts will be investigated using the following characterization techniques.

2.2.1: Electron Microscopes

Electron microscopes used in this dissertation work include scanning electron microscope (SEM) and transmission electron microscope (TEM). SEM is an important materials characterization technique to study the topography and composition of sample surface. [5] It works

by irradiating the sample with a focused beam of electrons which interact with the atoms of samples. The sample is surrounded by various detectors to collect the produced signals including secondary electrons, back-scattered electrons, characteristics X-ray and etc. The secondary electrons are the electrons of samples excited by incident electron beam. Back-scattered electrons are those reflected by sample. Both of two types of electrons can provide image and reveal the detail of surface topography of sample. When the incident electrons beam hits the sample, the inner shell electrons of the sample atoms are removed and the positions are filled by electrons with higher energy. The extra energy is released as characteristic X-ray. Since each element atom has a unique electronic structure, the characteristic X-ray is used to identify the composition and quantify elements in the sample.

In TEM technique, the electrons of incident beam are either scattered by sample or transmitted through samples. Both of these two types of electrons will be collected and converted to images (dark field image from scattered electrons, bright field image from transmitted electrons). Therefore, the specimen used in TEM must be prepared with a thickness less than 100 nm. Compared to SEM, TEM is able to image at a significantly higher resolution. The crystal structure of sample such as grain size, grain boundary, distance of crystal plane can be studied in TEM. In this dissertation, TEM is also used to investigate the dispersion of perovskite coating and platinum nanoparticle distribution on ZnO nanorod.

During the dissertation study at the Institute of Materials Science in University of Connecticut, JEOL 6335F SEM, Tecnai T12 TEM, Talos F200X TEM have been employed for characterization of structure, morphology and composition of nanomaterials and nano-array catalysts.

2.2.2: X-ray Photoelectron Spectroscopy

X-ray photoelectron spectroscopy (XPS) is a surface characterization technique to investigate the surface chemistry of a sample at the parts per thousand range. (**Figure 2-3**) It works by irradiating the sample with an X-ray beam to excite the electrons of atoms within 10 nm depth of sample. The kinetic energy and number of electrons that escape from sample will be detected and analyzed by detector. The composition, chemical state and electronic state of elements and empirical formula of sample surface can be determined by XPS.

In XPS, the incident X-ray with particular wavelength has fixed energy (E_{photon}). The kinetic energy of escaped electrons ($E_{kinetic}$) can be measured by detector. Thus, the electron binding energy ($E_{binding}$) of excited electrons can be known through the equation:

$$E_{binding} = E_{photon} - E_{kinetic} - \Phi$$

Φ is the work function dependent on spectrometer and the materials. Because some kinetic energy of excited electrons will be adsorbed by detector. Thus, Φ is a constant which needs to be adjusted in practice. The spectrum of XPS is given by equation counts as a function of binding energy.

In this dissertation, XPS is used to investigate the surface species of perovskite and platinum, which include the valence state of surface manganese cations, surface lattice oxygen and chemisorbed oxygen as well as platinum nanoparticles.

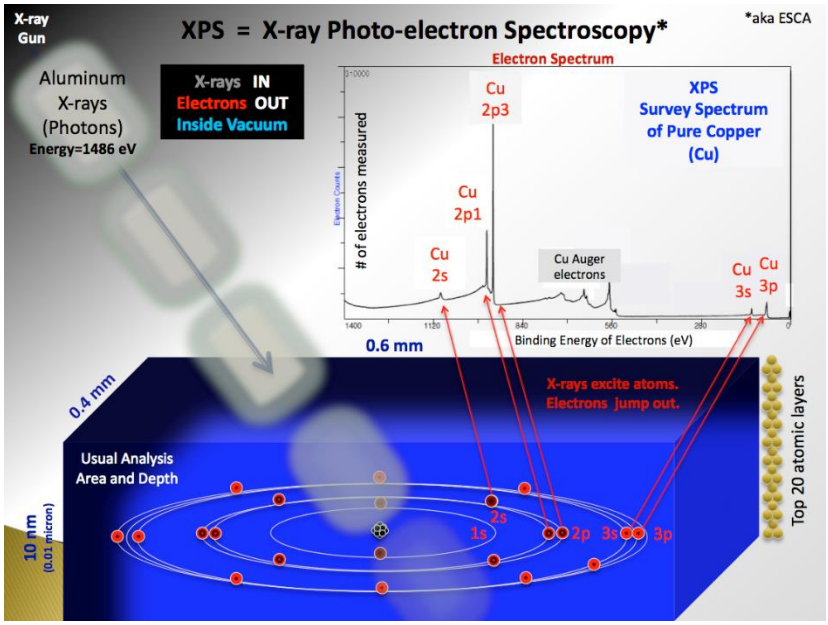

Figure 2-3. Illustration of principle of X-ray photoelectron spectroscopy (XPS). [6]

2.2.3: X-ray Diffraction

X-ray diffraction (XRD) is an analytical technique to identify the phase of crystalline materials. XRD is based on the interference of X-ray and crystalline sample. First, an incident ray is irradiated to the sample and the constructive interference will be produced if Bragg's law is satisfied:

$$n\lambda=2d\sin\theta$$

Where λ is the wavelength of incident beam, θ is the diffraction angle and d is the spacing between diffracting planes in a crystalline sample. By scanning the sample over a wide range of 2θ, the constructive interference occurs at particular 2θ due to the unique d-spacing of crystalline materials. The spectrum is presented by the signal intensity as a function of 2θ. By comparing the result with standard powder diffraction file, the chemical formula and phase of crystalline

materials can be identified. In this dissertation, the chemical formula and phase identification is performed by Bruker D2 Phaser.

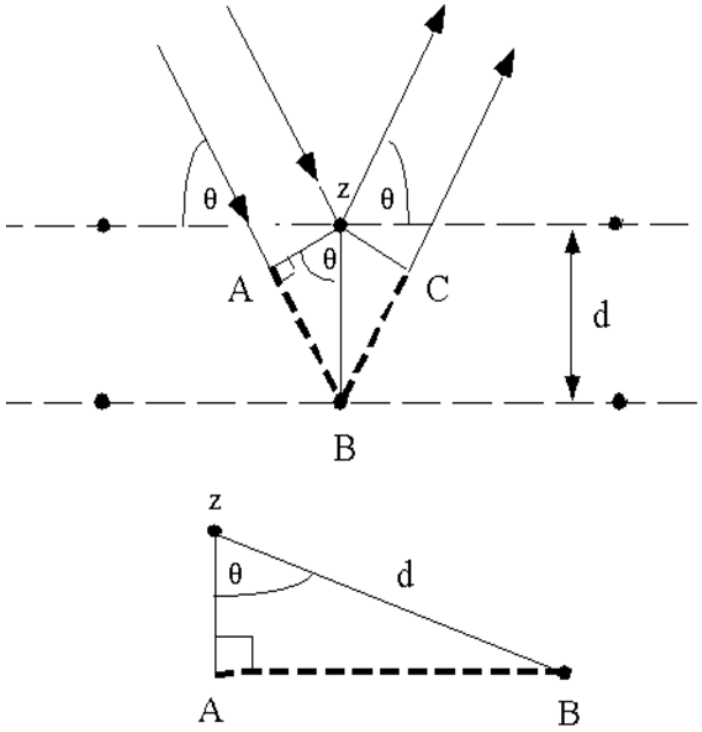

Figure 2-4. Illustration of Bragg's law in X-ray diffraction.

2.2.4: Temperature Programmed Reduction of H_2

Temperature programmed reduction of H_2 (H_2-TPR) is used to characterize a heterogeneous catalyst to find its reduction conditions. The sample is usually placed in a U-shape quartz tubing. The tubing is mounted in a furnace with temperature program controller. A thermal couple is placed near the sample in the tubing to record the reduction temperature. A gas flow composed of reducing component (H_2 with particular concentration) balanced with inert gas enters the tubing, and at the same time, the furnace is slowly ramping up (5°C/min or 10°C/min) from

room temperature to desired temperature. The variation of composition of the gas flow that exits the tubing is monitored by an instrument and the final spectrum is presented by H_2 consumption as a function of temperature. Since water vapor is the major reduction product, a cooling bath is usually used to eliminate the water vapor in the gas flow. The TPR-H_2 profile can be used for analyzing the reducing ability of catalyst, which is strongly associated with the catalytic activity of the catalyst.

2.2.5: Temperature Programmed Desorption of O_2

Temperature programmed desorption of O_2 (O_2-TPD) is used to investigated the activity and amount of oxygen species in catalysts. The sample is placed in a U-shape quartz tubing. The tubing is mounted in a furnace with temperature program controller. A thermal couple is placed near the sample in the tubing to record the desorption temperature. First, the sample is incubated in oxygen enriched gas flow at a particular temperature (200°C) to ensure the surface oxygen vacancies are filled by oxygen. Then the temperature is slowly decreased to room temperature in oxygen atmosphere. Then the gas flow is switched to inert gas to purge the tubing as well as sample to remove the physically adsorbed oxygen. Then the furnace is slowly ramping up (5°C/min or 10°C/min) from room temperature to desired temperature. The variation of composition of the gas flow exits the tubing is monitored by an instrument and the final spectrum is presented as O_2 desorption as a function of temperature. The desorption of surface oxygen and lattice oxygen can be clearly observed on TPD-O_2 profiles. In heterogeneous, the amount of surface oxygen species and the mobility of lattice oxygen are important parameters determining the activity of catalysts.

For both TPR-H_2 and TPD-O_2 characterization in this dissertation, the ChemiSorb 2720 Pulse Chemisorption System is used at the Nanomaterials Science Laboratory.

2.3: Catalytic Activity Characterization

The catalytic activity characterization in this dissertation is performed using two instruments: Fourier Transform Infrared Spectroscopy (FTIR) and Gas Chromatography (GC). FTIR is a technique that can be used to obtain an infrared spectrum of adsorption or emission of a solid, liquid or gas. The basic principle is that the instrument shines a beam containing many frequencies of light and measures the adsorption by the sample. Next, the beam is modified to contain a different combination of frequencies, giving a second data point. This process is repeated many times. Afterward, a computer collects all the data and identify the adsorption at each wavelength. Since each gas component has different light adsorption properties, the composition and concentration of the gas flow can be summarized from the spectrum given by FTIR. GC is another technique to analyze the gas composition. The system includes a few columns which is coated with stationary phase. The specimen is brought to the chambers by inert gas carrier. Since different gas components have different adsorption properties on stationary phase, they will be eluted one by one at different time. The analyzed result will be translated into electrical signal and the intensity is correlated with the concentration of this component.

Figure 2-5 shows the scheme of propane oxidation testing system. The monolithic catalyst is placed in a quartz tube that is mounted in a tubing furnace. The inlet gas is composed of C_3H_8, O_2 and N_2 with a fixed concentration ratio. The gas flow exiting from monolithic catalyst is analyzed by a GC system. The reaction temperature is controlled by a program and a thermal

couple is placed 1cm away from the entrance of monolithic catalyst to record the inlet gas temperature. The result is analyzed through the software provided by Agilent Technology.

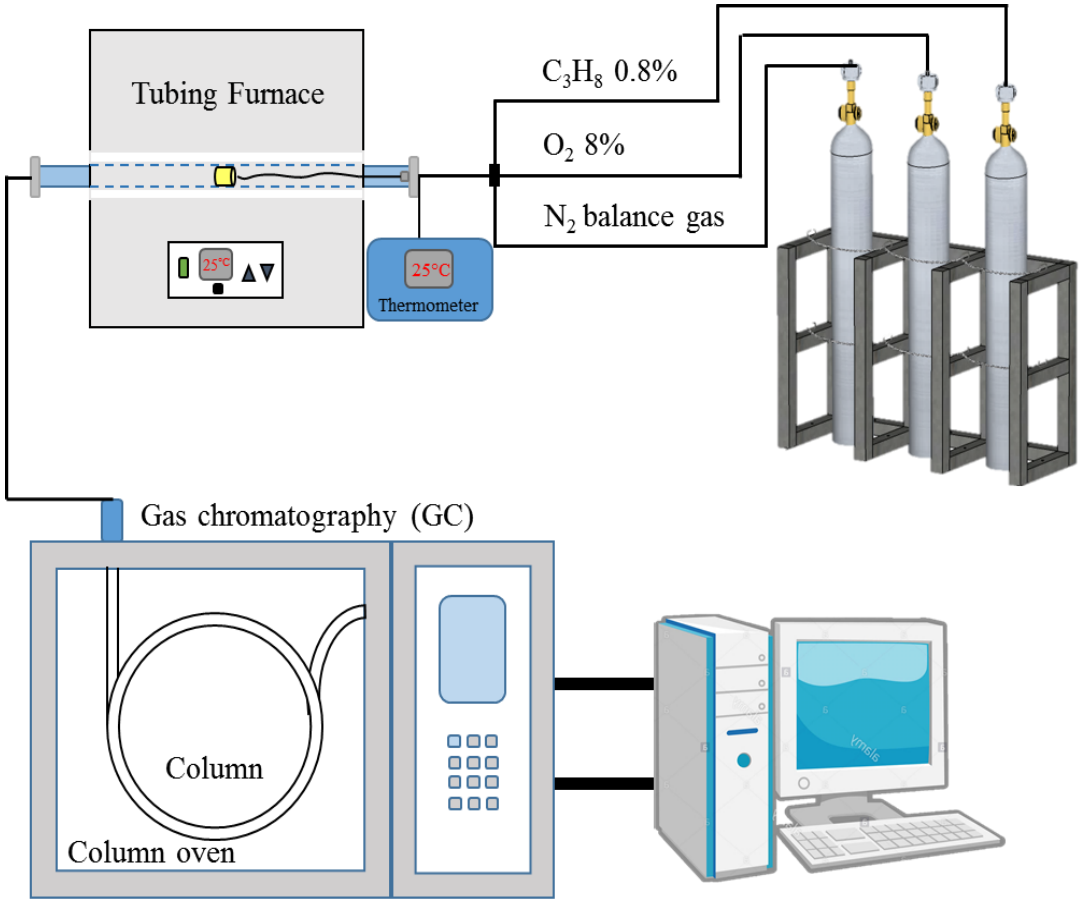

Figure 2-5. Scheme of GC based catalytic testing system for propane oxidation reaction.

Reference

1. L. Vayssieres, *Adv. Mater.*, **2003**,15, 464-466.

2. S. Xu, Y. Shen, Y. Ding, Z.L. Wang, *Adv. Funct. Mater.*, **2010**, 20, 1493–1495.

3. S. Xu, Z.L. Wang, *Nano Res.*, **2011**, 4, 1013-1098.

4. W. Xiao, Y, Guo, Z. Ren, G. Wrobel, Z. Ren, T. Lu, P. X. Gao. *Gryst. Growth Des*. **2013**, 13, 3657-3664.

5. D. Stokes, Principles and practice of variable pressure: environmental scanning electron microscopy (VP-ESEM). *John Wiley & Sons*, **2008**.

6. X-ray photoelectron spectroscopy, *Wikipedia,* https://en.wikipedia.org/wiki/X-ray_photoelectron_spectroscopy.

CHAPTER 3

ZnO/perovskite Core/shell Nanorod Array based Monolithic Catalysts for Low Temperature Propane Oxidation

A hydrothermal strategy combined with sol-gel deposition synthesis was successfully used to grow ZnO/perovskite ($LaBO_3$, B=Mn, Co, Ni) core-shell nanorod arrays within three-dimensional (3-D) honeycomb cordierite substrates. A facile sonication assisted colloidal wash coating process was able to deposit uniformly dispersed perovskite nanoparticles onto large-scale ZnO nanorod arrays on the channel surfaces of the substrate achieved by hydrothermal synthesis. Compared to traditional wash-coated perovskite catalysts, an enhanced catalytic performance was observed for propane oxidation with 25°C lower light-off temperature than wash-coated perovskite catalyst of similar $LaMnO_3$ loading (4.5mg). Temperature programmed reduction and desorption under H_2 and O_2 atmosphere, respectively, were used to study the reducibility and oxygen activity of these core-shell nanorod arrays based monolithic catalysts, revealing a catalytic activity sequence of $LaCoO_3$>$LaMnO_3$>La_2NiO_4 at the initial stage of catalytic reaction. The good dispersion and size control in La-based perovskite nanoparticles and their interfaces to ZnO nanorod arrays support may contribute to the enhancement of catalytic performance. This work may provide a new type of Pt-group metals (PGM) free catalysts with improved catalytic performance for hydrocarbon oxidations at low temperatures.

3.1: Introduction

The rapid consumption of platinum-group metals (PGM) and increasingly stringent exhaust emission restrictions impose a critical challenge for scientists and engineers to achieve

sustainable energy and environment globally.[1, 2] While pursuing energy efficiency and critical materials saving, as well as environmental pollution control, the environmental friendly and fuel-efficient low temperature combustion (LTC) technology represents a promising approach to be adopted as an upcoming solution. This, however, is in need of a compatible catalytic aftertreatment technology that can address the lack of low temperature catalytic activity in commercially available catalysts during cold start of automotive engines. Perovskite type materials, especially lanthanum based metal oxides have been widely investigated in the past decade as promising catalysts for hydrocarbon oxidation that possesses good stability at elevated temperature but suffer from compromised activity and high light-off temperature.[3, 4, 5, 6] Solutions have yet to be found for the inevitable trade-off between poor catalytic activity at low temperature and thermal stability at high temperature. [7] Moreover, traditional particle-form perovskite based monolith catalysts heavily rely on empirical wash-coating processes with general morphology lacking of well-defined structure. [8] Recently, nanostructure array based monolithic catalysts have been proposed, which may provide a promising solution to bridge the gap between catalytic performance and utilization efficiency of materials. [8, 9]

Herein, we report a cost-effective two-step (hydrothermal and sol-gel deposition) sequential synthesis approach to integrate commercial 3-D monolithic cordierite honeycomb with uniformly distributed ZnO/$LaBO_3$ (B = Co, Mn, Ni) core-shell nanorod arrays. Compared to traditional $LaMnO_3$ powder wash-coated monolithic catalysts, the ZnO/$LaMnO_3$ nano-array based structured catalyst shows significant enhancement of catalytic propane oxidation performance by lowering the activation energy and reducing the light-off temperature more than 25°C. A series of characterization techniques were used to investigate the reducibility and oxygen activity of different types of ZnO/perovskite core-shell nanorod arrays based monolithic catalysts.

3.2: Experimental

To prepare the $ZnO/LaBO_3$ (B = Co, Mn, Ni) core/shell nanorod arrays, all the experimental precursors, substrate and procedures were listed below.

3.2.1: Precursor and Substrate

(I) Zinc acetate dihytrate [$Zn(CH_3COO)_2 \cdot 2H_2O$, 219.49 $g \cdot mol^{-1}$] and Hexamethylenetetramine ($(CH_2)_6N_4$, HMT, 99%) were purchased from Fisher Scientific without further purification. Zinc acetate is crystalline white powder. HMT is a crystalline, heterocyclic organic compound. Both of the chemicals are highly soluble in water. They are used in hydrothermal synthesis of ZnO nanorod arrays on 3-D honeycomb cordierite.

(II) Lanthanum nitrate hexahydrate ($La(NO_3)_3 \cdot 6H_2O$), cobalt nitrate ($Co(NO_3)_2 \cdot 6H_2O$), manganese nitrate tetrahydrate ($Mn(NO_3)_2 \cdot 4H_2O$), nickel nitrate hexahydrate ($Ni(NO_3)_2 \cdot 6H_2O$) were purchased from Fisher Scientific without further purification. They are used as precursors in sol-gel solution for lanthanum based perovskite film deposition.

(III) Polyvinylpyrrolidone ($(C_6H_9NO)_n$, PVP, Mw58000) and diethanolamine ($(HOCH_2CH_2)_2NH$, 99%) were purchased from ACROS Organics. PVP is a water-soluble polymer which is used to adjust the viscosity of sol-gel solution. Diethanolamine is an organic compound which shows tendency to adsorb water. It is also used to adjust the PH value of sol-gel solution to avoid corrosion of ZnO nanorod array.

3.2.2: Hydrothermal Synthesis of ZnO Nanorod Array

Before ZnO nanostructure growth, a seed layer of ZnO should be deposited on 10×10 mm^2 bare cordierite substrates through a sonication-assisted dip coating method. [10] First, the cordierite substrate was cleaned with acetone and DI water thoroughly in sonication. Then 2.19g zinc acetate was dissolved in 500ml ethanol as the seeding solution. The dried substrate was submerged in solution under sonication and then dried in oven at 150°C for 10 mins. This seeding process was repeated for 10 cycles and the final calcination was performed at 350°C for 5 h.

The hydrothermal growth of ZnO nanorod array was carried out by using 200ml aqueous solution with equal moles of zinc acetate and HMT (12.5mM). The seeded substrate was submerged in growth solution and immobilized at the bottom margin of reactor. A magnetic stir bar was located at the opposite site of substrate and stirring at 500rpm to generate solution flow inside substrate channels. The reactor was incubated in oil batch to maintain the reaction temperature of 90°C. The aqueous solution was refreshed every 6 hours. After three cycles of growth, the substrate was rinsed with ethanol and dried naturally.

3.2.3: Perovskite Nanofilm Deposition

Firstly, three types of $LaBO_3$ (B = Mn, Co, Ni) colloidal solution were prepared by dissolving the stoichiometric metal nitrates (0.12 M) in 20 ml ethoxyethanol under sonication. Once the precursors were completely dissolved, 0.11g polyvinylpyrrolidone (PVP Mw 58000) and 0.15 ml diethanolamine were added under vigorous stirring, after which the solutions became cloudy and followed by 72 hours ageing in air. The perovskite film was deposited on ZnO nanorod arrays using a simple dip-coating method. The ZnO nanorod arrays integrated

substrate was submerged in sol-gel solution and sonicated for 1 minute. Then the substrate was transferred to a furnace and calcined at 300°C for 10 minutes. The dip-coating process was repeated for 8 times and followed by calcination at 650°C for 1 hour with a ramping rate 5°C/min to enhance crystallinity of metal oxides. The obtained ZnO/$LaMnO_3$, ZnO/$LaCoO_3$, ZnO/$LaNiO_3$ nano-array were denoted as ZnO/LMO, ZnO/LCO, ZnO/LNO, respectively. In 10 batches of the repeated wash-coating processes, the weight loading ratio of perovskites (e.g. LMO) is in a range of 5.8% - 6.0%, showing good reproducibility of the sonication assisted colloidal deposition in terms of perovskite loading amount.

3.3: Result and Discussion

Table 3-1 lists physical characteristics of ZnO nanorod arrays, LMO powder, and core-shell nanorod arrays based cordierite samples. After 8 times of wash-coating, the perovskite materials loading ratio can be controlled at around 12 g/L. The BET surface areas of these samples are also presented in the table. The BET surface areas of nano-array rooted on cordierite substrate surfaces were calculated based on Equation 3-1.

$$S_A = \frac{S_M * W_M - S_{BC} * W_{BC}}{W_A} \qquad \textbf{Equation 3-1}$$

The BET surface areas of perovskite film coated on ZnO nanorod array were calculated according to the following Equation 3-2.

$$S_P = \frac{S_M * W_M - S_{ZM} * W_{ZM}}{W_P} \qquad \textbf{Equation 3-2}$$

$S_A \; and \; W_A$: Surface area and weight of nano-array on cordierite

$S_P \; and \; W_P$: Surface area and weight of perovskite nanoparticles.

S_{BC} and W_{BC}: Surface area and weight of bare cordierite

S_M and W_M: Surface area and weight of monolithic samples

S_{ZM} and W_{ZM} : Surface area and weight of ZnO/cordierite monolithic sample

For LMO/cordierite sample, the BET surface area of LMO was calculated in a similar way based on the tested BET results of bare cordierites.

Table 3-1. Summary of physical properties of all samples.

Physical property	BET of monolithic sample m^2/g	Perovskite concentration based on ICP-AES result (mg/g)	Perovskite weight/volume loading ratio (g/L)	Calculated BET of nano-arrays (m^2/g)	Calculated BET of perovskite (m^2/g)	Catalysts for propane oxidation test (mg)	Perovskite material usage for test (mg)
Bare cordierite	0.36	--	--	--	--	--	--
ZnO/cordierite	1.43	--	--	16.72	--	93.0	None
LMO/cordierite	1.55	50.9	12.5	--	23.7	89.0	4.5
ZnO/LMO cordierite	1.73	42.1	10.2	13.95	8.6	98.2	4.1
ZnO/LCO cordierite	1.62	56.9	14.1	11.55	4.8	94.4	5.4
ZnO/LNO cordierite	2.10	43.8	10.7	17.38	16.7	96.3	4.2

X-ray diffraction analysis was conducted on the ZnO/perovskite nano-array monolithic catalysts. As a reference, the XRD pattern was collected on the perovskite powders synthesized from identical colloidal solution prepared for the nano-array based catalysts. $LaMnO_{3.5}$ (PDF 32-0484), $LaCoO_3$ (PDF 25-1060), La_2NiO_4 (PDF 89-3460), ZnO (PDF 36-1451) and cordierite

(PDF 12-0303) were detected. The patterns confirmed the formation of crystalline ZnO nanorod arrays and perovskite-type oxides.

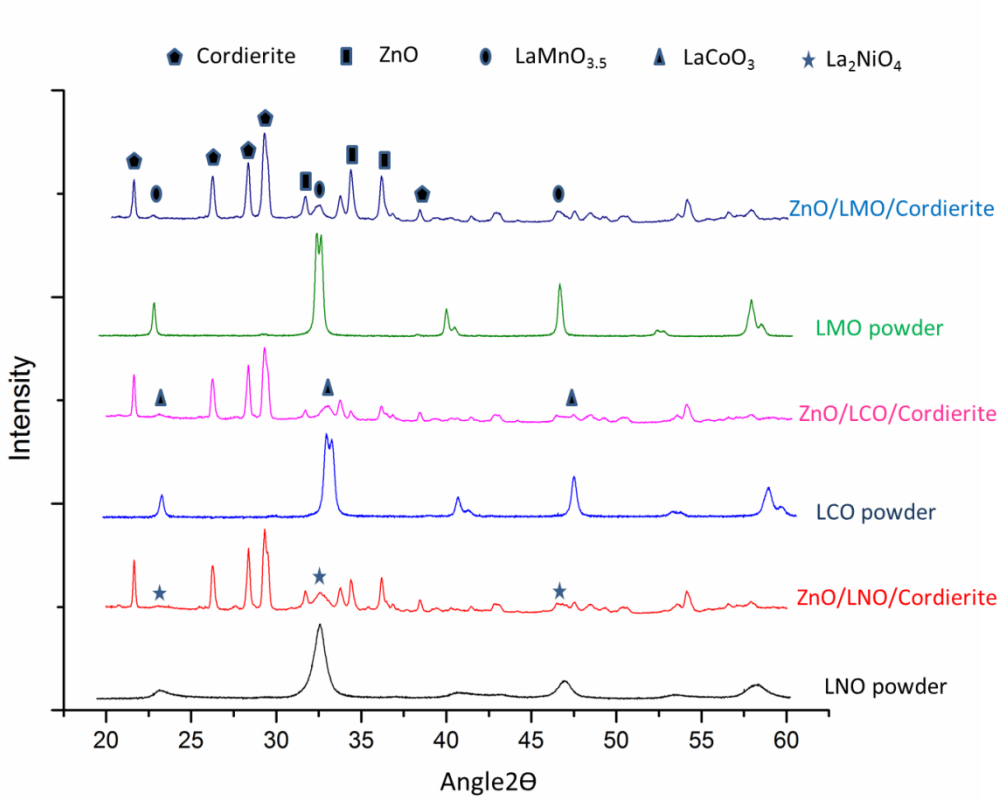

Figure 3-1. X-ray diffraction patterns of nanorod arrays based catalysts and perovskite powders.

Figures 3-2 (a) and **(b)** present typical morphology of ZnO nanorod arrays that uniformly rooted on the monolithic substrate channel surface. The weight loading ratio of ZnO nanorods is around 7% after 3 cycles of hydrothermal growth. The nanorod array displays a length of ~1.5 μm and a diameter of 150 nm- 200 nm. The geometry of ZnO nanorods could be tuned by the growth parameters such as temperature and precursor solution concentration. [10] **Figure 3-2 (d)**, **(e)** and **(f)** display the top view and **Figure 3-2 (g)**, **(h)** and **(k)** show the cross-sectional view of the three types of ZnO/perovskite core-shell nanorod arrays. Energy dispersive X-ray

spectroscopy (EDS) confirmed the successful loading of perovskite nano-shell. Taking ZnO/LMO **Figure 3-2 (c)** as an example, the atomic ratios of Zn, Mn, La elements are 83.6%, 8.0%, and 8.4%, respectively. The vertically aligned structural characteristic was well retained after perovskite film loading on ZnO nanorod arrays. The profiles of perovskite films on ZnO nano-arrays can be clearly observed in the respective cross-section SEM images **Figure 3-2 (g)-(k)**. Among the three types of core-shell nano-arrays, ZnO/$LaCoO_3$ nanorods possess a relatively rougher surface, indicating a larger size distribution of wash-coated $LaCoO_3$ nanoparticle film.

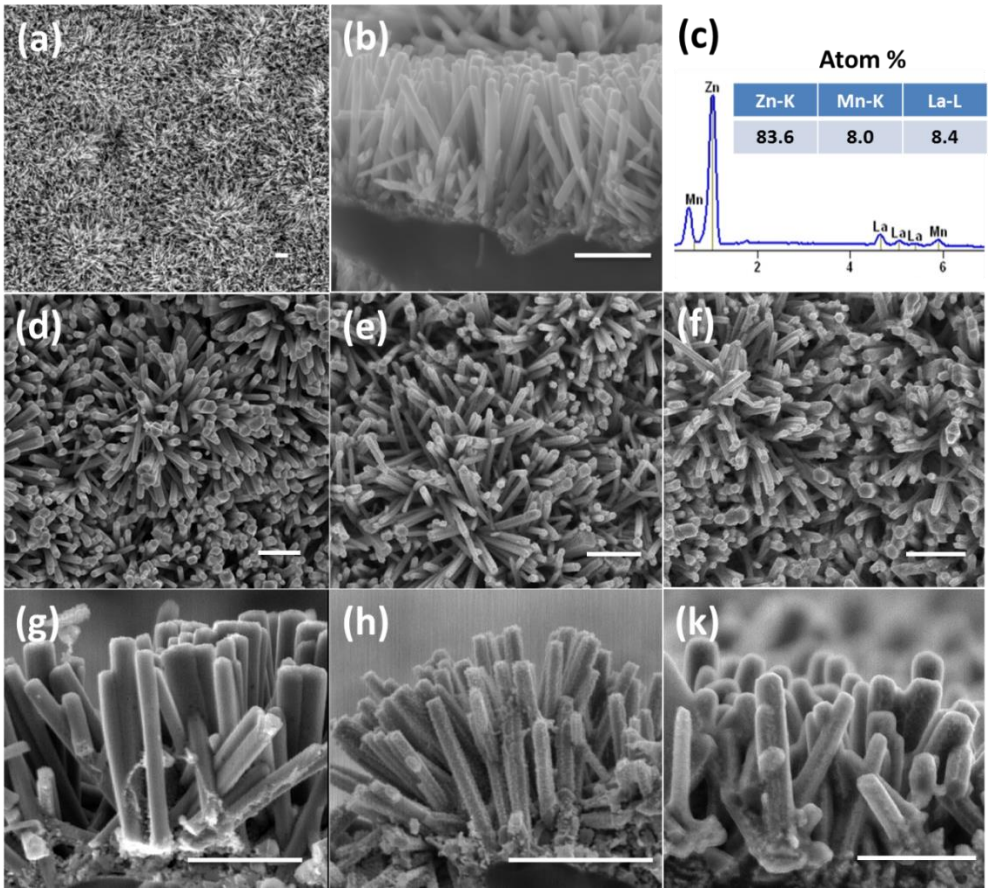

Figure 3-2. SEM images of (a) top view and (b) cross-section view of ZnO nanorod arrays rooted on monolithic cordierite substrate Top view and cross-sectional view of ZnO/LMO core-shell nanorod arrays (d)(g), ZnO/LCO core-shell nanorod arrays (e)(h); (f) ZnO/LNO

core-shell nanorod arrays (f)(k); (c) EDXS spectrum corresponding to the sample in (d). Scale bars without labels are 1 µm.

TEM characterization of ZnO/LCO and ZnO/LMO core-shell nanorods is presented in **Figure 3-3**. Perovskite $LaCoO_3$ particles can be clearly observed in bright **(a)** and dark **(b)** field images. The d-spacing values of {0 1 2} and {1 1 3} of $LaCoO_3$ lattice were labeled in Figure 3-3 (c). Figure 3-3 (d) shows the dark field image of a ZnO/LMO nanorod. The random distributed bright dots suggest LMO nanoparticles dispersed on ZnO nanorod. The thickness of perovskite coating can be increased by multiple colloidal wash coating cycles. And complete removal of residual solution before dried guarantees the uniformity of perovskite coating.

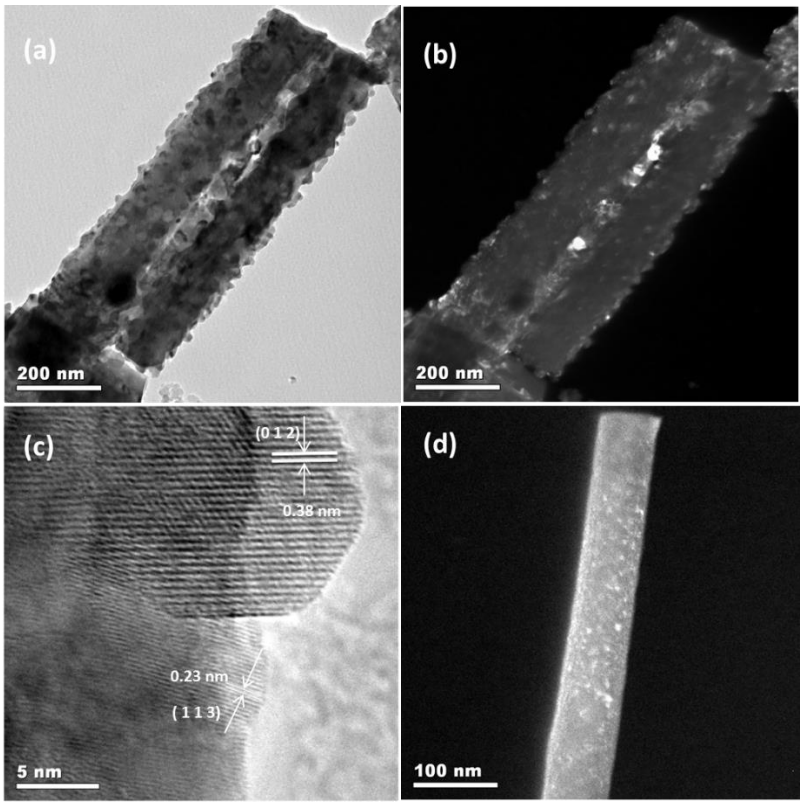

Figure 3-3. (a) Bright field and (b) dark field TEM images of ZnO/LCO core-shell nanorods; (c) HRTEM investigation of (a); (d) Dark field TEM images of a ZnO/LMO core-shell nanorod.

Figure 3-4 shows the propane oxidation light-off curves of core-shell nanorod arrays based cordierite samples and LMO coated cordierite sample as well as bare ZnO nanorod arrays based cordierite substrate. Compared to LMO coated monolithic sample, ZnO/LMO sample possesses a much lower light-off temperature (~30°C difference) and the activation energy is reduced from 283.9 kJ/mol (LMO) to 234.7 kJ/mol (ZnO/LMO), indicating an enchanced catalytic activity due to the ZnO/LMO core-shell nanorod structure. The improved performance may be attributed to good dispersion of LMO nanoparticles upon ZnO nano-array, facilitating the gas-solid interactions. [8] On the other hand, the interfaces between LMO nanoparticles and ZnO nanorods

support may also play an important role in catalytic performance improvement though direct evidence of interaction still needs further investigation. [11] In terms of lateral comparison of three types of ZnO/perovskte nano-array catalysts, ZnO/LCO sample shows the best catalytic performance at low temperature, with reaction initiated at 350°C of a significant propane conversion of over 13% where no conversion is detected for the other samples. However, ZnO/LCO and ZnO/LMO samples reach 50% conversion almost at same temperature (500°C) after which ZnO/LMO sample displays highest propane conversion until 650°C. Since the core-shell nanorod array based catalysts possess well-defined geometric characteristic as compared to LMO/cordierite catalyst, the reaction rate of propane oxidation was calculated in unit of mole per second per gram per square meter ($mol/s \cdot m^2$) of perovskite materials and presented in **Figure 3-4 (c)** as a function of temperature. The corresponding activation energies of three types of core-shell nanorod arrays based samples and LMO coated cordierite sample are presented in **Figure 3-4 (d)**. The reaction rate (catalytic activity) is revealed in the order ZnO/LCO > ZnO/LMO> ZnO/LNO.

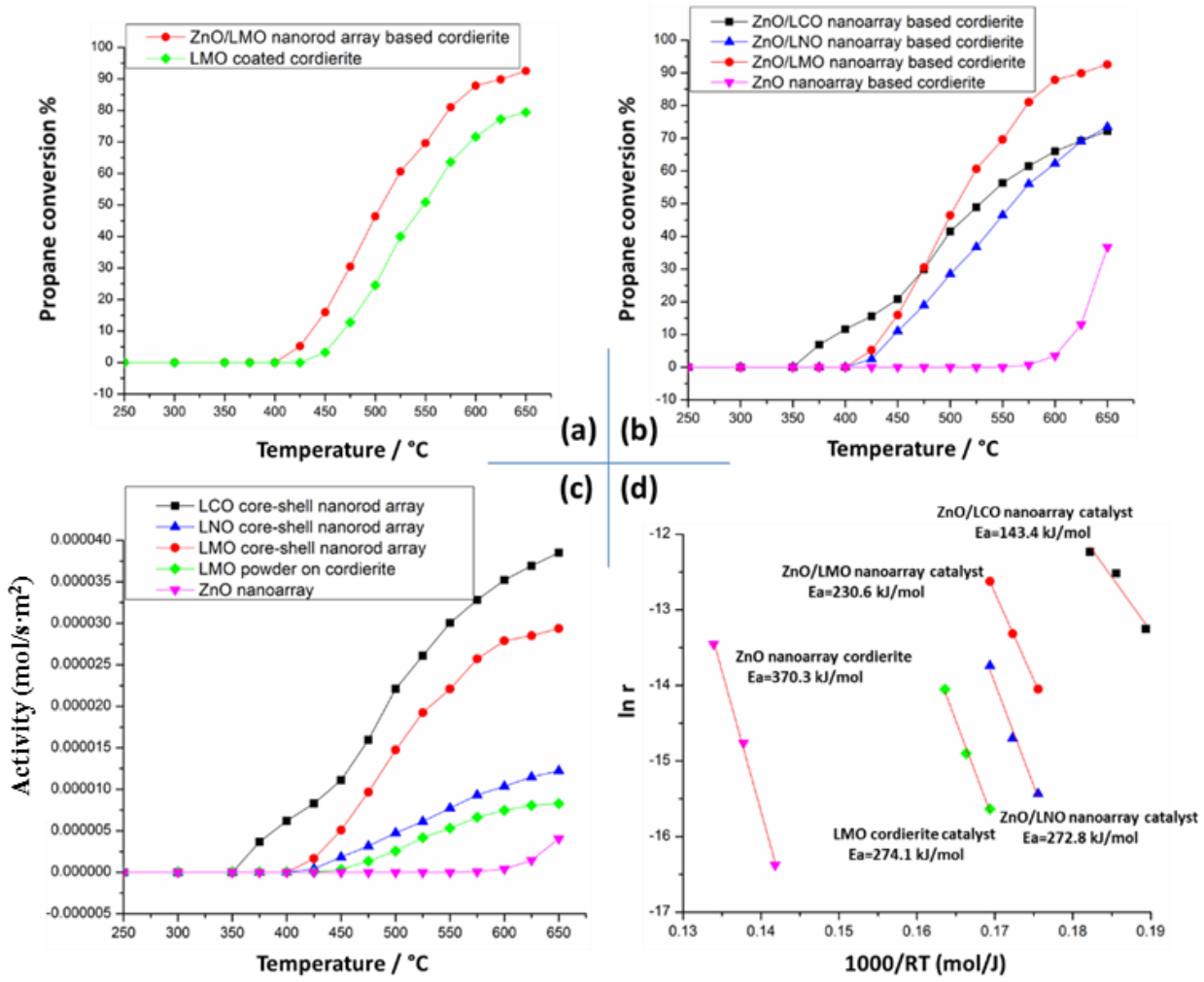

Figure 3-4. (a) and (b) catalytic performance of LMO powder based and core-shell nanorod arrays based catalysts for propane oxidation; (c) Activity of catalysts shown as a function of temperature; (d) Corresponding Arrhenius plots for the reaction kinetics.

Figure 3-5 (a) shows the temperature programmed reduction (TPR) profiles of three monolithic samples under H_2 atmosphere. In general, complete reduction of Mn^{4+} is hardly achieved and Mn^{3+} acts as an intermediate status before reduced to Mn^{2+}. [12, 13] For ZnO/LMO cordierite sample, a single major peak was observed between 350-400°C, which corresponds to the reduction of Mn^{4+} to Mn^{3+}. The shoulder located at ~500°C can be ascribed to the excess

oxygen and the reduction of ZnO nano-arrays. An initial consumption of H_2 was observed close to 800°C, which is attributed to the reduction of Mn^{3+} to Mn^{2+}. For the profile of ZnO/LCO cordierite sample, two major peaks appeared, which coincide with previous reports [14, 15] that Co^{3+} was first reduced to Co^{2+} (325-450°C), followed by reduction of Co^{2+} to Co^0 at higher temperature (>600°C). Moreover, the complete reduction of $LaNiO_3$ is divided into three stages, where La_2NiO_4 is formed as an intermediate phase. [16] Only two peaks were observed in the TPR profile of ZnO/LNO sample. The first peak is attributed to the reduction of nickel oxide (300-400°C), with the second peak due to the reduction of Ni^{2+} to Ni^0 (>550°C). [17] In addition, it is worth noting that H_2 intensity keeps dropping between the first and the second peaks in both ZnO/LCO and ZnO/LNO cordierite samples. This may result from the reduction of ZnO continuously consumed H_2 from 450 °C to 550°C. [18] Since the first peak for each sample displays very close reduction temperature, it is only concluded that the amount of surface lattice oxygen in ZnO/LCO is higher due to its higher H_2 consumption.

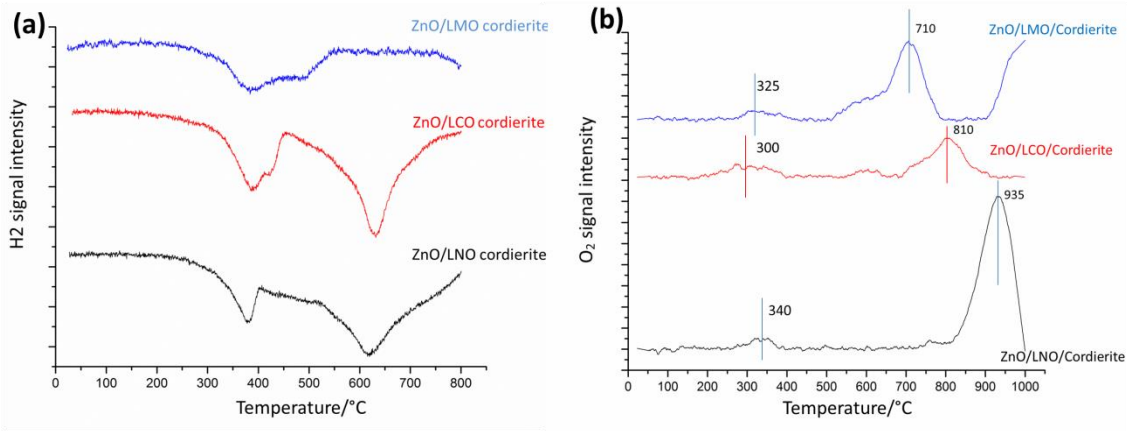

Figure 3-5. (a) H_2 Temperature-programmed-reduction and (b) Temperature-programmed-desorption of O_2.

It has been widely reported that there are two types of oxygen species in perovskite materials, α and β oxygen. α oxygen is suggested to desorb at a low temperature range of 300-600°C, as determined by the amount of surface oxygen vacancy. The peaks appeared at higher temperature (>600°C) correspond to the desorption of β oxygen, which is strongly associated with oxygen mobility in bulk. [15, 19] To understand the oxygen evolution in the ZnO/perovskite core-shell nanorod arrays, temperature programmed desorption test was carried out. The O_2-TPD profiles are presented in **Figure 3-5 (b)**. For α oxygen species, as compared to the other samples, ZnO/LCO cordierite possesses a broader peak located at relatively low temperatures (300°C) while relatively weak peaks were located at 325°C for ZnO/LMO and 340°C for ZnO/LNO respectively, indicating the oxygen species absorbed on surface vacancies are more active and the amount is higher than the other two samples. In a higher temperature range, a strong peak appears at 810°C with a strong shoulder at 600°C. For ZnO/LMO cordierite, the temperature of β oxygen peak is much lower (710°C) than the other two samples, accompanied by a noticeable shoulder from 520°C to 650°C that can be related to excessive lattice oxygen in $LaMnO_{3.5}$. [20] No obvious shoulder was detected in ZnO/LNO cordierite, a strong peak was observed at 935°C. Therefore, the activity of surface lattice oxygen was in the order of ZnO/LCO > ZnO/LMO > ZnO/LNO, which corresponds to the catalytic activity observed in propane oxidation light-off curves in the low temperature range (<400°C)

It is well known that perovskite metal oxide provides oxygen in the a catalytic reaction while B cation is reduced, then the reduced metal is reoxidized by aquiring oxygen from surroundings. [21] Hence, the activity of surface lattice oxygen and the mobility of oxygen in bulk play important roles in a complete redox cycle. [22] The order of three catalysts' performances at low temperature matches the order of activities of surface lattice oxygen observed in TPD-O_2

characterization, as supported by Mars-Van Krevelen mechanism. [23] As proposed, the surface lattice oxygen reacts with reactant molecule, leaving an oxygen vacancy on the surface of catalysts. The vacancy is filled by oxygen in gas phase or oxygen in bulk. For our samples, specifically, the mobility of oxygen in bulk was in the sequence of ZnO/LMO > ZnO/LCO > ZnO > LNO, which contradicts previous reports [14] that the oxygen mobility of LCO is more active than that of LMO in bulk. This can be demonstrated by the excessive lattice oxygen in $LaMnO_{3.5}$, which significantly enhanced catalytic activity of $LaMnO_{3.5}$ at high temperature. [24] Furthermore, the excessive lattice oxygen may contribute to the replenishment of surface oxygen vacancies and enable better catalytic performance of ZnO/LMO than that of ZnO/LCO above 500°C. As a potential contribution, the influence of ZnO/LMO interface should be further investigated. According to our previous report, [25] the thickness dependent ferromagnetic-superparamagnetic transition in (La, Sr)MnO_3 nanofilm on ZnO nanorod arrays was observed, which imposed another possible pathway to study catalytic activity improvement of ZnO/perovskite core-shell nanorod arrays based catalysts.

3.4: Conclusion

In summary, ZnO/$LaBO_3$ (B = Co, Mn, Ni) core-shell nanorod arrays have been successfully grown on 3-D honeycomb cordierite substrate using a hydrothermal and colloidal deposition synthesis method. Compared to traditional wash-coated LMO monolith catalyst, an enhanced catalytic performance was observed for ZnO/LMO nanorod arrays based catalyst with 25°C lower light-off temperature than wash-coated perovskite catalyst of similar LMO loading (4.5mg). And the corresponding activation energy also shows a decrease from 283.9 kJ/mol for LMO/cordierite catalyst to 230.6 kJ/mol for ZnO/LMO nanorod arrays based catalyst. The good

dispersion and size control in La-based perovskite nanoparticles and their interfaces to ZnO nanorod arrays support may be contribute to the enhancement of catalytic performance. The lateral comparison of three types of ZnO/$LaBO_3$ nanorod arrays based catalysts reveals a catalytic activity sequence of $LaCoO_3$ > $LaMnO_3$ > La_2NiO_4 at the initial stage of catalytic reaction. This work may provide a new type of Pt-group metals (PGM) free catalysts with improved catalytic performance for hydrocarbon oxidation at low temperature.

Reference

1. J. Lin, B. Qian, J. Liu, Y. Huang, A. Wang, L. Li, W. Zhang, L. F. Allard, X. Wang, T. Zhang, *Angew. Chem.* **2012**, 124, 2974-2978.

2. X. Mou, B. Zhang, Y. Li, L. Yao, X. Wei, D. S. Su, W. Shen, *Angew. Chem. Int. Ed*. **2012**, 51, 2989-2993.

3. M O'Connell, A.K Norman, C.F Hüttermann1, M.A Morris, *Catal. Today*. **1999**, 47, 123.

4. Nora A. Merino, BiBiana P. Barbero, *J. Catal.* **2005**, 231, 232-244.

5. T. Asada, T. Kayama, H. Kusaba, *Catal. Today.* **2008**, 139, 37-42.

6. Y. Lu, A. Eyssler, E. H. Otal, S. K. Matam, *Catal. Today.* **2013**, 208, 42- 47.

7. M. Alifanti, J. Kirchnerova, B. Delmon, D. Klvana, *Appl. Catal. A*, **2004**, 262, 167-176.

8. Y. Guo, Z. Ren, W. Xiao, C. Liu. H. Sharma, H. Gao, A. Mhadeshwar, P.-X. Gao. *Nano Energy*. **2013**, 2, 873-881.

9. Z. Ren, V. Botu, S. Wang, Y. Meng, W. Song, Y. Guo, R. Ramprasad, S. Suib, P.-X. Gao. *Angew. Chem. Int. Ed*. **2014**, 53, 1-6.

10. W. Xiao, Y, Guo, Z. Ren, G. Wrobel, Z. Ren, T. Lu, P. X. Gao. *Gryst. Growth Des*. **2013**, 13, 3657-3664.

11. D. Jian, P.-X. Gao, W. Cai, B.S. Allimi, S. Pamir Alpay, Y. Ding, Z. L. Wang, C. Brooks, J. Mater. Chem. 2009, 19, 970–975.

12. S. Irusta, M.P. Pina, M. Menéndez, J. Santamaria, *J. Catal*. **1998**, 179, 400-412.

13. A. Kaddouri, S. Ifra, *Catal. Commun*. **2006**, 7, 109-113.

14. S. Royer, F. Bérubé, S. Kaliaguine, *Appl. Catal*. *A.* **2005**, 282, 273-284.

15. B. Levasseur, S. Kaliaguine, *Appl. Catal. A.* **2008**, 343, 29-38.

16. C. Batiot-Dupeyrat, G. Valderrama, A. Meneses, F. Martinez, J. Barrault, *Appl. Catal. A.* **2003**,248, 143-151.

17. G. S. Gallego, F. Mondragón, J. M. Tatibouët, *Catal. Today*. **2008**, 133, 200-209.

18. M. Liang, W. Kang, K. Xie, J. *Natural Gas Chem*. **2009**, 18, 100-113.

19. K. Kaliaguine, A. Van Neste, V. Szabo, J. E. Gallot. M. Bassir, R. Muzychuk, *Appl. Catal. A.* 2001,209, 345-358.

20. C. Zhang, Y. Guo, Y. Guo, G. Lu, A. Boreave, L. Retailleau, A. Baylet, A. Giroir-Fendler. *Appl. Catal B.* 2014, 148, 490-498.

21. M. Baldi, E. Finocchio, F. Milella, G. Busca, *Appl. Catal B.* **1998**, 16, 43-51.

22. R. K. Grasselli, *Topics in Catal*. **2002**, 21, 79-88.

23. B. C. Enger, R. Lødeng, Anders Holmen, *Appl. Catal A.* **2008**, 346, 1-27.

24. L. Marchetti, L. Forni, *Appl. Catal B. Environmental*. 1998, 15, 179-187.

25. H. Gao, M. Staruch, M Jain, P. Gao, P, Shimpi, Y. Guo, W. Cai, H. Lin, *Appl. Phys. Lett.* **2011**, 98, 123105.

CHAPTER 4

Pt Loaded ZnO/perovskite Nano-array Catalysts: Enhanced Low Temperature Activity and Hydrothermal Stability

Uniformly dispersed platinum nanoparticles are successfully loaded on ZnO/$LaSr_{0.2}Mn_{0.8}O_3$ nanorod array catalysts through sol-gel co-deposition method and atomic-layer-deposition (ALD) method. The incorporation of platinum significantly improves the catalytic activity of ZnO/$LaSr_{0.2}Mn_{0.8}O_3$ nano-array catalysts and shifts the light-off curves towards low temperature range. The light-off temperature of nano-array catalysts is strongly associated with the loading amount of platinum. 0.1Pt LSMO possesses comparable light-off temperature as ALD-Pt LSMO (250°C) but decreased 90% conversion temperature (T_{90}) by 120°C. After being aged in water vapor enriched gas stream at high temperature (700°C and 800°C), 0.1Pt LSMO exhibits much better activity than ALD-Pt LSMO though both catalysts show deactivation. The better hydrothermal stability of 0.1Pt LSMO can be attributed the better dispersion of platinum nanoparticles after long-term aging. And the interface between platinum and $LaMnO_3$ formed during co-deposition may play an important role in stabilizing the platinum nanoparticles.

4.1: Introduction

Monolithic catalysts have been widely used to reduce the exhaust emission from fuel based combustion systems such as gasoline engine, diesel engine. [1, 2] Traditional monolithic catalysts, which are composed of honeycomb cordierite substrate and powder-form catalysts, are lack of well-defined micro structure configurations, leading to compromised catalytic performance and

high materials usage. Perovskite oxides have been widely investigated as promising catalysts for automotive emission control since last century due to their good catalytic activity and stability. [3, 4, 5, 6, 7, 8] However, the current synthetic approaches usually yield powder-form perovskite catalysts with low surface area and poor hydrothermal stability. [9] Moreover, the catalytic activity of perovskite based catalysts for low temperature hydrocarbons removal is still a challenge, evidenced by their relatively high light-off temperature even though with noble metal incorporated. [10] To meet the requirement of increasingly stringent emission standard and push the perovskite based catalysts towards practical applications, more efficient perovskite catalysts with good low temperature activity and hydrothermal stability must be developed. Recently, 3-D metal oxides nano-array integrated honeycomb substrates such as cordierites have been investigated as promising monolithic catalysts due to enhanced catalytic activity and reduced materials usage. [11] Herein, we introduce design and fabrication of large-scale Pt loaded perovskite nano-array based monolithic catalysts with high catalytic performance for propane oxidation. Using ZnO nano-array as support, the perovskite oxide possesses high dispersion and subsequently leads to uniform distribution of platinum nanoparticles. The obtained catalysts also exhibit decent activity after being aged in water-vapor enriched gas steam at 800°C for 50 h (700°C for 100 h). With demonstrated integration strategy of hydrothermal synthesis and sol-gel deposition, the ZnO/perovskite-Pt nano-array catalysts provide a new type of efficient monolithic catalysts for automotive emission control.

4.2: Experimental

First, ZnO nanorod array integrated monolith should be prepared through hydrothermal based continuous flow synthesis. The detailed procedure will be described in Chapter 6. The

ZnO nano-array obtained from this method is free of precipitates and more favorable to uniform deposition of perovskite coating. Herein, we use two different methods to load platinum nanoparticles on ZnO/ $LaSr_{0.2}Mn_{0.8}O_3$ nano-array and the procedures are described as below.

4.2.1: Co-deposition of Perovskite and Platinum Nanoparticles

First, perovskite type (xPt-$La_{0.8}Sr_{0.2}MnO_3$) sol-gel solution with platinum precursor was prepared by dissolving stoichiometric lanthanum(III) nitrate hexahydrate (19.2 mM), strontium nitrate (4.8 mM), manganese(II) nitrate tetrahydrate (24 mM) and tetraamineplatinum(II) nitrate (x% × 24 mM) in 20 ml N,N-Dimethylformamide (DMF) in sonication. In the other bottle, 2 g polyvinylpyrrolidone (M.W 55,000) and 0.5 ml diethanolamine were dissolved in 20 ml DMF. Then the two types of solution were fully mixed under vigorous stir at 60˚C and the solution turns dark brown. The achieved solution should be aged for 24 hours. ZnO nano-array integrated cordierite was used for perovskite nanofilm deposition to achieve the ZnO/Perovskite-Pt core-shell nanostructure. A piece of ZnO nano-array integrated monolith with dimension of 20 × 20 channels was submerged in sol-gel solution under sonication. Then the sample was transferred to a commercial kitchen use microwave oven for drying. This deposition process was repeated for a few cycles until the desired loading amount was acquired. The sample was calcined at 350˚C in air to remove partial surfactant between each deposition cycles. The final calcination should be carried out at 700˚C for 2 h with ramping rate of 5˚C/min.

4.2.2: Atomic-Layer-Deposition of Platinum on ZnO/perovskite Nano-array

Before ALD of platinum, ZnO/$La_{0.8}Sr_{0.2}MnO_3$ nano-array should be prepared by coating uniform $La_{0.8}Sr_{0.2}MnO_3$ nanoparticles on ZnO nano-array through the sol-gel deposition as described in 3.2.1. The obtained monolithic catalyst is used for ALD of platinum. The deposition is performed at 270 °C in vacuum condition using trimethyl (methylcyclopentadienyl) platinum(IV) and O_2 as platinum source and oxidant. Each deposition cycle is accompanied by 1s pulse of Pt precursor, followed by 30s N_2 purging and pumping to base pressure. The Pt loading amount is controlled by deposition cycles. After 40 cycles, the sample is taken out and used for catalytic reaction.

4.3: Result and Discussion

A series of monolithic Pt incorporated ZnO/$La_{0.8}Sr_{0.2}MnO_3$ nano-array catalysts were prepared with different Pt loading amount. The obtained catalyst is denoted as xPt LSMO, where x represents the molar percentage to Mn. The morphology of Pt incorporated $La_{0.8}Sr_{0.2}MnO_3$ nano-array (0.1Pt LSMO) on the wall surface of 3-D monolithic substrate is shown in **Figure 4-1 (a)**. The rough $La_{0.8}Sr_{0.2}MnO_3$ nano-shell can be clearly observed on the surface of ZnO nanorod array. A single core-shell nanorod is shown in **Figure 4-1 (b)**. The uniformly dispersed $La_{0.8}Sr_{0.2}MnO_3$ nanoparticles are able to significantly increase the surface area of nano-array, which is favorable to catalytic reaction. **Figures 4-1 (c)** and **(d)** display the Pt nanoparticles with average diameter of lower than 2 nm dispersed on perovskite nanofilm. The elements mapping demonstrates that no significant element agglomeration exists on this individual nanorod.

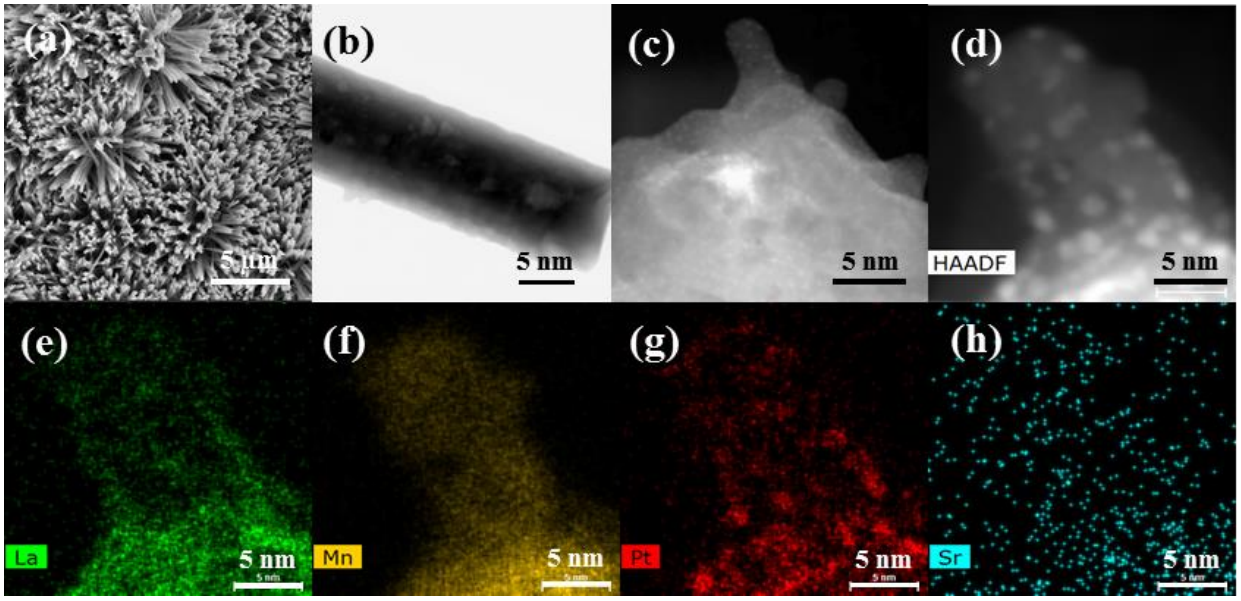

Figure 4-1. (a) Top-view SEM image of 0.1Pt LSMO catalyst. (b) Bright field TEM image of core/shell nanorod composed of ZnO nanorod and $La_{0.8}Sr_{0.2}MnO_3$-Pt nanofilm. (c) HAADF image showing tip of core/shell nanorod with highly dispersed platinum nanoparticles. (d) Higher magnification of TEM image showing the platinum nanoparticles. (e)-(h) Element mapping of La, Mn, Pt, and Sr.

Figure 4-2 shows the Pt loaded ZnO/perovskite core/shell nanorod obtained through ALD method. The white bright dots in **Figures 4-2 (a)** and **(c)** identify the successful deposited Pt nanoparticles. The element mapping of Pt implies relatively more uniformly dispersion of Pt nanoparticles on perovskite nanofilm than that obtained from Pt-perovskite co-deposition (**Figure 4-1 (g)**). The average diameter of Pt in **Figure 4-2 (c)** is ~5 nm.

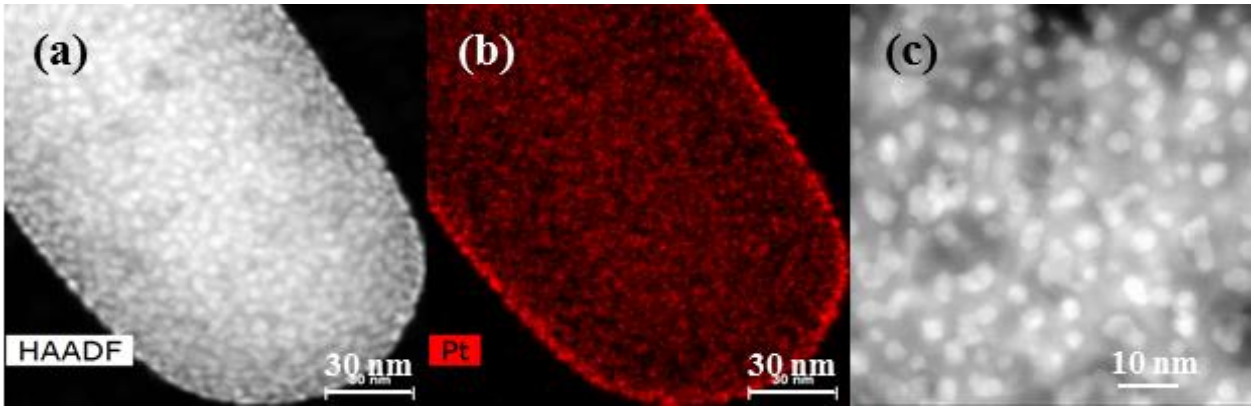

Figure 4-2. (a) HAADF image of tip of ALD-Pt LSMO nanorod. (b) Element mapping of Pt. (c) High magnification view of Pt nanoparticles on perovskite.

The catalytic propane oxidation performance was presented in **Figure 4-3**. The ZnO/LSMO nano-array catalys shows 50% conversion temperature (T_{50}) higher than 500˚C. As the Pt amount increases, the light-off curves of catalysts are shifted to lower temperature range. As presented, the T_{50} of xPt-LSMO catalysts were in the order of 0.1Pt LSMO (255˚C) > 0.01Pt LSMO (350˚C) > 0.001Pt LSMO (450˚C) > ZnO/LSMO (510˚C). Since 0.1Pt LSMO shows good low temperature activity, atomic-layer-deposited Pt LMO nano-array catalyst (ALD-Pt LSMO) was used as control sample. According to light-off curves, 0.1Pt LSMO and ALD-Pt LMO show comparable catalytic performance. And 0.1Pt LSMO also possesses much lower T_{90} (266˚C) than ALD-Pt LSMO (400˚C). The column diagram in **Figure 4-3 (b)** presents a more straightforward view of the influence of Pt loading amount on the activity of catalysts. The Pt concentration of catalysts was investigated using ICP-AES. With similar Pt concentration (5 g/L), 0.1Pt LSMO catalyst shows better catalytic activity than ALD-Pt LSMO.

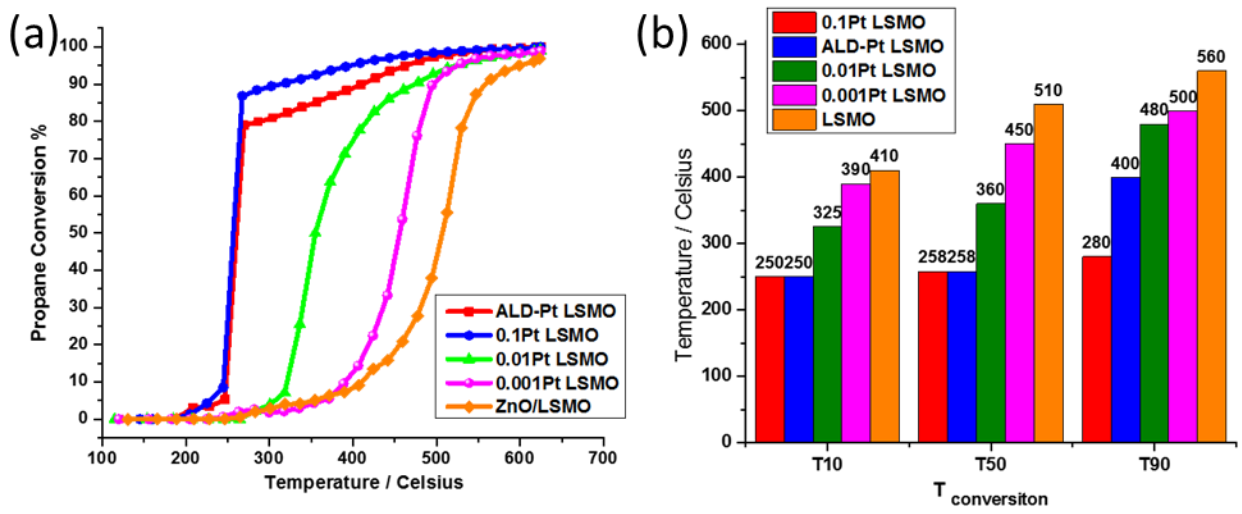

Figure. 4-3. (a) Propane oxidation performance of monolithic xPt-LSMO catalysts and ALD-Pt LSMO catalyst. (b) Column diagram of T_{10}, T_{50}, T_{90} for all the catalysts.

To study the hydrothermal stability 0.1Pt LSMO, the propane oxidation performance before and after hydrothermal aging of the same catalysts are collected and presented in **Figure 4-4**. The ALD-Pt LSMO shows severe activity deterioration with T_{50} increases from 255˚C (fresh) to 350˚C (aged) after 700˚C hydrothermal aging. And the performance is even worse after 800˚C hydrothermal aging. In comparison, 0.1Pt LSMO shows better stability than ALD-Pt LSMO even though activity deterioration also exists. The catalytic activity slightly deactivates with T_{50} increases from 255˚C (fresh) to 290˚C (aged). However, the catalytic performance of catalysts aged at 700˚C and 800˚C presents minor difference in terms of the T_{90}, which indicates that 0.1Pt LSMO is capable of bearing harsher hydrothermal condition.

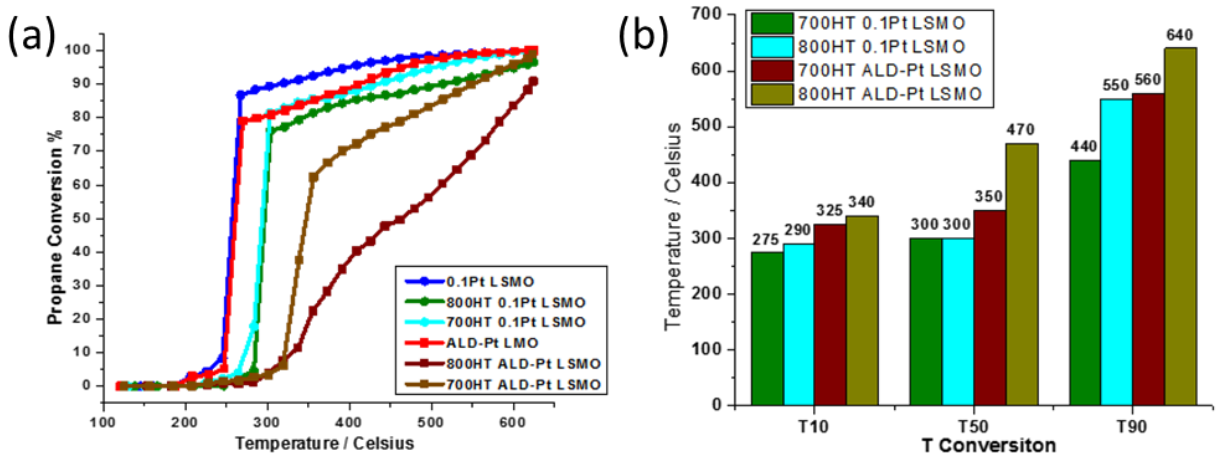

Figure 4-4. (a) Propane oxidation performance of 0.1Pt LSMO and ALD-Pt LMO catalysts before and after hydrothermal aging. Aging conditions: 800˚C for 50h and 700˚C for 100h. (b) Column diagram of T_{10}, T_{50}, T_{90} for all the catalysts.

The morphology changes of ALD-Pt LSMO before and after hydrothermal aging are presented in **Figure 4-5 (a)** and **(b)**. The ZnO/perovskite core/shell structure is destructed due to the partially disappearance of ZnO. However, the nano-array structure is still retained. The TEM result in (c) and (d) show the Pt nanoparticles in 0.1Pt LSMO before and after aging. The average diameter of Pt nanoparticles significantly increased from 1.5 nm to 4 nm after aging. However, the Pt nanoparticles still presents uniform distribution in perovskite shell. The interface between Pt nanoparticles and $La0.8Sr0.2MnO_3$ and the interface between $La0.8Sr0.2MnO_3$ and ZnO may play an important role in improving the hydrothermal stability of perovskite based monolithic catalysts. The $La_{0.8}Sr_{0.2}MnO_3$ is able to immobilize Pt nanoparticles and prevent Pt agglomeration. In addition, the nano-array structure supported by ZnO nanorod is able to prevent the collapse of $La0.8Sr0.2MnO_3$ nano-shell during the sintering in hydrothermal condition because individual nanorod is not in contact with each other. Besides the interface

effect, another possible reason for the better hydrothermal stability in 0.1Pt LSMO is the intelligent catalyst reported by scientists. [12, 13] The noble metal atoms may dissolve in and segregate out of perovskite structure lattice in oxidizing and reducing atmosphere. Therefore, it is possible some platinum was incorporated into perovskite lattice and segregate out during hydrothermal aging.

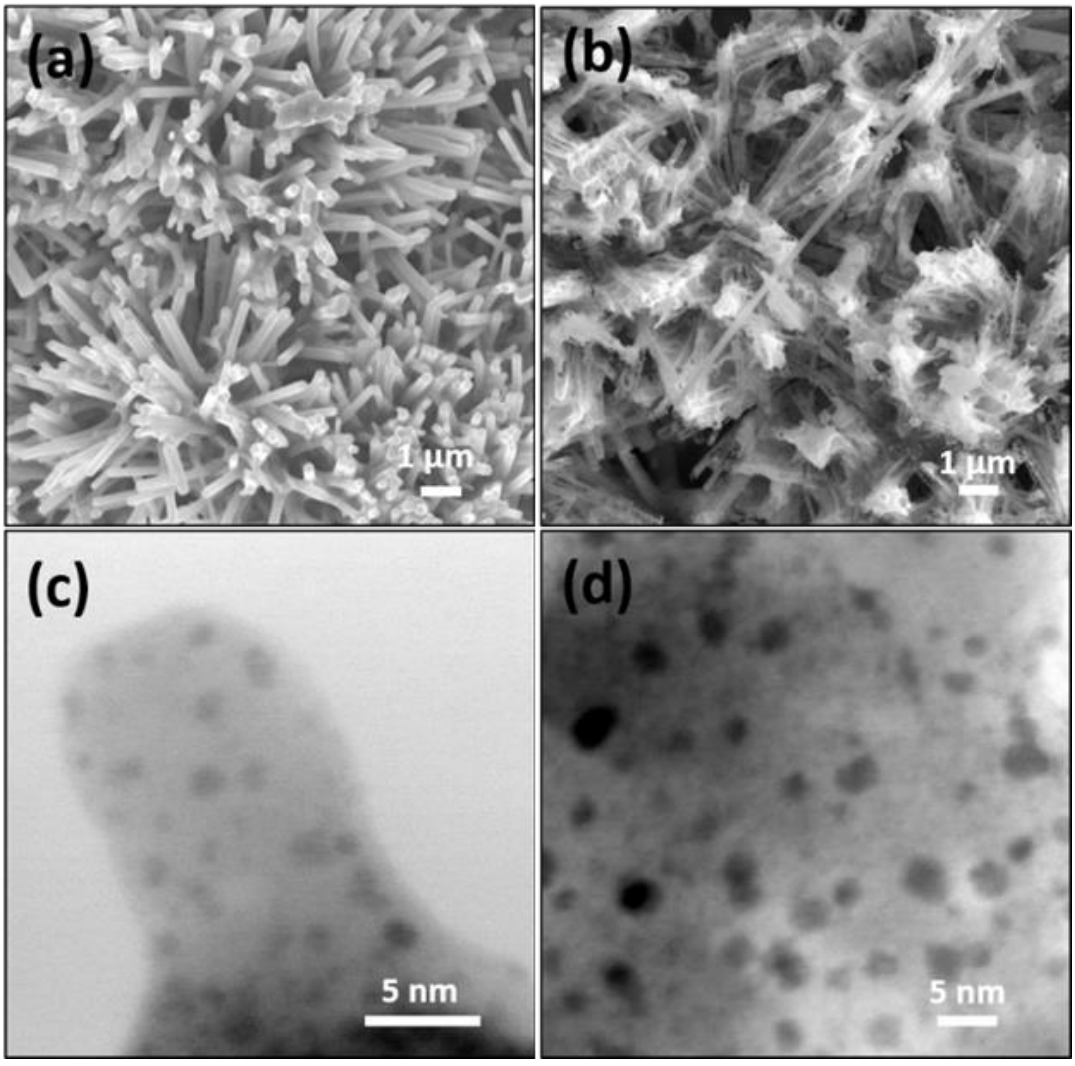

Figure 4-5. SEM images of ALD-Pt LSMO nano-array catalysts (a) before and (b) after hydrothermal aging. TEM images of Pt nanoparticles distribution of 0.1Pt LSMO nano-array catalysts (c) before and (d) after hydrothermal aging.

4.4: Conclusion

A novel synthetic approach was developed for fabricating Pt incorporated ZnO/$La_{0.8}Sr_{0.2}MnO_3$ core/shell nano-array catalysts through sol-gel co-deposition of platinum and $La_{0.8}Sr_{0.2}MnO_3$ on ZnO nano-array. The platinum was loaded on ZnO/$La_{0.8}Sr_{0.2}MnO_3$ as uniformly dispersed nanoparticles. The obtained xPt LSMO nano-array catalysts show improved catalytic activity for propane oxidation. And the activity is strongly related to the Pt loading amount on the catalysts. With similar Pt usage, 0.1Pt LSMO catalyst possesses comparable activity to ALD-Pt LSMO nano-array catalysts but much lower 90% conversion temperature. After the hydrothermal aging, both 0.1Pt LSMO and ALD-Pt LSMO catalysts show obvious deterioration of activity. However, 0.1Pt LSMO still retains decent catalytic activity with light-off temperature at 300°C. The good hydrothermal stability of 0.1Pt LSMO is originated from the interface between Pt nanoparticles and $La0._8Sr_{0.2}MnO_3$ and the interface between $La0._8Sr_{0.2}MnO_3$ and ZnO nanorod, which prevents the collapse of perovskite nanofilm and the agglomeration of platinum nanoparticles. We believe this integration strategy provides a new route for design and fabricating efficient noble metal/perovskite based nano-array catalysts with enhanced hydrothermal stability.

Reference

1. R. J. Farrauto, K. E. Voss, *Appl. Catal., B*, **1996**, 10, 29-51.

2. R. M. Heck, S. Gulati, R. J. Farrauto, *Chem. Eng. J.*, **2001**, 82, 149-156

3. Y. Teraoka, H. Fukuda, S. Kagawa, *Chem. Lett*., **1990**, 19, 1-4.

4. V.R. Choudhary, B.S. Uphade, S.G. Pataskar, *Fuel*, **1999**, 78, 919-921.

5. B. Viswanathan, *Catal. Rev.- Sci. Eng*. **1992**, 34, 337-354.

6. Y. Teraoka, K. Nakano, W. Shangguan, S. Kagawa, *Catal. Today*, **1996**, 27, 107-113.

7. L. Forni, I. Rossetti, *Appl. Catal., B*, **2002**, 38, 29-37.

8. S. Royer, D. Duprez, F. Can, X. Courtois, C. Batiot-Dupeyrat, S. Laassiri, H. Alamdari, *Chem. Rev.*, **2014**, 114, 10292-10368.

9. J. Chen, M. Shen, X. Wang, J. Wang, Y. Su, Z. Zhao, *Catal. Commun*., **2013**, 37, 105-108.

10. C. H. Kim, G. Qi, K. Dahlberg, W. Li, *Science*, **2010**, 327, 1624-1627.

11. Y. Guo, Z. Ren, X. Xiao, C. Liu, H. Sharma, H. Gao, A. Mhadeshwar, P.X. Gao, *Nano Energy*, **2013**, 2, 873–881.

12. Y. Nishihata, J. Mizuki, T. Akao, H. Tanaka, M. Uenishi, M. Kimura, T. Okamoto, N. Hamada, *Nature*, **2002,** 418, 164-167.

13. X. Li, C. Chen, C. Liu, H. Xian, L. Guo, J. Lv, Z. Jiang, P. Vernoux, *ACS Catal*. **2013**, 3, 1071-1075.

CHAPTER 5

Enhanced Metallic Nano-Pt Dispersion on Mesoporous Perovskite Nanotube Arrays for Efficient Low Temperature Propane Oxidation

3-D monolithically integrated mesoporous $LaMnO_3$-Pt nanotube array was prepared through hydrothermal growth, sol-gel deposition and acid etching combined approach. The mesoporous nanotube arrays exhibit significantly increased surface area compared to their core/shell nanorod arrays counterpart. Diluted acid etching inevitably removes partial lanthanum cations of $LaMnO_3$. The charge imbalance is neutralized by increased surface Mn^{4+} population, which not only improves the reducibility of nanotube arrays, but also increases the oxidation-resistance of surface dispersed Pt nanoparticles in oxidizing atmosphere. The $LaMnO_3$-Pt nanotube array with improved surface area and enhanced metallic Pt nanoparticles enable an enhanced low-temperature catalytic activity for propane oxidation.

5.1: Introduction

Monolithic catalysts, composed of honeycomb substrate and wash-coated powder-form catalysts on its channel surface, represents a unique class of functional devices that has been widely used in automotive emission control industry. Design of low cost and high efficiency catalysts with low temperature catalytic activity meets the urgent demand of low-temperature combustion technology towards ultra-fuel-efficient engines and combustors. [1] Perovskite materials (ABO_3), especially lanthanum based perovskite oxides, have been investigated as

potential substitutes of platinum-group metals (PGMs) catalysts since last century. [2] Due to the access of multiple valence states of cations and their capacity of accommodating substituting elements in structure lattice, perovskite oxides exhibit exceptional and tunable redox ability. [3] Many studies have been focused on their catalytic performance for oxidation reactions and NO reduction. [4, 5, 6] However, their activity for catalyzing oxidation reactions is still one or two orders of magnitude lower than PGMs. [7] Though some works tried to improve the activity of oxidation by introducing small amount of noble metal in perovskite, it is rather difficult to achieve high dispersion of noble metals through traditional impregnation method owing to the nature of low surface area of perovskite support. [8] To overcome this obstacle, new synthesis and decoration methods have been sought after lately to increase the dispersion of metal nanoparticles on perovskite. For example, atomic layer deposition (ALD) was developed as a new technique to obtain well dispersed platinum (Pt) nanocrystal on $SrTiO_3$ nanoparticles.[9] Doping noble metal atoms in perovskite structure lattice has been shown to enable an interesting concept of intelligent catalysts featuring high Pt dispersion, exceptional catalytic activity and stability. [10, 11] However, it remains a challenge to make these promising concepts adaptable with good industrial scalability and three-dimensional (3-D) substrate compatibility, which however represent a viable path towards practical production and application.

Recently, transition metal oxide nano-array integrated monolithic catalysts are emerging as a new class of catalytic converters for automotive emission control.[12, 13, 14, 15] The 3-D nano-array architecture provides a unique platform of multi-diversity to engineer catalysts with rational materials selection and structural design. [16] Meanwhile, surface acid treatment was reported as good method to improve the catalytic activity of perovskite oxides. [17, 18, 19] Surface acidity and basicity of support materials also poses strong influence on the catalytic performance of Pt/Pd

based catalysts by controlling the oxidation state of Pt/Pd in oxygen-rich atmosphere. [20, 21] Thus, design of high-efficiency perovskite/noble metal based catalysts may be realized by manipulating nanoscale structures and exploiting the nanoscale metal-support interaction.

Herein, by using wet chemical synthesis in conjunction with acidic nano-template etching process, large-scale mesoporous $LaMnO_3$ nanotube arrays highly dispersed with metallic Pt nanoparticles have been successfully integrated onto field-size cordierite honeycomb, forming an efficient and robust monolithic catalyst for low temperature propane oxidation. The diluted nitric acid etching process not only helps enable a novel class of perovskite nanotube arrays with well-defined geometry and mesoporosity, but also increases the surface acidity of $LaMnO_3$ and enhances the oxidation-resistance of metallic Pt nanoparticles. As a result, the mesoporous $LaMnO_3$-Pt nanotube array catalysts exhibit superior propane oxidation activity at low temperature with significantly enhanced reaction kinetics compared to the template core/shell nanorod array catalysts and pure $LaMnO_3$ powder wash-coated catalyst. This work demonstrates a new strategy for design of high performance monolithic devices towards efficient and robust catalytic emission control.

5.2: Experimental

The mesoporous $LaMnO_3$-Pt nanotube array was prepared through a combination of ZnO/$LaMnO_3$-Pt core/shell nanorod array synthesis and diluted nitric acid etching. The detailed procedure is described as below.

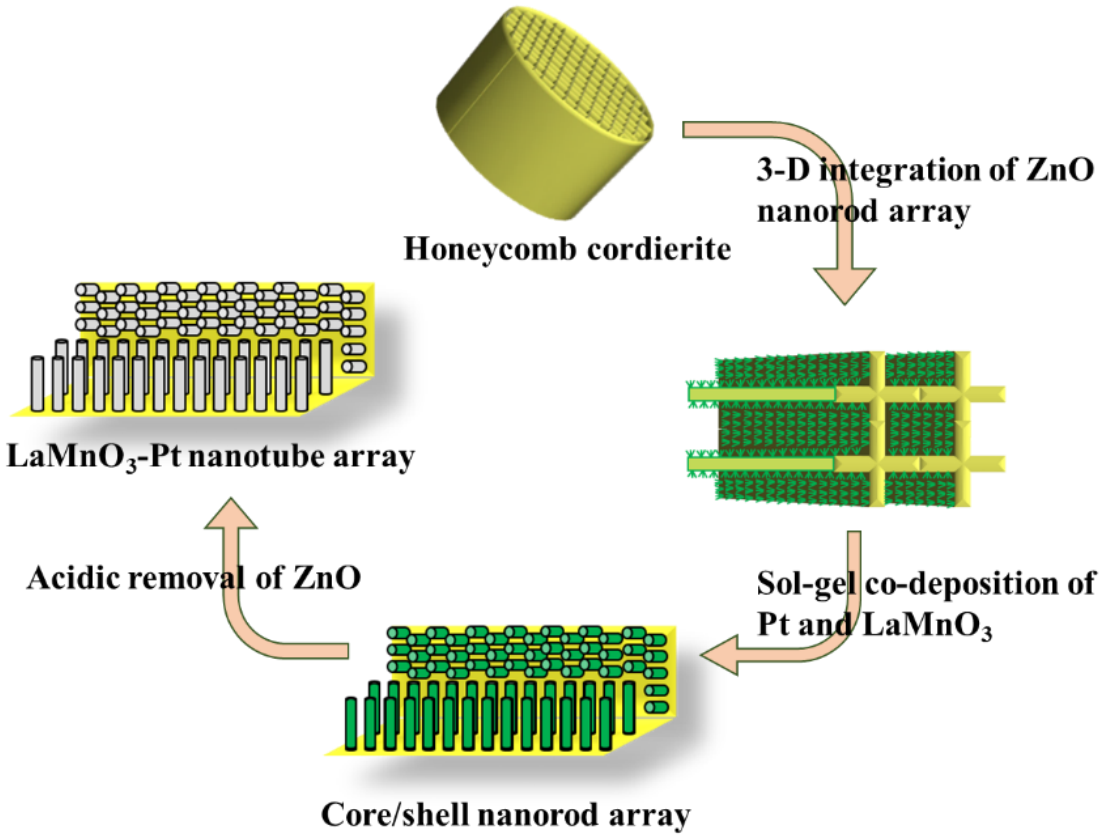

Figure 5-1. Schematic illustration of fabrication of 3-D monolithic $LaMnO_3$-Pt nanotube array catalyst.

5.2.1: ZnO/$LaMnO_3$-Pt Core/shell Nanorod Array Integration

First, the ZnO nanorod array was conformably grown on monolithic cordierite via the hydrothermal based batch process as reported previously. [22] Perovskite film deposition: The perovskite type sol-gel solution was prepared by dissolving stoichiometric lanthanum(III) nitrate hexahydrate, strontium nitrate, manganese(II) nitrate tetrahydrate and tetraamineplatinum(II) nitrate in 20 ml N,N-Dimethylformamide (DMF) under sonication. In the other bottle, 2 g polyvinylpyrrolidone (M.W 55,000) and 0.5 ml diethanolamine were dissolved in 20 ml DMF.

Then the two types of solution were mixed under vigorous stir at 60˚C and the solution rapidly turned dark brown. The achieved solution was aged for 24 hours. ZnO nano-array integrated cordierite was used for perovskite nanofilm deposition to achieve the ZnO/$LaMnO_3$-Pt core-shell nanostructure. First, one piece of sample was submerged in sol-gel solution under sonication. Then the sample was removed and transferred to a commercial kitchen use microwave oven for drying under the microwave irradiation. This deposition process was repeat for a few cycles until the desired loading amount (15%) was acquired. The sample was calcined at 350˚C in air to remove partial surfactant between each deposition cycles. The final calcination was carried out at 700˚C for 2 h with ramping rate of 5˚C/min.

5.2.2: Mesoporous $LaMnO_3$-Pt Nanotube Array Fabrication

Nitric acid was slowly added into 800 ml DI water to adjust the PH between 2 and 3. One piece of monolithic catalyst with dimension of 10 × 20 channels was slowly submerged and immobilized in the acid solution. The solution was under vigorous stir to generate steady flow through the channels of monolithic catalyst. The catalyst was taken out after 30 minutes and rinsed with DI water. Then it was dried in oven overnight for further usage.

5.2.3: Catalytic propane oxidation

Propane oxidation was carried out using gas chromatography–mass spectrometry (GC-MS). A piece of catalysts (5 × 5 channels) with channel length of 1 cm was wrapped by intumescent mat purchased from Corning Inc. and inserted in quartz tube (ID 1"). The quartz tube was placed in a tubing furnace to be heated. The testing gas was composed of 0.78% C_3H_8, 8% O_2 and 91.22% N_2 with total flow rate of 250 sccm. The space velocity of test was controlled to be

60,000 h^{-1}. For each test cycle, the catalyst was firstly activated in testing gas stream at 400°C for 10 mins so that the intumescent mat can completely block the open space between catalyst and quartz tube. After the catalyst was cooled down to room temperature, the furnace temperature started to ramp up with rate of 2°C/min. The temperature of testing gas entering catalyst was probed by thermal couple and the outlet gas was analyzed by GC-MS.

5.3: Result and Discussion

Figure 5-2 (a) shows the ZnO nano-array and $LaMnO_3$-Pt nanotube array integrated monoliths. **Figure 5-2 (b)** presents the SEM image of uniformly grown ZnO nanorod array with average length of 5 μm on both sides of wall surface along substrate channels. With successful co-deposition of Pt and $LaMnO_3$ onto ZnO nanorod arrays under microwave-assisted deposition followed by high temperature calcination, 3-D ZnO/$LaMnO_3$-Pt core/shell nanorod array integrated honeycomb was assembled as shown in **Figure 5-2 (c)**. The inset enlarged SEM image displays the hexagon-shaped tips of core/shell nanorods. The roughness of $LaMnO_3$ shell coating on ZnO can be clearly observed. Pt loading was controlled by adjusting the original Pt precursor concentration in sol-gel solution. The catalysts with molar ratios of Pt to Mn of 1% and 5% were denoted as 1LMO-R and 5LMO-R, respectively. The ZnO nanorod core in the obtained core/shell nano-array catalysts were readily removed in diluted nitric acid, leaving mesoporous $LaMnO_3$/Pt nanotube structures with well-ordered configuration (1LMO-T, 5LMO-T) as presented in **Figure 5-2 (d)**. The atomic ratio obtained from Energy Dispersive X-ray (EDX) spectroscopy indicates a La-cation deficiency in both 1LMO-T and 5LMO-T samples due to the diluted acid etching. [17]

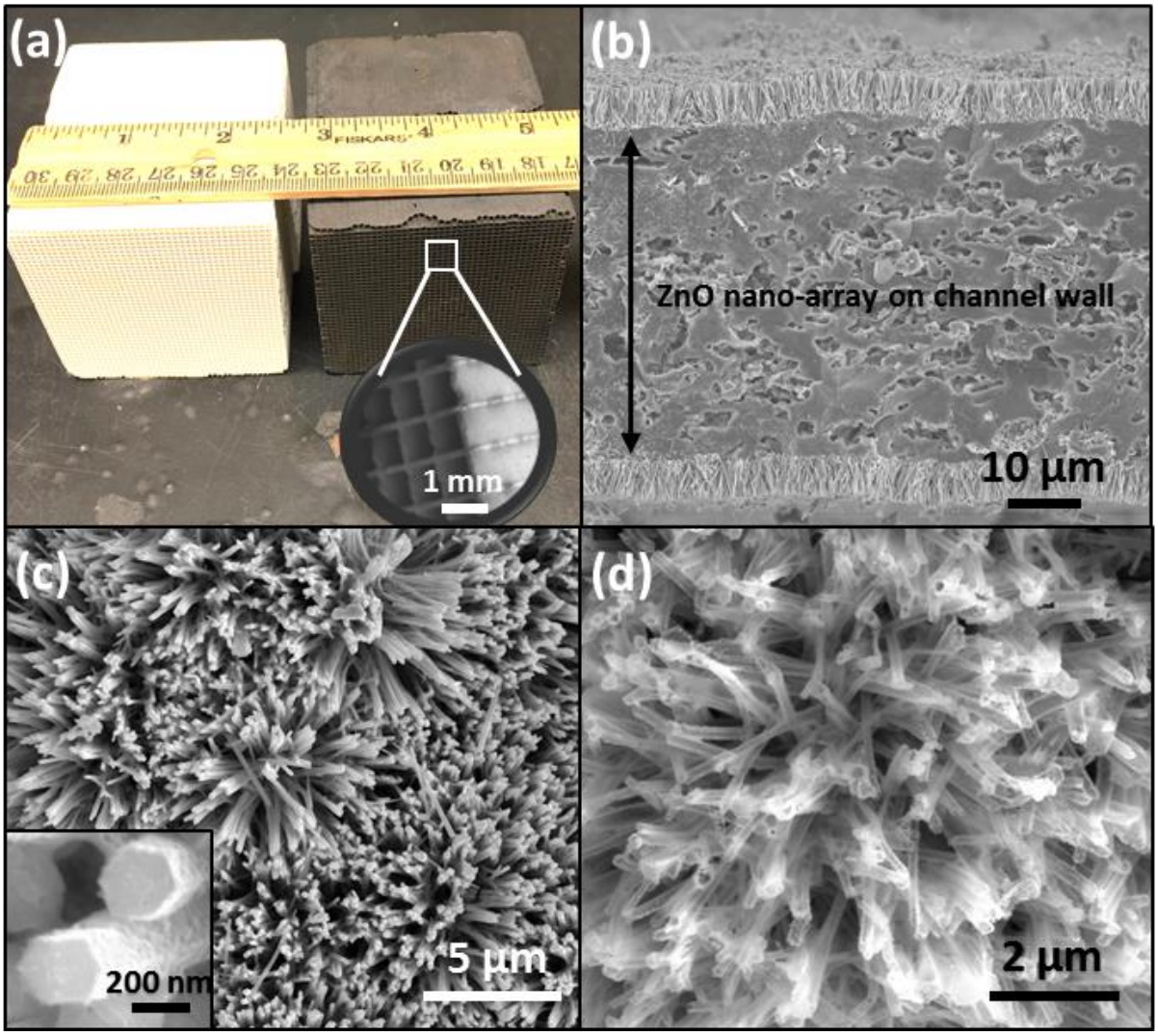

Figure 5-2 (a) A photograph of 2.5″ × 2.5″ × 3″ ZnO nanorod array (white) and 5LMO-T nanotube array (black) integrated monolithic catalysts, and an inset SEM image of honeycomb substrate channels. (b) SEM image of uniform ZnO nanorod arrays rooted on honeycomb channel wall surface. (c) Top view SEM image of 5LMO-R core/shell nanorods array and a zoom-in view of hexagonal tips of core/shell nanorods. (d) Top view SEM image of 5LMO-T nanotube array after removal of ZnO nanorod cores through diluted nitric acid treatment.

As can be seen in a typical TEM image of 5LMO-R shown in **Figure 5-3 (a)**, ZnO nanorod is wrapped by a ~40 nm thick of $LaMnO_3$ coating composed of nanoparticles. After ZnO removal using nitric acid, the $LaMnO_3$ nanoparticles of 20 ~ 40 nm were revealed in the 5LMO-T nanotube sample (**Figure 5-3 (b)**). Due to the removal of ZnO nanorod cores, mesopores formed at the interspaces of individual $LaMnO_3$ nanocrystallites. The enlarged TEM image shows uniformly distributed Pt nanoparticles on $LaMnO_3$, with a size range from 1 to 3 nm as revealed by the HAADF image. The measured interplanar spacing (0.285 nm) in **Figure 5-3 (d)** is closely matched to the {2-11} planes in $LaMnO_3$, but slightly larger than standard value of 0.271 nm (JCPDS # 82-1152). This can be attributed to the weakened Mn-O bonds as a result of lattice distortion induced by La cation deficiency. [23] **Figures 5-3 (f-g)** present the elemental mapping in selected area of 5LMO-T nanotube sample, revealing no obvious phase segregation in the mesoporous $LaMnO_3$ nanotubes.

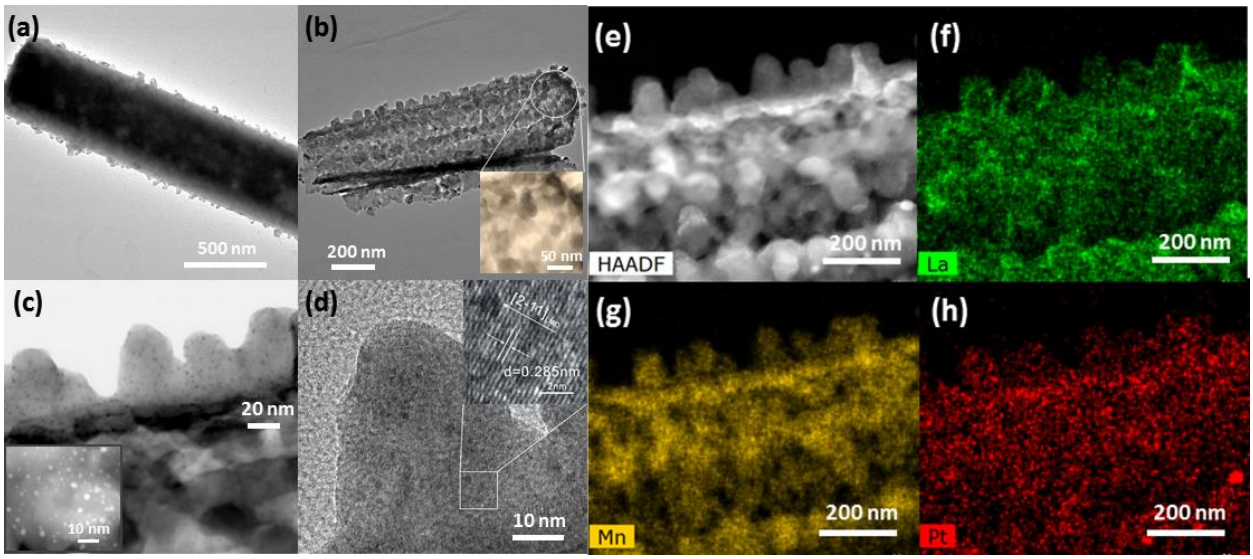

Figure 5-3 Typical TEM images of (a) a ZnO/$LaMnO_3$-Pt nanorod. (b) a mesoporous $LaMnO_3$/Pt nanorod. (c) an HAADF image revealing the $LaMnO_3$ nanoparticles with uniformly dispersed Pt nanoparticles. (d) HRTEM investigation of $LaMnO_3$ after acid treatment. (e)~(h) Elemental mapping of La, Mn and Pt under the HAADF mode.

XRD patterns (**Figure 5-4**) for nano-array catalysts before and after acidic removal of ZnO indicate there is no additional phase formed. The Pt is too little to be detected. However, there are still strong peaks assigned to ZnO in nanotube array catalyst, which may be originated from the residual ZnO at the bottom of nano-array that was not completely removed.

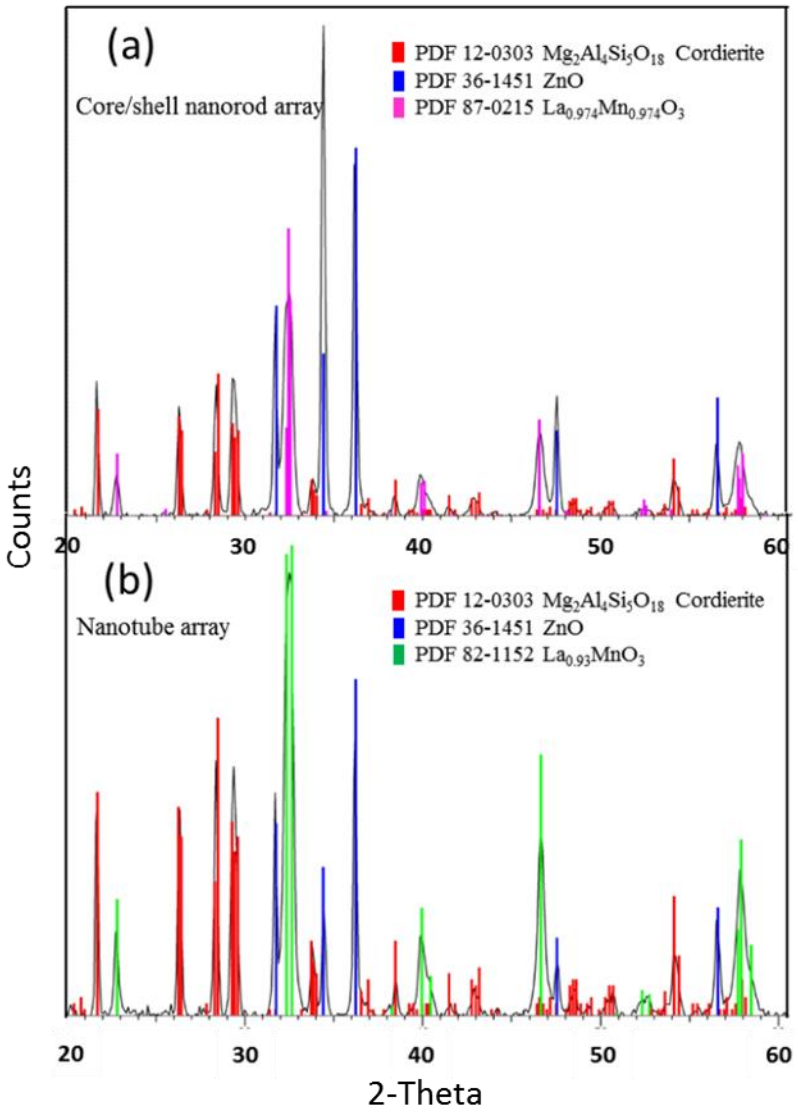

Figure 5-4. XRD patterns of (a) 5LMO-R and (b) 5LMO-T catalysts composed of cordierite substrate, zinc oxide and lanthanum manganese oxide.

The catalytic propane oxidation over nano-array catalysts was performed in $C_3H_8/O_2/N_2$ mixture stream (0.78%/8%/91.22%) with a fixed space velocity of 60,000 h^{-1}. The detailed testing condition was described in supplementary information. T_{10} (temperature at which 10% conversion of propane into carbon dioxide is achieved), T_{50} and T_{80} for nano-array catalysts and

pure $LaMnO_3$ powder wasch-coat catalyst are summarized in a bar chart as displayed in **Figure 5-5 (c)**. The 5LMO-T nanotube sample possess the lowest T_{10}, T_{50} and T_{80} as well as the lowest activation energy compared to other nano-array catalysts, and moreover a very fast reaction kinetics with only 9°C difference between T_{50} and T_{80}. As shown in **Figure 5-5 (a)**, the catalytic activity was found to be dependent on Pt loading of the catalysts. The light-off curves for 5LMO-R and 5LMO-T with relatively higher Pt loading amount shifted to lower temperature by 50°C in comparison with the 1LMO-R and 1LMO-T nano-array samples. The comparison of core/shell nanorod arrays and nanotube array catalysts reveals that acidic removal of ZnO nanorods gave rise to a significant enhancement of low temperature catalytic activity, shifting the light-off curves towards lower temperature range with enhanced kinetics and reduced activation energy (**Figure 5-5 (b)**).

Table 5-1. Summary of propane oxidation activity of the nano-array integrated monolithic catalysts under study and their physical and chemical characteristics. (S_{BET} calculation excludes contribution from honeycomb substrate)

Catalysts	5 mol% Pt + $ZnO/LaMnO_3$ nanorods	5 mol% Pt + $LaMnO_3$ nanotubes	1 mol% Pt + $ZnO/LaMnO_3$ nanorods	1 mol% Pt + $LaMnO_3$ nanotubes	$LaMnO_3$
Denotation	5LMO-R	5LMO-T	1LMO-R	1LMO-T	LMO
E_a [kJ/mol]	129.2	81.3	132.2	108.0	197.8
T_{10} (˚C)	261	227	308	294	342
T_{50} (˚C)	289	254	333	311	482
T_{80} (˚C)	327	263	438	332	525
Pt (g/L)	2.55	2.65	0.54	0.50	0
S_{BET} (m^2/g)	8.6	24.6	9.5	28.5	-
Mn^{4+} : Mn^{3+} (XPS)	0.56	0.82	0.46	0.65	-
La : Mn (EDX)	0.98	0.84	0.98	0.86	-

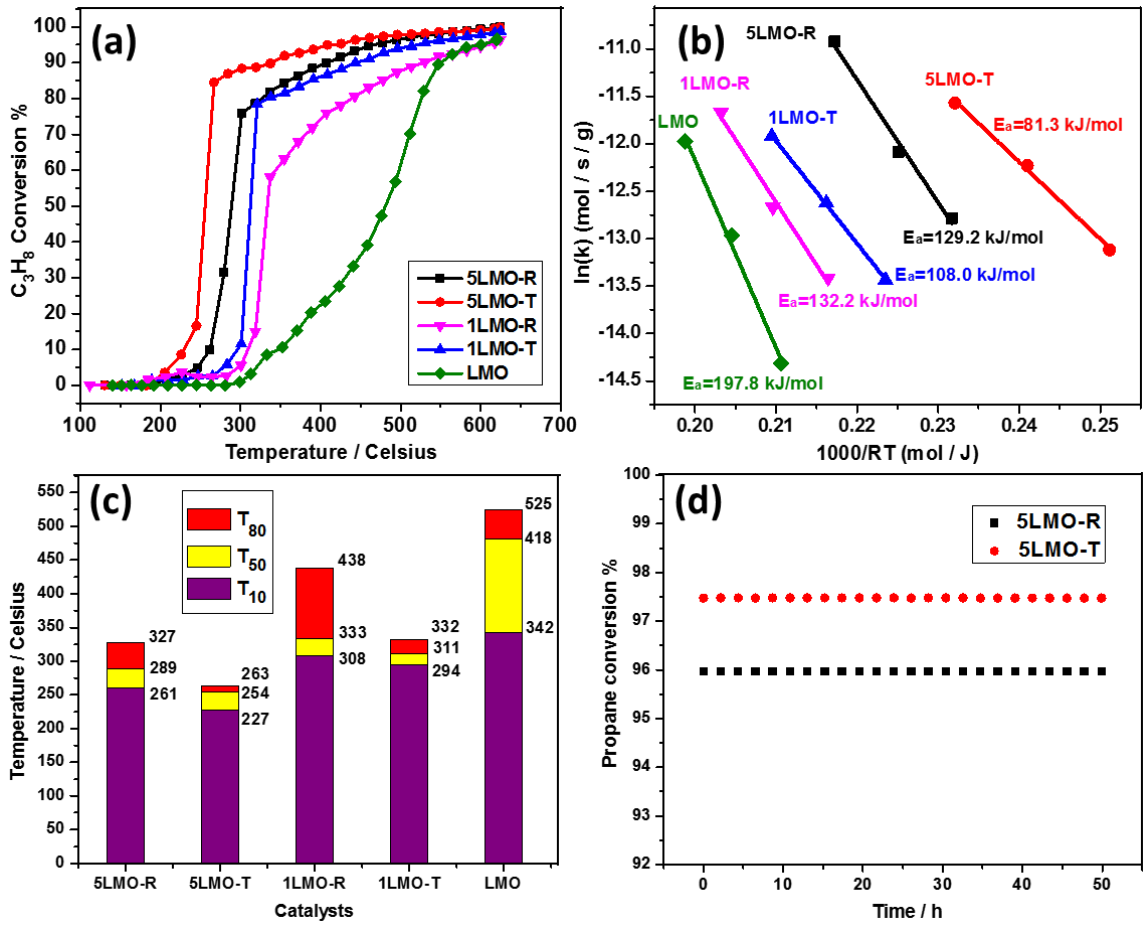

Figure 5-5. Catalytic propane oxidation performance of $LaMnO_3$/Pt based nano-array integrated monolithic catalysts: (a) propane oxidation conversion as a function of temperature; (b) Arrhenius plot of different catalysts; (c) bar charts of T_{10}, T_{50} and T_{80} of different catalysts; (d) hydrothermal stability of 5LMO-R and 5LMO-T during test at 400°C for 50 hours.

In order to identify the reasons for activity enhancement in the nanotube array catalysts after acid removal of ZnO nanorod cores, various physico-chemical characterizations were performed. Figure 5-6 (a) compares the pore diameter distribution before and after ZnO nanorod core removal. Two major increases were observed in pore volumes in 5LMO-T in contrast to 5LMO-

R. Specifically, a new one is revealed in the pore diameter range of 7 nm-20 nm, in which no pore volume was found in 5LMO-R. This variation further confirms the formation of mesoporous nanotube structure in consistency with the TEM observation in Figure 5-3. The other pore volume increase is of a size range of ~100 nm-600 nm. This pore diameter range matches to the diameter range of ZnO nanorods, indicating the hollow nanotube structures due to the successful removal of ZnO nanorod cores. As a result, the surface area of nano-array catalyst increases from 8.6 and 9.5 m^2/g for 5LMO-R and 1LMO-R, respectively, to 24.6 and 28.5 m^2/g for 5LMO-T and 1LMO-T, respectively. As the support for Pt, nanotube array structures with high surface area not only favor Pt dispersion, but also enhance phase interactions between solid catalysts and gas reactants. On the other hand, the exposure of internal surface of nanotubes provides additional gas-solid interfaces, which facilitate propane adsorption on active sites and increases the average residence time. Although surface area plays an important role in catalytic reactions, the resistance to high temperature sintering may be a major concern, especially when water steam is involved, i.e., under hydrothermal condition. To test the hydrothermal stability, we conducted the test over nanotube array catalysts under a gas stream at 500°C for 50h. After the aging, surprisingly both 5LMO-R and 5LMO-T nano-array catalysts sustained with good oxidation activity without deactivation detected, as revealed in **Figure 5-5 (d)**. This clearly demonstrated that the hydrothermal stability of $LaMnO_3$ nano-array catalysts was not compromised even after removal of ZnO nanorod cores. The good thermal stability of porous nanotube array can be partially ascribed to well-defined $LaMnO_3$ nano-array configuration. The individual nanotube and the open space among them are able to help prevent the pore collapse. Moreover, the interfaces between $LaMnO_3$ and Pt nanoparticles may also play an important role in stabilizing the catalytic active sites. For instance, in **Figure 5-3 (c)**, the 1-3 nm Pt

nanoparticles may be embedded within the 20-40 nm $LaMnO_3$ nanoparticles, which could help stabilize the structures and retain activities after aging.

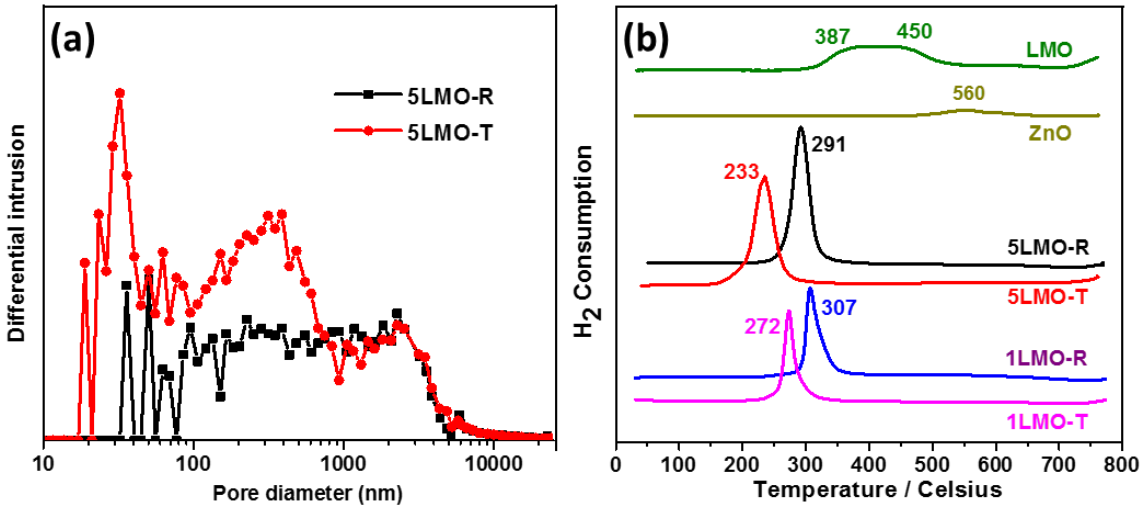

Figure 5-6. (a) Pore size distribution of before (5LMO-R) and after (5LMO-T) acidic removal of ZnO nanorod cores in the ZnO/$LaMnO_3$-Pt core/shell nanorod array integrated catalysts; (b) Temperature programed reduction profile of different catalysts under hydrogen exposure (H_2-TPR).

To further study the catalytic activity of different nano-array catalysts, temperature programmed reduction under H_2 (TPR-H_2) was carried out to study the variation of reducibility originated from acidic removal of ZnO nanorods. As shown in **Figure 5-6 (b)**, the reduction region for pure $LaMnO_3$ is a broad peak consisting of two shoulders. The one at lower temperature (387°C) is assigned to removal of oxygen within the perovskite lattice. The other one is correlated with the reduction of Mn^{4+} to Mn^{3+}. [24, 25] For all the Pt incorporated 5LMO-R, 1LMO-R, the reduction peaks are narrowed and shifted to lower temperature region by 159°C

and 217°C respectively compared to pure LMO. This variation might be caused by promoted reduction of Mn^{4+} by dissociatively adsorbed hydrogen on Pt nanoparticles, indicating the hydrogen spillover occurrence on the surface of Pt nanoparticles. [26, 27] Compared to 1LMO-R (307 ˚C), the reduction temperature of 5LMO-R (291˚C) is further lowered due to the increased Pt loading. For both 5LMO-T and 1LMO-T, it is noted that the reduction peaks are shifted to lower temperature ranges compared to 5LMO-R and 1LMO-R. This might be due to the higher reducibility of Mn^{4+} in mesoporous nanotube arrays than those in their core/shell nanorod array counterparts. [28]

X-ray photoelectron spectroscopy (XPS) was used to investigate the electronic structure change of nano-array catalyst surfaces. Since the acid etching removes partial La cations in perovskite lattice along with ZnO nanorods and lowers the ratio of La: Mn on the surface of perovskite, charge imbalance caused by the loss of La cations can be neutralized by increase of either Mn^{4+} or forming more surface oxygen vacancies. As shown in **Figures. 5-8 (a)** and **(b)**, the surface Mn^{4+}/ Mn^{3+} ratio was significantly increased in 5LMO-T compared to 5LMO-R sample. The surface enrichment of Mn^{4+} was also consistent to enhanced reducibility of nanotube arrays in H_2-TPR result as mentioned above. However, the amount of surface oxygen vacancy was not boosted after acid etching. According to the O_2-TPD profiles in **Figure 5-7**, the low temperature (<500°C) desorption that can be correlated with surface adsorbed oxygen (O_{ads}) is not enhanced in 5LMO-T. However, the peak shows up in 5LMO-T at 624°C can be assigned to surface lattice oxygen (O_{latt}). The increased mobility of surface lattice oxygen in mesoporous nanotube arrays enables them to desorb more easily compared to core/shell nanorod array catalysts. Moreover, this result can be confirmed by the molar ratio of O_{ads} : O_{latt} in XPS result, which decreases from 5LMO-R to 5LMO-T as indicated in **Figures 5-8 (e)** and **(f)**. Thus, it can

be concluded that the loss of La cations resulted from acid etching was compensated by increase of Mn^{4+} population rather than forming more oxygen vacancies on the surface of $LaMnO_3$.

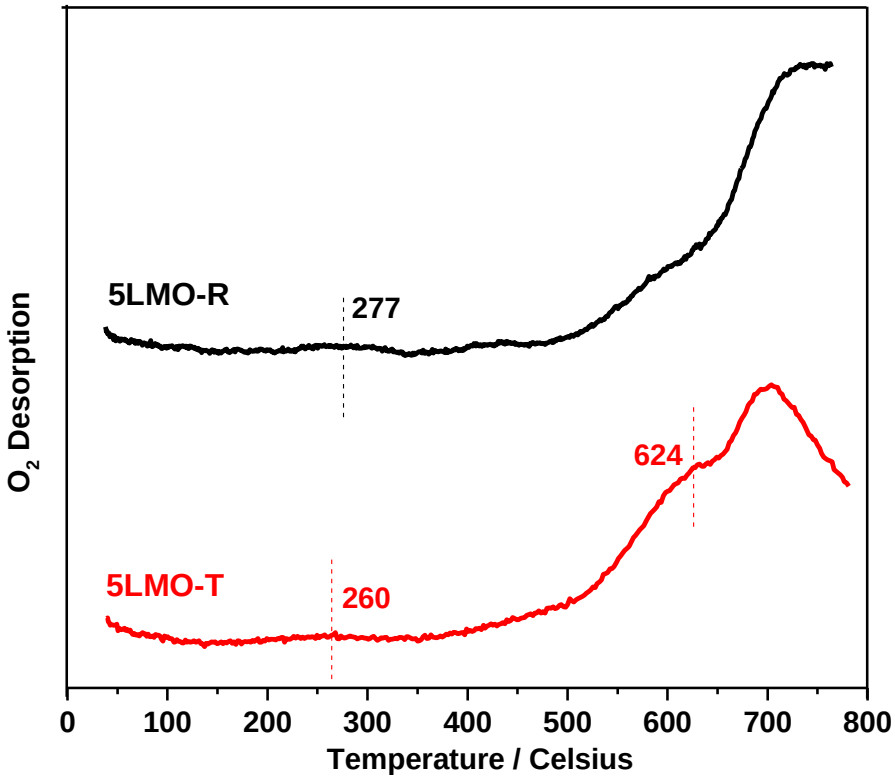

Figure 5-7. O_2-TPD profiles for 5LMO-R and 5LMO-T catalysts.

It is worth noting that these nano-array catalysts have to undergo an extended temperature range to achieve full conversion after ignition, a relatively flat plateau with slow kinetics shown in light-off curves (**Figure 5-5 (a)**). Propane oxidation reaction rate for Pt based catalysts is known to be strongly dependent on the propane molecule adsorption on Pt surface, with a critical factor in partial pressure of propane and oxygen in gas stream. [29, 30] Therefore, in propane-lean atmosphere, it is difficult to rapidly convert all propane molecules since the propane adsorption becomes increasingly difficult as the reaction proceeds with a low rate. However, this slope of

plateau is decreased for both 5LMO-T and 1LMO-T compared to their nanorods array counterparts. Therefore, the activity enhancement in nanotube array catalysts is not only associated with the lowered light-off temperature, but also with the improved kinetics of propane adsorption on catalysts' active sites as reaction proceeds. Since the TEM and ICP results have confirmed the consistence of Pt nanoparticle size, dispersion and total amount for 5LMO-R and 5LMO-T, the valance state of surface Pt acquired from XPS result should be a major concern for explaining activity improvement. Metallic Pt is known as more active than PtO and PtO_2 for propane combustion because dissociatively adsorbed oxygens on metallic Pt can facilitate the C-H bond scission. [31] The oxidation-resistance of Pt nanoparticles under oxidizing atmosphere can be dependent on the total electrophilic/electrophobic or acidic/basic properties of the support materials. More electrophilic and acidic supports result in less oxidized Pt. [21, 32, 33] Apparently, besides the ZnO nanorods and partial La cations, acid etching also removed the OH^- species on the surface of $LaMnO_3$ and lowered its surface basicity. [34] Moreover, the increased population of Mn^{4+} species on nanotube catalysts resulted in a more electrophilic support for Pt nanoparticles. Thus, the Pt nanoparticles on $LaMnO_3$ nanotube arrays possessed better oxidation resistance and maintained in less oxidized state in oxygen-rich propane oxidation reaction. As shown in **Figures 5-8 (c)** and **(d)**, the Pt_{4f} spectra can be decomposed into Pt^{4+}, Pt^{2+} and Pt^0 using the curve-fitting method. 5LMO-T possessed a strong peak assigned to Pt^0 at 70.8 eV [35] which was barely observed in 5LMO-R. In light of the competitive adsorption of propane molecule and oxygen on Pt surface as discussed above, maintaining the Pt nanoparticles in less oxidized state also favors the adsorption of propane molecules because the oxygen species on metallic Pt are dissociated as adatoms or adions on the surface. Subsequently the increase of overall reaction rate of propane oxidation can be expected.

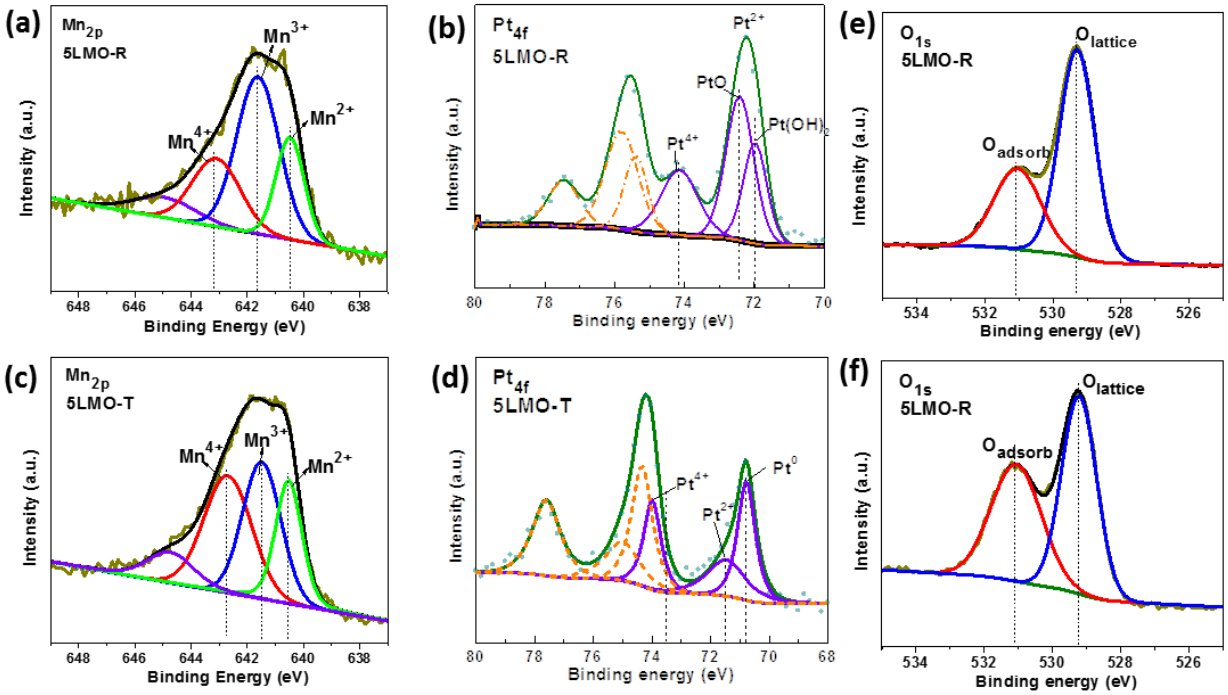

Figure 5-8 X-ray photoelectron spectra (XPS) of Mn_{2p} (a) (c), Pt_{4f} (b) (d) and O_{1s} (e) (f) for 5LMO-R and 5LMO-T catalysts, respectively.

5.4: Conclusion

In conclusion, mesoporous $LaMnO_3$/Pt nanotube array integrated monolithic catalysts has been successfully assembled by using surface acidic etching of ZnO/$LaMnO_3$-Pt core/shell nanorods array. The large surface area and as-obtained internal surface of nanotube array are kinetically favorable to gas-solid phase interaction and are hydrothermally stable in oxidation reaction. The La cations deficiency owing to acid etching is neutralized by increased surface Mn^{4+} population, which leads to more electrophilic/acidic $LaMnO_3$ support. The surface variation of $LaMnO_3$ support enables Pt nanoparticles to possess better oxidation resistance and results in more catalytically active metallic Pt in oxidation reactions. This work provides a new

route to improve the catalytic activity of perovskite/noble metal based catalysts through engineering the nanostructure and tuning the surface chemistry of perovskite, which can be extended to design other noble metal based heterogeneous catalysts.

Reference

1. M. Zammit, C. DiMaggio, C. Kim, C. Lambert, G. Muntean, C. Peden, J. Parks and K. Howden, "Future automotive aftertreatment solutions: the 150 C challenge workshop report," *US Drive Report*, Southfield, MI, 2013.

2. W. F. Libby, *Science*, **1971**, 171, 499-500.

3. T. Nitadori, T. Ichiki, M. Misono, Bull. Chem. Soc. Jpn., 1988, 61, 621.

4. H. Arai, T. Yamada, K. Eguchi, T. Seiyama, Appl. Catal., 1986, 26, 265-276.

5. T. Seiyama, *Catalysis reviews* , **1992**, 34, 281-300.

6. C. H. Kim, G. Qi, K. Dahlberg, W. Li, *Science*, **2010**, 327, 1624-1627.

7. S. Royer, D. Duprez, F. Can, X. Courtois, C. Batiot-Dupeyrat, S. Laassiri, H. Alamdari, Chem. Rev, **2014**, 114, 10292−10368.

8. L. Giebeler, D. Kießling, G. Wendt, *Chem. Eng. Technol*, **2007,** 30, 7, 889-894.

9. J. Enterkin, W. Setthapun, J. Elam, S. Christensen, F. Rabuffetti, L. Marks, P. Stair, K. Poeppelmeier, C. Marshall, *ACS Catal*, 1, **2011**, 629-635.

10. Y. Nishihata, J. Mizuki, T. Akao, H. Tanaka, M. Uenishi, M. Kimura, T. Okamoto, N. Hamada, *Nature*, **2002,** 418, 164-167.

11. Li, X; Chen, C; Liu, C; Xian, H; Guo, L; Lv, J; Jiang, Z; Vernoux, P, *ACS Catal.*, **2013,** 3, 1071-1075.

12. Y. Guo, Z. Ren, W. Xiao, C. Liu, H. Sharma, H. Gao, A. Mhadeshwar, P. Gao, *Nano Energy*, **2013,** 2, 873–881.

13. Z. Ren, V. Botu, S. Wang, Y. Meng, W. Song, Y. Guo, R. Ramprasad, S. Suib, P. Gao, *Angew. Chem. Int. Ed*., **2014,** 53, 1-6.

14. S. Chen, W. Song, H. Lin, S. Wang, S. Biswas, M. Mollahosseini, C. Kuo, P. Gao, S. Suib, *Appl. Mater. Interfaces*, **2016,** 8, 12, 7834-7842.

15. S. Du, W. Tang, Y. Guo, A. Binder, E. Kyriakidou, T. Toops, S. Wang, Z. Ren, S. Hoang, P. Gao, *Emission Control Science and Technology*, **2017,** 3, 18-39.

16. S. Wang, Z. Ren, Y. Guo, P. Gao, *CrystEngComm,* **2016,** 18, 2980-2993.

17. K. Huang, X. Chu, L. Yuan, W. Feng, X. Wu, X. Wang, S. Feng, *Chem. Commun*, **2014,** 50, 9200-9203.

18. Y. Peng, W. Si, J. Luo, W. Su, H. Chang, J. Li, J. Hao, J. Crittenden, *Environ. Sci. Technol*., **2016,** 50, 6442–6448.

19. B. Zhao, R. Ran, L. Sun, X. Guo, X. Wu, D. Weng, *RSC Adv*., **2016,** 6, 69855-69860.

20. Y. Yazawa, N. Takagi, H. Yoshida, S. Komai, A. Satsuma, T. Tanaka, S. Yoshida, T. Hattori, *Appl. Catal. A*, **2002,** 233, 103–112.

21. Y. Yazawa, H. Yoshida, T. Hattori, *Appl. Catal. A*, **2002,** 237, 139-148.

22. S. Wang, Z. Ren, W. Song, Y. Guo, M. Zhang, S. L. Suib, P. X. Gao, *Catal. Today*, 2015, 258, 549, 555.

23. W. Si, Y. Wang, Y. Peng, J. Li, *Angew.Chem.* , **2015,** 127, 8065 –8068.

24. J. Chen, M. Shen, X. Wang, J. Wang, Y. Su, Z. Zhao, *Catal. Commun.*, vol. 37, pp. 105-108, 2013.

25. S. Ponce, M. A. Pena, J. L. G. Fierro, *Appl. Catal., B* , **2000,** 24, 193.

26. C. Li, Y. Lin, *Appl. Catal., B,* **2011,** 107, 284-293.

27. L. Giebeler, D. Kießling, G. Wendt, *Chem. Eng. Technol*., **2007,** 30, 889-894.

28. Y. Liu, H. Dai, Y. Du, J. Deng, L. Zhang, Z. Zhao, C. Au, *J. Catal.*, **2012,** 287, 149-160.

29. L. Ma, D. Trimm, C. Jiang, *Appl. Catal., A,* **1996,** 138, 275-283.

30. M. Avila, C. Vignatti, C. Apesteguía, T. Garetto, *Chem. Eng. J.*, **2014,** 241, 52-59.

31. R. Burch, M. Hayes, *J. Mol. Catal. A: Chem*., **1995,** 100, 13-33.

32. H. Yoshida, Y. Yazawa, T. Hattori, *Catal. Today,* **2003,** 87, 19-28.

33. Y. Yazawa, N. Kagi, S. Komai, A. Satsuma, Y. Murakami, T. Hattori, *Catal. Lett.*, **2001,** 72, 157-160.

34. S. Sugunan, V. Meera, *React. Kinet. Catal. Lett*., **1997**, 62, 327-332.

35. N. Singhania, E. Anumol, N. Ravishankar, G. Madras, *Dalton Trans*., **2013,** 42, 15343-15354.

36. Y. Wang, H. Arandiyan, J. Scott, M. Akia, H. Dai, J. Deng, K. Aguey-Zinsou, R. Amal, ACS Catalysis. **2016**, 6, 6935−6947.

CHAPTER 6

Hydrothermal Based Scalable Continuous Flow Synthesis of ZnO Nanorod Arrays in 3-D Ceramic Honeycomb Substrate

Scalable and cost-effective synthesis and assembly of technologically important nanostructures in three-dimensional (3D) substrates hold keys to bridge the demonstrated nanotechnologies in academia with industrially-relevant scalable manufacturing. In this work, using ZnO nanorod arrays as an example, a hydrothermal based continuous flow synthesis (CFS) method is successfully used to integrate the nano-arrays in the multi-channeled monolithic cordierite. Compared to batch process, CFS significantly enhances the average growth rate of nano-arrays by 125%, with the average length increasing from 2 μm to 4.5 μm giving rise to the same growth time of 4 hours. The precursor utilization efficiency in the CFS is significantly enhanced by 9 times compared to that of batch processes by preserving the majority of precursors in recyclable solution. Computational fluid dynamic simulation suggests a steady-state solution flow and mass transport inside the channels of honeycomb substrates, giving rise to steady and consecutive growth of ZnO nano-array with average lengths of 10 μm in 12 h. With the demonstrated scalable synthesis upon commercial monolithic cordierite, we believe CFS to be a promising industrial-relevant integration strategy to fabricate metal oxide nano-array based monolithic devices for various environmental and energy applications.

6.1: Introduction

One-dimensional (1-D) nanostructures, such as nanorods, nanowires and nanotubes, have been widely reported showing excellent properties in heterogeneous catalysis. [1, 2, 3] The

predominantly exposed catalytically reactive crystal planes enable 1-D nanostructured catalysts to exhibit enhanced activity in catalytic reactions. [4, 5] The Scalable assemblies of 1-D metal oxide nanostructures, such as ZnO, TiO_2, MnO_2, and Co_3O_4, into well-defined three-dimensional (3-D) nano-arrays with a tailored geometric c, onfiguration represent a unique strategy to pursue high-performance functional devices targeting a variety , of energy and environment applications. [6, 7, 8, 9] Among the various synthetic approaches of 1-D metal oxide nano-arrays, bottom-up based hydrothermal approaches possess advantages of being environmental benign, cost-effective, and convenience for low temperature operation. [10] Recently, continuous flow of reaction solution over substrate was widely studied to facilitate growth of 1-D nanostructure array on flat substrates. Such continuous flow assisted growth features significantly enhanced reaction rate compared traditional batch processes.[11, 12, 13, 14, 15] However, there are no reports of continuous flow synthesis on integrating 3-D substrate with 1-D nanostructure array. Traditionally, hydrothermal based nano-array integration on structure-complicated substrate is mainly hindered by the difficulty of mass transport within confined space, resulting in poor coverage of nano-array throughout whole substrate. Though mechanical agitation has been proven to be an effective method for fabricating large-scale ZnO nanorod arrays on 3-D honeycomb substrates in traditional batch processes, [16] the poor growth rate, low precursors utilization efficiency, and high yield of free precipitates impose critical challenges to enable batch processes to meet the requirements of industrial-relevant scalable manufacturing. Furthermore, mass transport in space-confined substrate channels becomes more and more critical when the length of the substrate is gradually enlarged. Therefore, the development of 3-D functional nano-array devices calls for more favorable and more feasible integration approach.

Herein, we introduce a hydrothermally based continuous flow synthesis (CFS) method to grow uniform ZnO nanorod arrays on 3-D honeycomb substrates, which features low cost, high growth efficiency, and scalable integration.

6.2: Experimental

The precursors and substrate for continuous flow synthesis are the same as described in Chapter 3. However, the experimental setup is significantly different from traditional batch process.

6.2.1: Precursors, Substrate and Setup

Zinc acetate dihytrate [$Zn(CH_3COO)_2 \cdot 2H_2O$, 219.49 $g \cdot mol^{-1}$] and Hexamethylenetetramine ($(CH_2)_6N_4$, HMT, 99%) were purchased from Fisher Scientific without further purification. Zinc acetate is crystalline white powder. HMT is a crystalline, heterocyclic organic compound. Both of the chemicals are highly soluble in water. They are used in hydrothermal synthesis of ZnO nanorod arrays on 3-D honeycomb cordierite. The 3-D cordierite monolithic substrates were obtained from Corning (Product No.600/2). The hydraulic diameter of substrate channels is 0.97 mm and cell density is 600 cpsi. Masterflex L/S pumps (115VAC) and silicone tubing L/S 16(Platinum) used in continuous flow synthesis were provided by Cole-Parmer.

6.2.2: Hydrothermal based Continuous Flow Synthesis

Continuous flow synthesis is described as two major steps: (1) ZnO seed layer deposition upon wall surfaces of multi-channeled monolithic substrates and (2) hydrothermal growth of large-scale ZnO nanorod arrays. The seed layer enables the hydrothermal synthesis to bypass the nucleation step and facilitate the heterogeneous growth of nano-array on substrate. First, a monolithic cordierite substrate was rinsed with ethanol and DI water to remove surface impurities and grease. Then the multi-channeled substrate was vertically submerged under 20 mM zinc acetate ethanol solution and kept under sonication for 30 seconds. Then the substrate was dried in an oven at 150°C for 10 minutes. This seeding process was repeated for 10 cycles. The final treatment was performed at 350°C for 5 hours to facilitate further crystallization of ZnO seeds.

In the second step, ZnO nanorod array growth was carried out using the experimental setup as depicted in Figure 6-1. The growth solution was prepared by dissolving equal molar amounts of zinc acetate and HMT (12.5mM) in DI water. The honeycomb cordierite substrate was vertically mounted and stabilized in a glass reactor with Teflon tape blocking the open space between the substrate and the reactor. The reactor was incubated in a water bath at 90°C. Two peristaltic pumps were used to generate a steady flow in the solution circulation. The liquid level of growth solution in the reactor was maintained at 4 cm above the substrate. Before the outflow solution was pumped back into the solution reservoir, an ice-water bath was used to cool down the used solution below 50˚C, and a filter was mounted on reservoir to eliminate the precipitates formed in solution. Contrast experiments were conducted using a mechanical agitation assisted batch process as reported.[16] The experimental conditions are listed in **Table 6-1**. In the other

series of CFS with different pumping flow rates (10, 20, 30 ml/min·cm^2), 1000 mL solution in total was used for 12 h hydrothermal growth.

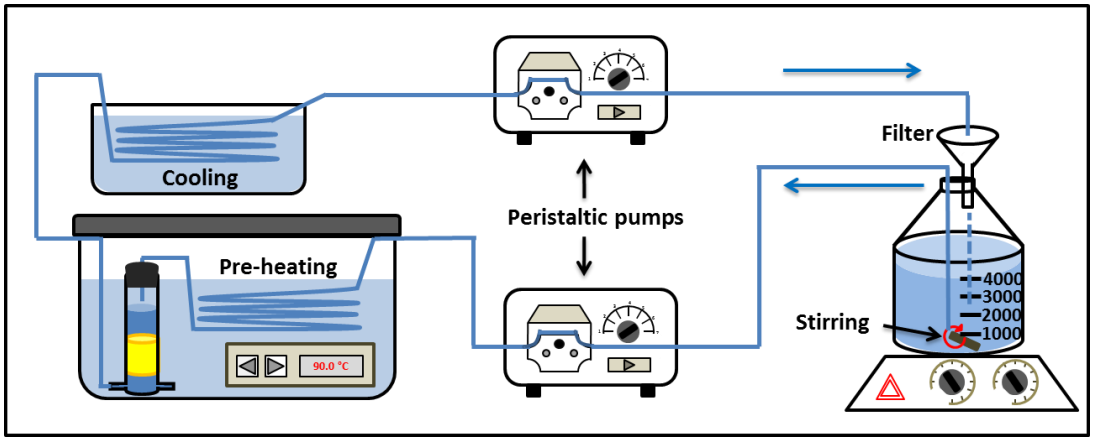

Figure 6-1. Experimental setup of the CFS method

Table 6-1. Reaction conditions of batch process and continuous flow synthesis.

	Denotation	Solution concentration (mM)	Solution usage (ml)	Growth temperature (°C)	Growth time (h)	Stir rate & pumping rate
Batch	S1	12.5	600	90	4	600 rpm
CFS	S2	12.5	600	90	4	3.3 ml/min·cm^2

6.2.3: Computational Fluid Dynamic

Computational fluid dynamics (CFD) was employed to study the flow field inside the substrate channels. The flow analysis was performed using ANSYS Fluent 15.0, which is a commercial CFD solver suitable for a wide variety of compressible and incompressible flow problems. The solution fluid was modeled as a homogeneous, incompressible, Newtonian fluid with density of ρ = 998.2 kg/m3 and dynamic viscosity of μ = 1.003 × 10−3 kg/m·s. Incompressible Navier−Stokes equations were used to describe momentum conservation using the finite-volume method. The SIMPLE scheme was adopted for pressure−velocity coupling and a second order scheme was used for spatial discretization.

6.3: Result and Discussion

The structure and morphology of as-grown ZnO nanorod array on cordierite honeycomb substrate after continuous flow synthesis was investigated and confirmed by an array of spectroscopies. Shown in **Figure 6-2 (a)**, the X-ray diffraction pattern (XRD) of ZnO nanorod array integrated monolith sample is consistent to ZnO (PDF 36-1451) and cordierite (PDF 12-0303) from Joint Committee on Powder Diffraction Standards (JCPDS) without the detection of any impurity. The intensity of (100), (002) and (101) peaks indicate the successful growth of ZnO nanorod on the cordierite substrate. **Figure 6-2 (b)** presents a cross-sectional Scanning Electron Microscope (SEM) view of vertically rooted ZnO nanorod array on the wall surface of cordierite substrate and **Figure 6-2 (c)** shows the Transmission Electron Microscope (TEM) image of a brunch of ZnO nanorods. The densely packed ZnO nanorod array exhibits well-

ordered alignment and possesses an average length of 6.5 µm and diameter of 260 nm. The characterization confirms that pure ZnO nanorod array was successfully grown on cordierite honeycomb substrate through hydrothermal based continuous flow synthesis method.

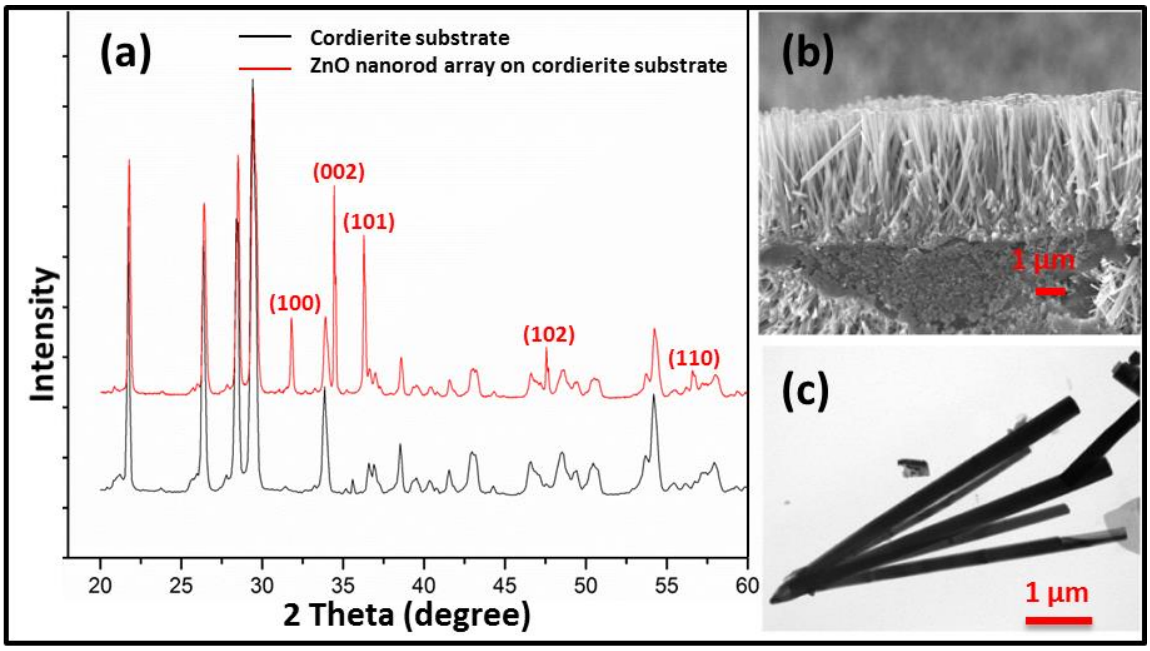

Figure 6-2. (a) X-ray diffraction patterns of bare cordierite honeycomb substrate and ZnO nanorod array integrated cordierite honeycomb substrate. (b) SEM image of cross-sectional view of ZnO nanorod array rooted on the wall surface of substrate, which was obtained via CFS with pumping flow rate of 20 ml/min. (c) Bright field TEM image of a brunch of ZnO nanorod from (b).

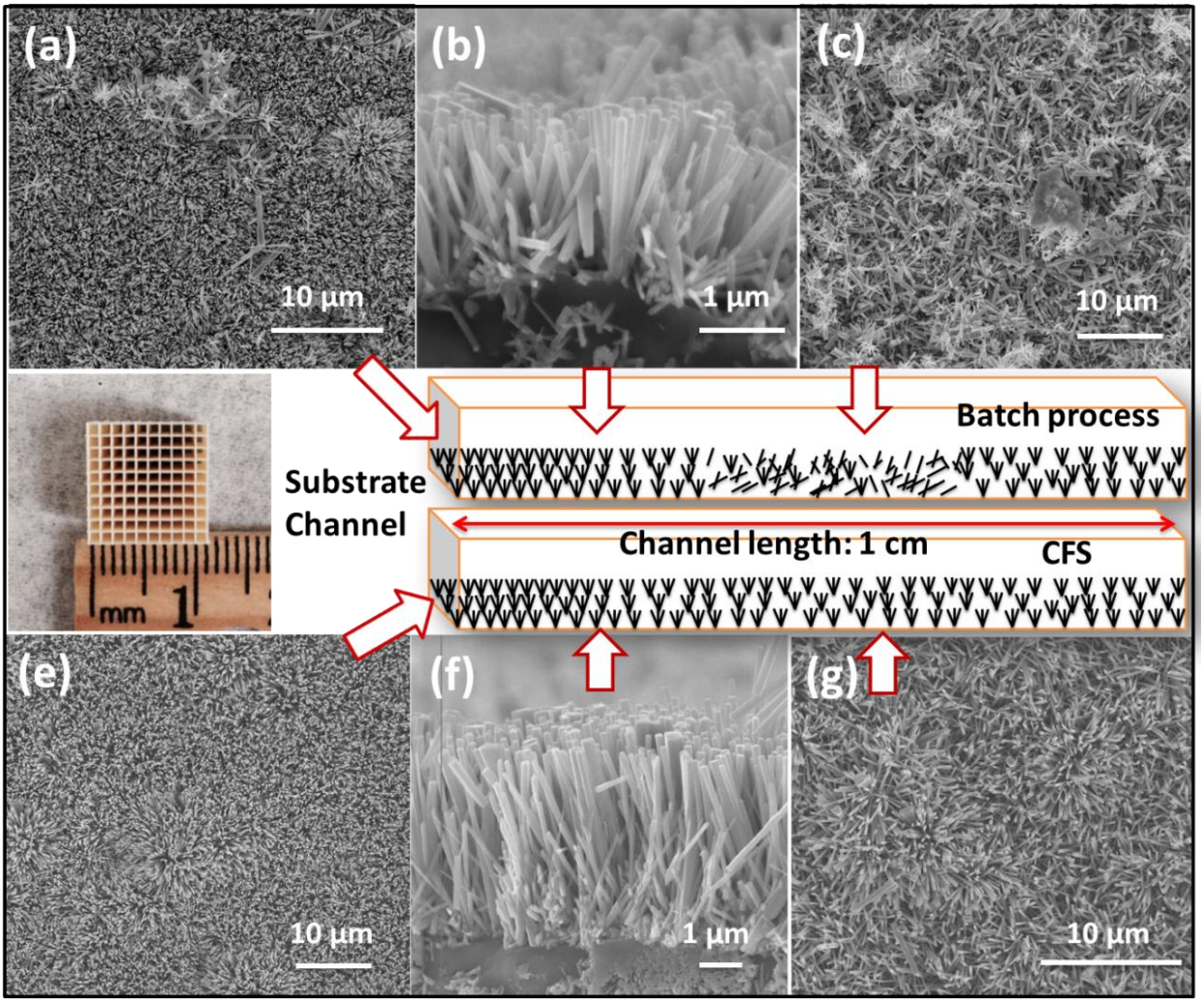

Figure 6-3. SEM images of typical ZnO nano-array obtained from batch process (sample 1) (a) top view and (b)cross-section view near channel ends, (c) top view of middle area of channels; And ZnO nano-array grew using the CFS method (sample 2) (e) top view and (f) cross-section view near channel ends, (g) top view of middle area of channels.

In the case of batch process, ZnO nanorod array in the end area possesses good alignment and uniform distribution (**Figure 6-3 (b)**). In the middle of the channels, characteristics of ZnO nanorod array severely deteriorated, as demonstrated by the sparse ZnO nanorods and randomly

distributed precipitates. Compared with sample1, sample 2 obtained from the CFS method exhibits well-organized morphology in terms of overall nanorod array uniformity and alignment. The density of ZnO nano-array on wall surface in the middle area (**Figure 6-3 (c)** and **(g)**) was significantly improved and the widespread precipitates distributed on nanorod array in sample 1 had not been detected in sample 2.

It is well known that ZnO nanorods growth is in favor of existing seeds rather than nucleation in homogeneous solution. [17] However, the favorable growth of ZnO nanorods cannot completely prevent nucleation from occurring in solution. At initial stage of reaction in the batch process, small particles formed in solution due to nucleation might penetrate the channels with solution flow induced by magnetic stirring. As time goes on, some particles were stuck in the channels as long as they reached certain sizes, leading to severely competitive growth to ZnO nanorod array on the wall surface and rapidly lowering the solution concentration. This scenario was highlighted in the middle area of channels where precipitates preferentially aggregated (**Figure 6-3 (c)**), evidenced by randomly oriented and sparse ZnO nanorod array on the wall surface as well as the ZnO particles and bulk precipitates. For CFS method, the vertically mounted substrate enabled these ZnO particles to be easily drained out of substrate along the channels and filtered before solution was injected into the solution reservoir. The heating and cooling circulation system confined the ZnO nanorod array growth within the glass reactor and minimized the consumption of precursors by ZnO particles growth, which subsequently guaranteed most precursors in solution to be supplied to the growth of ZnO nanorod array. From the growth efficiency point of view, the average length of nanorods in the channel ends area was increased from 2 μm for sample 1 (**Figure 6-3 (b)**) to 3.5 μm (**Figure 6-3 (f)**) for sample 2, and

the ZnO nanorod array weight loading ratio as improved from 4.3% (sample 1) to 5.5% (sample 2), indicating that CFS possesses relatively faster average growth rate of ZnO nanorods.

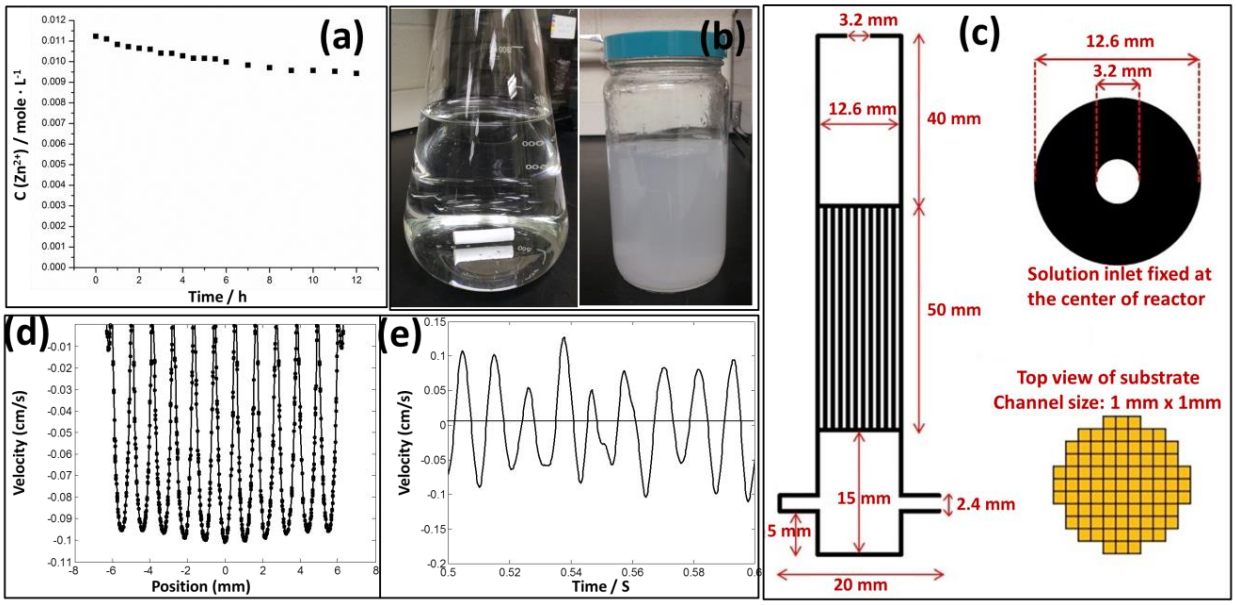

Figure 6-4. (a) [Zn^{2+}] concentration of solution reservoir varies as a function of time in CFS; (b) solution reservoir after 20 min growth time (Left: transparent solution for CFS and Right: cloudy solution for batch process); (c) geometric parameters employed in fluid dynamic simulation; (d) computational flow velocity versus position in CFS; (e) computational flow velocity versus time in batch process.

To further understand the mechanism of improved ZnO nanorod array growth rate in the CFS method, CFD was introduced to demonstrate the flow field of different synthesis processes. Hydrothermal growth of ZnO nanorod array through batch process had been reported showing that zinc ion concentration sharply decreased at the initial stage (< 2h), after which it decayed to zero slowly and linearly with increasing time.[18] It has been well known that hydrothermal growth

of ZnO nanorods array on substrate is inevitably accompanied by the formation of ZnO particles derived from homogeneous nucleation. In traditional batch process, ZnO particles are drastically enlarged at the expense of rapid consumption of precursor, which leads to severe competitive growth of ZnO particles in the solution and ZnO nanorod arrays on honeycomb substrate. However, the CFS showed no such sharp decrease in the monitored variation of zinc ion concentration. As shown in **Figure 6-4 (a)**, the zinc ion concentration decays at a slow but steady pace throughout the entire reaction time. And after 12 h reaction, 84% of original zinc ion was preserved in growth solution. This result can be ascribed to the unique heating-cooling-filtering circulation in CFS effectively eliminating the ZnO particles formed in solution and preventing them from further growth. As presented in **Figure 6-4 (b)**, the solution reservoir of CFS was still quite clear after 20-minute reaction time while the solution in the batch reactor has become completely cloudy.

The precursor utilization can be calculated by:

$$U = \frac{M_{(ZnO)load}}{M_{(ZnAc)consumed}} \qquad \textbf{Equation 6-1}$$

$M_{(ZnO)load}$: Mole of ZnO grown on monolithic substrate

$M_{(ZnAc)consumed}$: Mole of ZnAc had been consumed in reaction.

Based on Equation 1, the precursor utilization of CFS (25.7%) is almost 9 times that of the batch process (2.8%). The solution color variation and precursor utilization confirm that CFS possesses superior capability of suppressing the growth of ZnO particles in solution and reducing the undesirable by-product, and thus the precursor utilization efficiency for CFS is enhanced.

CFD simulations were further conducted to understand the non-uniformity growth different locations in the channels using CFS. The geometric parameters are presented in **Figure 6-4 (c)**.

The solution inlet with a diameter of 3.2 mm was considered to be infinitely close to solution line in the reactor and fixed aligned with the center of reactor's cross section. The substrate was compactly mounted in the reactor with solution both above and below it. The simulations use a non-uniform tetrahedral mesh with approximately 15 million cells between the inlet and outlet of the substrate. No-slip boundary conditions were applied to the walls and the inlet mass flow rate was 0.5 g/s (30 ml/min).

The CFD result in **Figure 6-4 (d)** presents a projective profile which depicted the solution flow velocities at the top plane of the substrate versus the distance to the center of substrate. The overall profile displays a symmetrical trend in which flow rate reaches peak at the center channels and gradually decreases approaching the marginal area, implying that slightly more reactants were being supplied to ZnO nano-array growth in center channels compared to marginal channels. For the CFD result of mechanical agitated batch process, the oscillating flow velocity induced by high-frequency-vibrating stirring bar easily causes particles aggregation in middle area of channels, which consequently leads to bulk precipitates after the initial stage of reaction. However, the CFD result of continuous flow synthesis shows a time-independent steady solution flow in each channel, favoring the consecutive mass transport of reactants within the space-confined channels. Consequently, distribution uniformity of ZnO nano-array along the channel is significantly enhanced, as evidenced by the well-grown nanorod array in middle area of the channels (**Figure 6-4 (g)**). The contrast of CFD results well explained the observed difference in nano-arrays' morphologies achieved via CFS and stirring agitated batch process.

As a low cost and efficient synthesis method, CFS holds great potential to solve the scale up problem in front of nano-array catalysts nanomanufacturing. Our first attempt of scaling up is focused on the length of monolithic device channel. We are trying to scale-up monolith substrate

in the length direction from 1 cm to 5 cm, and face a greatest challenge of uniformity of ZnO nanorod array throughout the entire channel length with such a limited diameter. It has been proved that the characteristics of ZnO nanorod array are essential to various growth parameters such as temperature, solution concentration, precursor and pH of the solution. [19, 20] However, in the continuous flow synthesis process, an inevitable concentration gradient is generated along the channels when solution flows through it. The pumping flow rate of solution thus was found to be a crucial parameter determining the uniformity of ZnO nanorod array. **Figure 6-5** shows SEM characterization result of large-scale ZnO nanorod arrays in a center channel of the monolithic honeycomb substrate using the CFS method. 4000 mL mixed zinc acetate and HMT solution with concentration of 12.5 mM was used to maintain the growth running for 12 hours with a fixed flow rate of 10 ml/min. The entire channel length was divided into 5 areas, where Area 1 was closest to the solution inlet and Area 5 near the outlet. Area 1 displays the best uniformity of ZnO nanorod array among the five areas, whereas Area 2 presents slightly reduced areal density ($5/\mu m^2$) compared to Area 1 ($6/\mu m^2$). In Area 3 and Area 4, poor areal density ($<1/\mu m^2$) and significant non-uniformity of ZnO nanorod array along the channel were observed. This scenario confirms that the remarkable solution concentration gradient is the reason that precursors were being consumed gradually in Area 1 and Area 2, making the solution concentration insufficient for Area 3 and Area 4 to achieve uniform growth of ZnO nanorod array. For Area 5, the areal density shows a rebound ($3/\mu m^2$) which contradicts previous description. This might be attributed to solution leakage through the space between the reactor wall and the substrate that supplied Area 5 with decent precursors for ZnO nanorods growth.

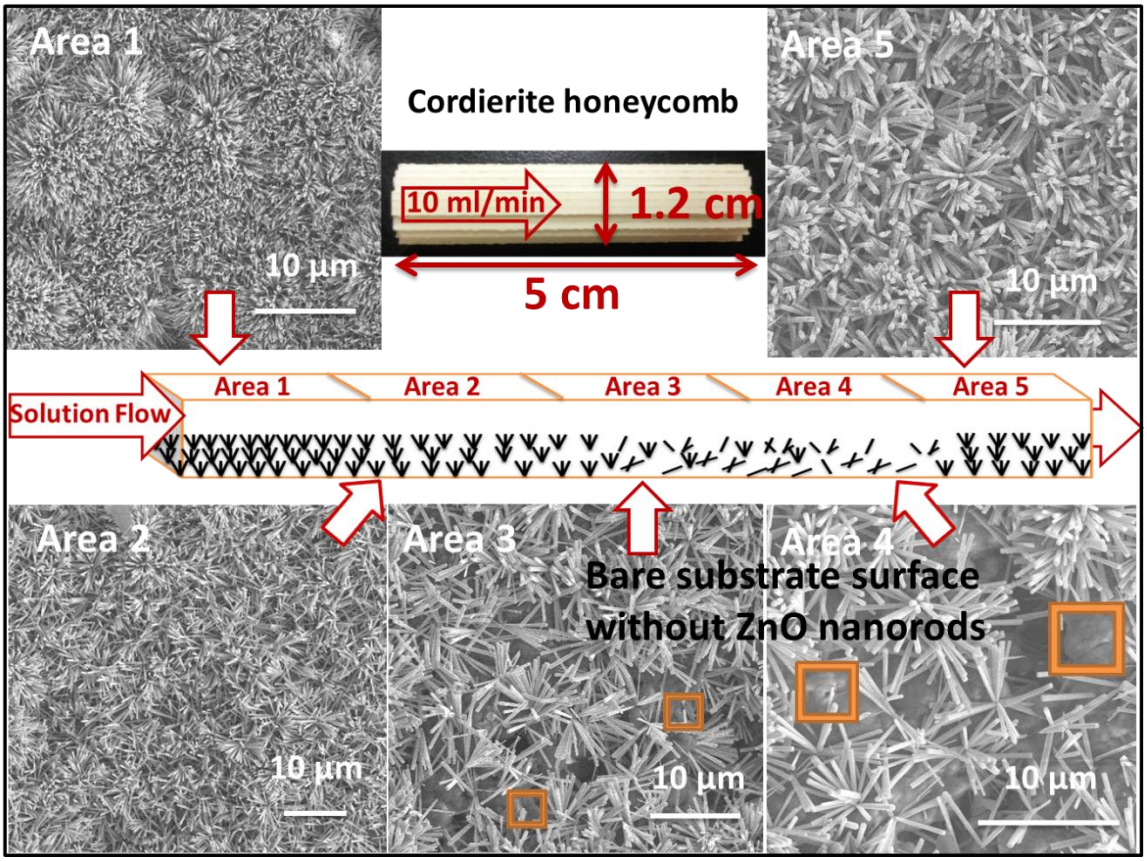

Figure 6-5. Geometry of monolithic honeycomb substrate (top) and SEM images of ZnO nanorod arrays in areas of a single center channel obtained via CFS with pumping flow rate of 10 ml/min.

In the following two batches of CFS, the pumping flow rates were increased to 20 ml/min and 30 ml/min, respectively, to guarantee that sufficient precursors can be supplied to Area 3 and Area 4 of the channels. The weight loading ratios of ZnO nano-array for these three batches were 4.2%, 7.58% and 10.1%, respectively, following the trend of the increasing flow rate. **Figure 6-6** presents top view and cross-sectional view SEM images of Area 3 and Area 4 of the substrates obtained from increased flow rates. In comparison to the result of 10 ml/min pumping rate, ZnO nanorod array obtained from 20 ml/min was more densely packed without any exposed bare

substrate surface. As the pumping rate increased to 30 ml/min, the density and alignment of ZnO nanorod array in these two areas were further improved. Though the enhancement derived from increasing pumping flow rate can be clearly observed, it is important to quantify these characteristics of ZnO nanorod arrays.

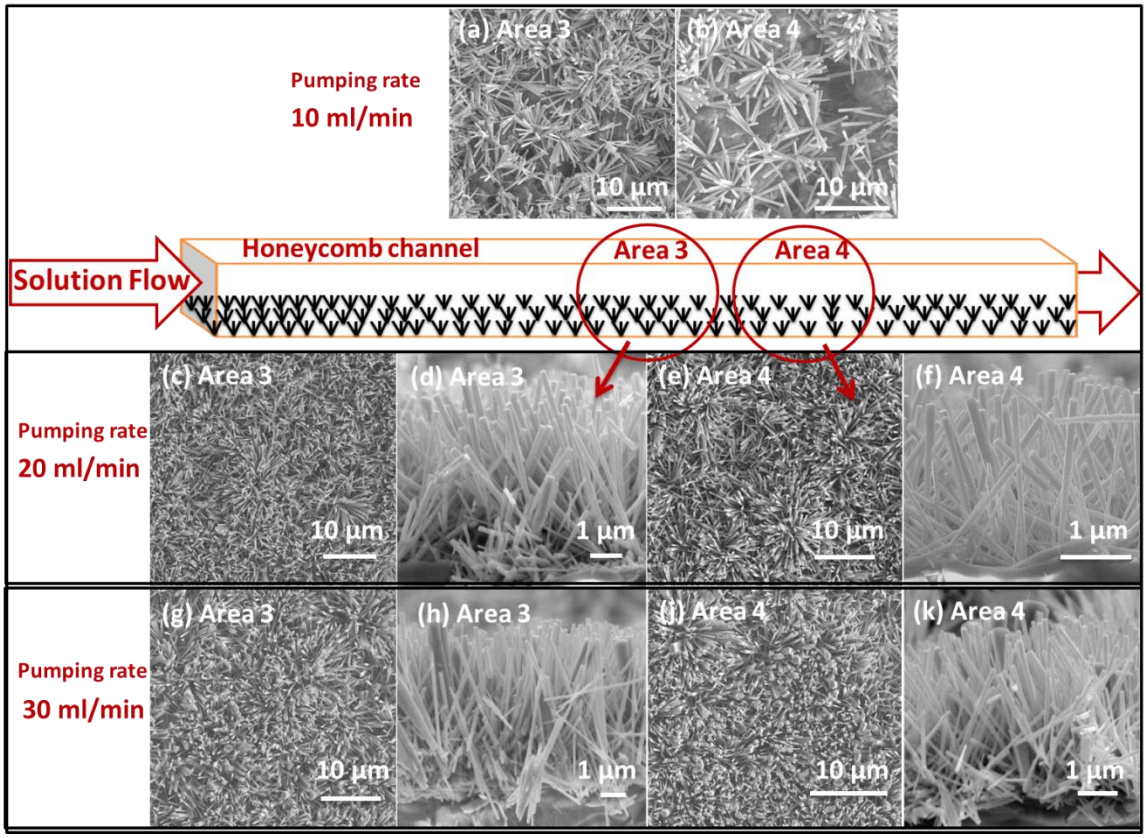

Figure 6-6. SEM images of ZnO nanorod array at Area 3 and Area 4 obtained with pumping flow rate of 10 ml/min (a, b), 20 ml/min (c, d, e, f) and 30 ml/min (g, h, j, k)

Table 6-2 lists the average length (AL), average diameter (AD) and average density of ZnO nanorod array in the five areas of the channels. ZnO nanorod array achieved from 30 ml/min flow rate displays greater overall average length (6.4 µm) and average density (5.2/µm^2)

compared to the result of 20 ml/min batch (5.2 μm) and (3.8/ μm^2). From the perspective of density uniformity, the standard derivation of nano-array's density for five areas decreased from 1.55 for batch 2 to 0.65 for batch 3, implying that the improved ZnO nano-array's density in Area 3 and Area 4 contributed to the enhancement of overall density uniformity.

Table 6-2. Summary of the nano-array geometric information obtained from CFS different flow rates.

Flow rate	Batch 2: 20 ml/min			Batch 3: 30 ml/min		
Characteristics	AL (μm)	AD (nm)	Average density (/μm^2)	AL (μm)	AD (nm)	Average density (/μm^2)
Area 1	6.5	260	6	8	270	6
Area 2	4.8	269	3.8	7.5	260	5.8
Area 3	4.5	280	2.5	6	270	4.8
Area 4	4.4	290	2.2	4.5	260	4.5
Area 5	4.6	220	4.5	5	250	5
Overall	5.2	258	3.8	6.4	262	5.2

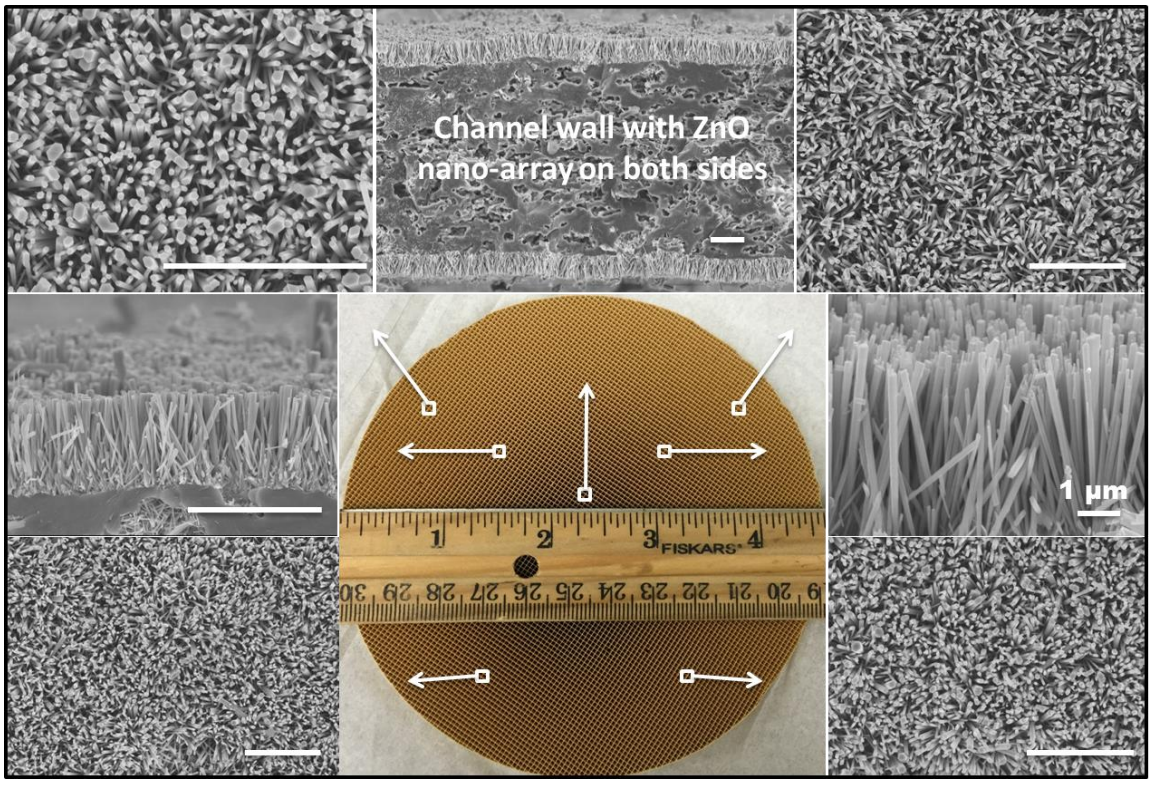

Figure 6-7. Uniformly distributed ZnO nano-array on cordierite honeycomb substrate with diameter of 4.7 in. Scale bars without label: 10 μm.

Laterally scalable synthesis has been successfully demonstrated with uniformly distributed ZnO nano-arrays across the entire honeycomb substrate as shown in **Figure 6-7**, which delivers a promising achievement that could be hardly obtained via a traditional batch process. From the perspective of average growth rate, a rather important figure of merit employed in industrial processing or manufacturing, the CFS process here can be further improved to accommodate the need for much more drastically reduced growth duration. Maintaining a constant concentration of growth solution and consecutive mass transport in substrate channels are two crucial factors that ensure a fast and steady growth rate. As an effective energy source, microwave heating [22] has shown its capability of improving growth rate of ZnO 1D nanostructure array on 2D

substrates, which may be extended to practical manufacturing of 1D nanostructure based 3D devices.

6.4: Conclusion

In summary, a low-temperature hydrothermal based continuous flow synthesis was successfully conducted to integrate uniformly distributed large-scale ZnO nanorod arrays on commercial 3D honeycomb substrate with channel length up to 5 cm (2 in.). Equipped with dimensionally compatible reactor and solution flow rate, CFS technique enables growth of uniformly distributed ZnO nano-arrays across the entire substrate of 12 cm (4.7 in.) in diameter. In comparison to traditional batch process, the morphology of ZnO nanorod array achieved from CFS possessed longer average length, significantly enhanced array density in channel middle area, reduced precipitates and as high as 9 times improved precursor utilization efficiency. The results of a series of varied flow rate based CFS experiments indicated that the pumping flow rate is not only a key parameter determines distribution uniformity of ZnO nanorod array along the substrate channel, but also an essential parameter for the scale-up nanomanufacturing of monolith devices. The CFS strategy demonstrated a novel hydrothermal based approach with lower cost and higher growth efficiency to integrate ZnO nanorod arrays with 3D multi-channeled substrate, which leads to the realization of fast, low-cost and scalable manufacturing of functional 1D nanostructures based 3D devices.

Reference

1. Z. Ren, Y.B. Guo, G. Wrobel, D. Knecht, H.Y. Gao, Z.H. Zhang, P.X. Gao, *J. Mater. Chem*., **2012**, 22, 6862–6868.

2. D. Jian, P.X. Gao, W. Cai, B.S. Allimi, S.P. Alpay, Y. Ding, *J. Mater. Chem*., **2009**, 19, 970-975.

3. Z. Ren, V. Botu, S. Wang, Y. Meng, W. Song, Y. Guo, R. Ramprasad, S.L Suib, P.X. Gao, *Angew. Chem. Int. Ed.*, **2014**, 53, 7223-7227.

4. K. Zhou, X. Wang, X. Sun, Q. Peng, Y. Li, *J. Catal.* **2005**., 229, 206-212.

5. X. Xie, Y. Li, Z. Q. Liu, M. Haruta, W. Shen, *Nature*, **2009**, 458, 746-749.

6. Y. Guo, Z. Ren, W. Xiao, C. Liu, H. Sharma, H. Gao, A. Mhadeshwar, P.X. Gao, *Nano Energy*., **2013**, 2, 873-881

7. S. Wang, Z. Ren, W. Song, Y, Guo, M. Zhang, S. L. Suib, P.X. Gao, *Catal. Today*, **2015**, 258, 549-555.

8. S.Y. Chen, W. Song, H.J. Lin, S. Wang, S. Biswas, M. Mollahosseini, C.H. Kuo, P.X. Gao, S.L. Suib, *ACS Appl. Mater. Interfaces*, **2016**, *8*(12), 7834-7842.

9. S. Wang, Z. Ren, Y. Guo, P.X. Gao, *CrystEngComm*, **2016**, 18, 2980-2993.

10. J. L. Gomez, O. Tigli, *J. Mater. Sci.*, **2013**, 48, 612-624.

11. L.Y. Chen, Y.T. Yin, *Cryst. Growth Des*., **2012**, 12, 1055-1059.

12. L. Liu, K. Hong, X. Ge, D. Liu, M. Xu, *J. Phys. Chem. C*., **2014**, 118, 15551–15555.

13. K.M. McPeak, J.B Baxter, *Cryst. Growth Des*., **2009**, 9, 4538-4545.

14. K.M. McPeak, J.B Baxter, *Ind. Eng. Chem. Res.*, **2009**, 48, 5954-5961.

15. C.H. Choi, J.B. Levin, C.H. Chang, *CrystEngComm*, **2016**, 18, 8645-8652.

16. W. Xiao, Y. Guo, Z. Ren, G. Wrobel, Z. Ren, T. Lu, P.X. Gao, *Cryst. Growth Des.*, *2013*, 13, 3657–3664.

17. S. Xu, Z.L. Wang, *Nano Res*., **2011**, 4, 1013-1098.

18. M.N. Ashfold, R.P. Doherty, N.G. Ndifor-Angwafor, D.J. Riley, Y. Sun, *Thin Solid Films*, **2007**, 515, 8679-8683.

19. D. Polsongkram, P. Chamninok, S. Pukird, L. Chow, O. Lupan, G. Chai, H. Khallaf, S. Park, A. Schulte, *Physica B: Condensed Matter*., **2008**, 403, 3713-3717.

20. S. Baruah, J. Dutta, *Sci. Technol. Adv. Mater*., **2009**, 10, 013001.

21. G.Q. Zhang, H.B. Wu, H.E. Hoster, M.B. Chan-Park, X.W. Lou, *Energy Environ. Sci*., **2012**, 5, 9453-9456.

22. L. Liu, K. Hong, X. Ge, D. Liu, M. Xu, *J. Phys. Chem. C*., **2014**, 118, 15551–15555.

CHAPTER 7

Summary and Outlook

7.1. Summary

Nano-array integration, as an important functional enabling technology, has been widely employed in environmental and energy harvesting applications. Using well-defined nano-array configuration to substitute the powder catalyst on monolith shows great promise towards next generation monolithic catalysts that might be used in near-future automotive aftertreatment system. In the past few years, the development of nano-array based monolithic catalysts has been focused on rational material selection, especially on transition metal oxides, and nano-array integration strategy on 3-D substrate. As a consequence, low temperature based hydrothermal integration was developed to synthesize different 1-D transition metal oxide nano-arrays on commercial honeycomb substrates that have been used in catalytic converters. In this dissertation, we have extended the catalytically active materials from transition metal oxides to lanthanum based perovskite oxides ($LaBO_3$). 3-D perovskite nano-array was successfully fabricated by using ZnO nanorod array as a secondary support through a combination of hydrothermal growth and sol-gel deposition method. The structure and catalytic activity of as-prepared catalysts are investigated using a variety of techniques. The catalytic activity of the perovskite nano-array catalyst is investigated using propane oxidation as a probe test. It is revealed that the activity of the perovskite catalysts is strongly correlated with their nanostructures. The nano-array based perovskite catalyst shows enhanced activity and material utilization efficiency in comparison to the powder perovskite catalyst, which can be attributed to

the better dispersion of perovskite on ZnO nano-array and thus a stronger gas-solid phase interaction in propane oxidation. Noble metal incorporation significantly improves the low temperature activity of ZnO/perovskite nano-array catalysts. And the interface between different solid components during sol-gel deposition results in good hydrothermal stability of the catalysts. Further structural modification through acid treatment leads to the formation of mesoporous nanotube array of Pt loaded perovskite catalysts, which induces the evolution of surface chemistry and further improvement of low temperature activity.

In Chapter 1, the exhaust aftertreatment of automobiles is systematically introduced in the sequence of catalytic converter, monolithic catalysts and the wash-coating process that is being used to fabricate monolithic catalysts in the industry. The weakness of commercial powder based monolithic catalyst is discussed in detail. The catalytic performance and other advantages such as reduced materials usage enabled by 1-D nanostructure array are also discussed. Additionally, the principle for design of nano-array based monolithic catalyst is highlighted due to its significant importance in this dissertation.

In Chapter 2, the detail of experiment design and procedure are introduced. The integration strategy of ZnO/perovskite core/shell nanorod array is the fundament of perovskite nano-array catalysts, which requires the capability of controlling the geometric size, shape and uniformity of ZnO nano-array as well as the dispersion of perovskite nanofilm throughout entire piece of monolith. The catalytic activity investigation is also introduced in this section which includes GC and FTIR gas analysis instrumentation.

In Chapters 3-5, the detailed work and results relevant to catalysts' activity in this dissertation are discussed. ZnO/$LaMnO_3$ nano-array catalyst possesses lower light-off temperature (by 25°C), lower activation energy and reduced materials usage than powder based

perovskite catalyst. The enhanced dispersion of $LaMnO_3$ nanoparticles is studied by SEM, TEM and BET characterization. Incorporation of noble metal (Pt) is able to improve the low temperature activity of ZnO/perovskite nano-array catalyst. 0.1Pt LSMO shows lightly better activity compared to ALD-Pt LSMO catalyst with similar Pt loading amount. And the interface between three components (ZnO, perovskite, Pt) plays importance role in stabilizing the catalytic active sites during the hydrothermal aging, enabling the 0.1Pt LSMO to possess decent activity (T_{50}: 300C) for propane oxidation after aging at 800°C. Furthermore, mesoporous $LaMnO_3$/Pt nanotube array is obtained by using surface acidic etching of ZnO/$LaMnO_3$-Pt core/shell nanorods array. The nano-tube array catalyst exhibits lower light-off temperature (254°C) than its core/shell nano-array counterpart (289°C). The large surface area and as-obtained internal surface of nanotube array are kinetically favorable to gas-solid phase interaction and are hydrothermally stable in oxidation reaction. The La cations deficiency owing to acid etching is neutralized by increased surface Mn^{4+} population, which leads to more electrophilic/acidic $LaMnO_3$ support. The surface variation of $LaMnO_3$ support enables Pt nanoparticles to possess better oxidation resistance and results in more catalytically active metallic Pt in oxidation reactions.

In Chapter 6, a novel hydrothermal based continuous flow synthesis is introduced. The integration strategy shows enhanced growth rate of ZnO nanorod array, reduced raw materials usage and great potential for industrial-relevant scalable manufacturing. The special heating-cooling-filtering circulation effectively suppresses the precursor consumption from homogeneously nucleated nanoparticles and boosts the heterogeneous nano-array growth on honeycomb substrate. Scale-up integration of ZnO nano-array has been successfully demonstrated on commercial cordierite substrate.

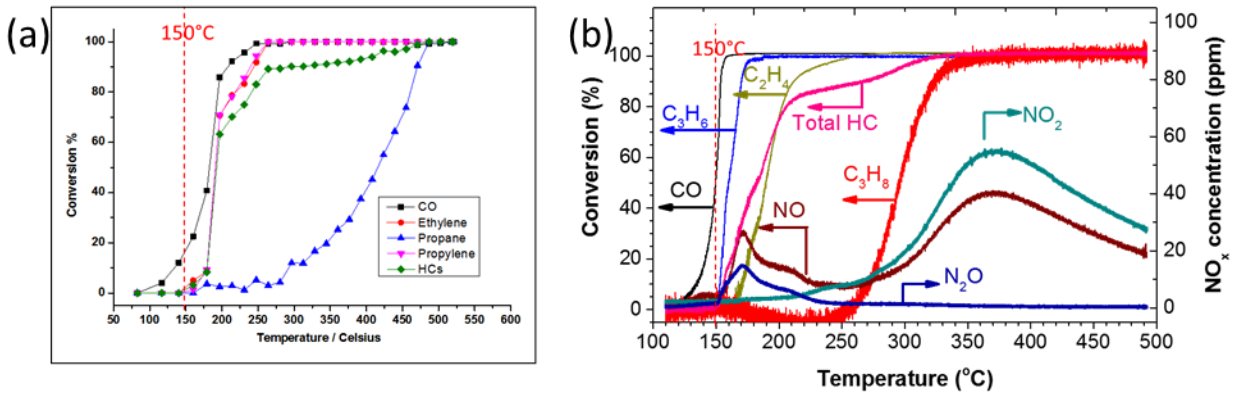

Figure 7-1. Light-off curves of (a) 5LMO-T catalyst and (b) commercial DOC catalyst tested in simulated exhaust (LTC-D mode)

Table 7-1. 90% conversion temperatures of each component in LTC-D mode

Catalysts	CO	Ethylene	Propane	Propylene	HCs
5LMO-T	207°C	243°C	470°C	238°C	296°C
Commercial	154°C	170°C	323°C	212°C	268°C

Shown in **Figure 7-1** is the catalytic performance of 5LMO-T nanotube array catalyst and commercial catalyst tested in low temperature oxidation-diesel mode (LTC-D). Both catalysts do not meet the requirement of 150°C challenge, especially for the conversion of total hydrocarbons (HCs). The 90% conversion temperatures of two catalysts for all the components are summarized in **Table 7-1**. The commercial catalyst becomes active for total HCs at 268°C. And 5LMO-T becomes active at 296°C. Obviously, the activity for total HCs is greatly dependent on the activity for propane oxidation in simulated exhaust since the propane oxidation is usually

delayed compared to other hydrocarbons. The commercial catalyst becomes active for propane oxidation in simulated exhaust at 323°C, which is much lower than that of 5LMO-T (470°C). The higher T_{90}s of 5LMO-T indicate that the low temperature catalytic activity of nano-array catalyst cannot be comparable to commercial catalyst. However, the commercial catalyst possesses much higher PGMs loading (4.7 g/L) than that of 5LMO-T (2.5 g/L), which indicates the nano-array catalysts are holding the potential to reduce the noble metal usage while pursuing the low temperature catalytic activity. The work we have finished by now poses a guideline to manipulate the catalytic activity of perovskite nano-array based catalysts and a feasible approach to improve the materials utilization efficiency.

In summary, this dissertation develops a new type of 3-D perovskite nano-array based monolithic catalysts by rational material selection and structural modification for automotive emission control purpose. It also presents the potential scalable manufacturing route to bridge the laboratory demonstration to industrial practical application of nano-array based monolithic catalysts.

7.2. Outlook and Suggestion

In light of the 150°C challenge and the current experiment result of catalytic activity, ZnO/perovskite nano-array based monolithic catalysts is still lack of required low temperature activity for hydrocarbons oxidation. Even though this weakness can be improved by incorporating noble metal into the material system, 90% conversion at 150°C is still a huge challenge since noble metal is lack of strong interaction with perovskite materials. Single atom catalyst and bimetallic noble metal catalyst are drawing attention due their exception activity toward hydrocarbon oxidation. Highly dispersed noble metal atoms on support materials

represent a unique type of catalysts with high noble metal utilization efficiency and exceptional catalytic activity for oxidation reaction. Moreover, Pd is more active for hydrocarbons oxidation and less expensive than Pt. Using palladium (Pd) to partially substitute Pt is also an effective method to lower the cost the catalysts. However, improving the stability of Pd based catalysts maintains a challenging work. Thus, to further increase the activity of perovskite nano-array catalysts and reduce the noble metal usage at the same time, the following work of Pt incorporate perovskite nano-array catalysts should be focusing on: (1) enhancing the dispersion of noble metal nanoparticles on perovskite by reducing the size of Pt cluster, (2) exploring the interaction between different noble metals (Pt, Pd) to compensate the poor activity of perovskite for low temperature hydrocarbons oxidation, (3) study the hydrothermal stability and sulfur-poisoning resistance of Pt/Pd based catalysts.

Additionally, though the surface area of perovskite can be increased by using nano-array configuration and diluted acid treatment, it still cannot be compatible to commercial powder-form monolithic catalysts. The poor surface area is a major hurdle for design of high-efficiency perovskite catalysts in emission reduction. To increase the surface area of perovskite based catalysts, one can manipulate the perovskite coating and the nano-array architecture simultaneously because the particle size, geometric size of nano-array and uniformity of coating significantly influence the surface area. The best scenario should be monolayer perovskite coating with controlled average particle size on densely packed ZnO nanorod array with average diameter lower than 50 nm. However, the correlation between catalytic activity of nano-array catalysts and their average length-diameter ratio is unknown. Thus, a detailed study should be carried out to construct the parameters which may potentially affect the catalysts' activity, such as average length, average diameter, and thickness of perovskite coating. The future work of

perovskite based catalysts can be focused on: (1) shrinking the nanoparticle size of perovskite by tuning the original precursors concentration of sol-gel solution; (2) increasing the aspect ratio of perovskite nanotubes through reducing the average diameter of ZnO nanorods by adjusting the reaction condition in hydrothermal synthesis; (3) developing other metal oxide supports with high surface area; (4) study the correlation between catalytic activity of nano-array catalysts and geometry parameters.

The integration strategy of continuous flow synthesis does not include the perovskite deposition step. The laboratory scale demonstration has not yet been demonstrated to be feasible for scalable manufacturing. Uniform coating of perovskite on nano-array will be more and more difficult to achieve when the dimension of substrate becomes larger and larger. It is essential to develop suitable deposition method and compatible setup for perovskite loading. The viscosity and concentration of sol-gel solution should play an important role in obtaining uniform coating on nano-array integrated commercial honeycomb cordierite. Due to the toxicity and high price of dimethylformamide solvent, following work should include seeking for substitution organic solvent for perovskite deposition.

RESUME

Summary

- Highly self-motivated and innovative researcher with excellent problem-solving capability and team spirit.
- Extensive experience in nanomaterials synthesis, characterization, formula optimization and functional device fabrication.
- Strong skill in handling various analytical instrumentations and performing experiment design, data collection and result analysis.

Education

Ph.D. candidate in Materials Science and Engineering (GPA: 3.91/4.0)

University of Connecticut, Storrs, CT August 2012 - Present

B.S. in Materials Science and Engineering (GPA: 3.5/4.0)

Jilin University, Changchun, Jilin, P.R. China Sep 2007 - June 2011

Professional Experience

University of Connecticut Graduate Research Assistant August 2012-present

Projects:

- Metal Oxide Nano-array based Catalysts for Low Temperature Diesel Oxidation (DOE sponsored).
- Scalable and Sustainable Hydrothermal Manufacturing of Nano-array based Low Temperature Diesel Oxidation Catalysts (NSF sponsored).

Responsibility:

- Design and synthesis of high-performance metal oxide nano-array based catalysts and functional devices for diesel oxidation, diesel particulate filtration, lean NO_x trapping.
- Characterization of nano-size metal oxides catalysts using various techniques (SEM, TEM, FIB, XRD, BET, XPS, etc.)
- Catalytic performance test, thermal and hydrothermal stability test and data analysis of various nanostructured catalysts.
- Development of scalable and automation manufacturing protocol of nano-array based devices for various environmental and energy applications.

Professional Skills

- Expert in heterogeneous nanocatalysts synthesis, characterization and formula screening for automotive exhaust reduction.
- Expert in large scale metal oxides nano-array integration, thin film deposition on various 2-D and 3-D substrates.
- Experience in design and prototype of scalable automation manufacturing system for functional nano-array devices.
- Four-year experience in operating electron microscopes including SEM, TEM for structure and composition analysis of nanomaterials.
- Experience in various experimental instrumentations including FTIR, GC-MS, Chemisorption Analyzer, XRD, Radio-frequency Magnetron Sputtering.
- Excellent experiment design and data analysis capability, and proposal writing skill.

Professional Internship Activities

- University of Connecticut Technologies Incubator Program-Bioscience, Entrepreneurship & STEM Summer Intern, 05/2016-07/2016
- Part-time Internship at 3D Array Technology LLC, Farmington, CT, 10/2015-04/2016

Honors and Awards

- Kokes Awards, North American Catalysis Society, 2017
- Doctoral Dissertation Fellowship, University of Connecticut, 2016.
- FEI Graduate Fellowship, University of Connecticut, 2015.
- First place, Student Speaking Contest, ASM Hartford Chapter's Student Night, Storrs, 2015
- First place, Basketball Tournament Championship, University of Connecticut Chinese Student and Scholar Association (CSSA), Storrs, 2013
- Excellent Student Leadership Award, Jinlin University, China, 2011
- College Undergraduate Scholarship, Jilin University, China, 2008-2010
- Excellent Student Award, MS&E Department, Jilin University, China, 2008

Conference Presentations

1. **S. Wang**, S. Du, W. Tang, P.X. Gao, "Pt Loaded Perovskite Nano-Array Based Monolithic Catalysts for Automotive Emission Control", 25th North American Meeting (NAM) of the Catalysis Society, Denver, CO, 06/2017. (Poster presentation)

2. W. Tang, **S. Wang**, P.X. Gao, et. al., "In Situ Constructing Nano-Sheet Array on the Cordierite Honeycomb and Its Application in Catalytic Combustion of Hydrocarbons," 25th North American Meeting (NAM) of the Catalysis Society, Denver, CO, 06/2017. (Poster presentation)

3. W. Tang, **S. Wang**, P.X. Gao, et. al., "Fabrication of Spinel Nanostructured $MnxCo_{3-X}O_4$ Sheet Array Based Monolithic Catalysts for Low Temperature Propylene and Propane Oxidation," 25th North American Meeting (NAM) of the Catalysis Society, Denver, CO, 06/2017. (Poster presentation)

4. S. Hoang, **S. Wang**, P.X. Gao, et. al., "Exceptional Low Temperature Diesel Oxidation Activity over Pt Supported TiO2 Nano-Array Integrated Monolithic Catalysts," 25th North American Meeting (NAM) of the Catalysis Society, Denver, CO, 06/2017. (Oral presentation)

5. S. Du, **S. Wang**, P. X. Gao, et. al., "Nano-Array Modified Perovskite Based Catalytic Diesel Particulate Filters for Enhanced Soot Oxidation," 25th North American Meeting (NAM) of the Catalysis Society, Denver, CO, 06/2017. (Poster presentation)

6. **S. Wang**, X.X. Lu, P.X. Gao, et. al., "Scalable Manufacturing of Metal Oxide Nano-Array Integrated Monoliths", NSF Nanoscale Science and Engineering Grantee Conference, Washington D.C., 12/12/2016. (Poster presentation)

7. M.W. Zhang, **S. Wang**, P.X. Gao, "Scalable Microwave-assisted Continuous Flow Synthesis of ZnO Nanowire Arrays on Monolithic Cordierite Substrates for Environmental Applications", MRS fall meeting, Boston, MA, 12/1/2016. (Poster presentation)

8. S. Hoang, Y.B. Guo, W.X. Tang, **S. Wang**, P.X. Gao, et al., "Exceptional Activity for Diesel Oxidation over Pt Supported TiO_2 Nano-array Based Monolithic Catalysts", MRS fall meeting, Boston, MA, 11/30/2016. (Oral presentation)

9. B. Zhang, Y. Huang, R. Vinluan, **S. Wang**, X. Lu, M.W. Zhang, J. Zheng, P.X. Gao, "Synergy Effects in Hybrid Au/Iron Oxide Nanoparticles on the ZnO Nanowire Arrays towards NO_2 Sensing at Elevated Temperature," MRS fall meeting, Boston, MA, 11/28/2016. (Oral presentation)

10. **S. Wang**, Y. Guo, P.X. Gao, "Continuous Flow Synthesis of ZnO Nano-Array integrated Monoliths", NSF Nanoscale Science and Engineering Grantee Conference, Washington D.C., 12/2015. (Poster presentation)

11. **S. Wang**, Z. Ren, Y. Guo, P.X. Gao, "3D ZnO/Perovskite core/shell nanorod array based catalyst: promising PGM-free catalyst for low temperature hydrocarbons oxidation", 250th ACS National Meeting & Exposition, Boston, MA, 08/2015. (Oral presentation)

12. **S. Wang**, Z. Ren, Y. Guo, P.X. Gao, "ZnO/Perovskite Core-Shell Nanorod Arrays Based Monolithic Catalyst for Hydrocarbon Oxidation at Low Temperature", 24th North American Meeting (NAM) of the Catalysis Society, Pittsburgh, PA, 06/2015. (Oral presentation)

13. **S. Wang**, Y. Guo, P.X. Gao, "Continuous Flow Synthesis of Cordierite based ZnO Nanorod Array with High Growth Efficiency and Geometry Tunability", MRS fall meeting, Boston, MA, 12/2014. (Poster presentation)

14. **S. Wang**, Z. Ren, P.X. Gao, "3D Perovskite/Metal Oxide Composite Nanorod Array based Monolithic Catalysts for Automotive Emission Control", 8th International Conference on Environmental Catalysis (ICEC), Asheville, NC, 08/2014. (Poster and oral presentations)

PUBLICATIONS

(1) **S. Wang**, Z. Ren, Y. Guo and P.X. Gao, "Nano-array integrated monolithic devices: toward rational materials design and multi-functional performance by scalable nanostructures assembly". CrystEngComm, 2016, 18(17), 2980-2993. (highlights, inside cover)

(2) **S. Wang**, Z. Ren, W.Q. Song, Y.B. Guo, S.L. Suib, "ZnO/Perovskite core-shell nanorod array based monolithic catalysts with enhanced propane oxidation and material utilization efficiency at low temperature," Catal. Today, 2015, 258, 549-555.

(3) **S. Wang**, Z. Ren, Y. Guo and P.X. Gao, "One-Dimensional Nanostructure-Enhanced Catalysis.", Chapter in 'The Lightest Metals: Science and Technology from Lithium to Calcium', Encyclopedia of Inorganic and Bioinorganic Chemistry, edited by Timothy P Hanusa, John Wiley & Sons, Ltd, (2015).

(4) **S. Wang**, Y. Wu, P.X. Gao et al., "Scalable Continuous Flow Synthesis of ZnO Nanorod Arrays in 3D Ceramic Honeycomb Substrate for Low Temperature Desulfurization," CrystEngComm, 2017, accepted.

(5) **S. Wang**, P.X. Gao, et al., "Enhanced Metallic Nano-Pt Dispersion on Mesoporous Perovskite Nanotube Arrays for Efficient Low Temperature Propane Oxidation,". 2017, in submission.

(6) A. Piyadasa,***** **S. Wang**,***** P.X. Gao, "Band Structure Engineering of Semiconductor Nanowires and related Nanostructures: A Review," Semicond. Sci. Technol., 2017, DOI: 10.1088/1361-6641/aa6778. (***** equal contribution)

(7) Q.S. Liu, **S. Wang**, P.X. Gao, et al., "Highly sensitive Mg-doped ZnO film based UV-assisted NO detector at room temperature," Nanoscale. 2017, in revision.

(8) S. Du, **S. Wang**, P.X. Gao, et al., "ZnO/perovskite composite nano-array based structured catalysts for low temperature passive regeneration of diesel particulate filters", 2017, to be submitted

(9) Z. Ren, V. Botu, **S. Wang**, Y. Meng, W. Song, Y. Guo, R. Ramprasad, S. L. Suib and P. X. Gao, "Monolithically Integrated Spinel $M_xCo_{3-x}O_4$ (M=Co, Ni and Zn) Nano-Array Catalysts: Scalable Synthesis and Cations Manipulation for Low Temperature Catalytic CH_4 and CO Oxidation," Angew. Chem. Int. Ed., 2014, 53, 7223-7227.

(10) S.Y. Chen, W. Song, H.-J. Lin, **S. Wang**, S. Biswas, M. Mollahosseini, C.-H. Kuo, P.X. Gao, S. Suib, "Manganese Oxide Nanoarray-Based Monolithic Catalysts: Tunable Morphology and High Efficiency for CO Oxidation," ACS Materials & Interfaces, 8 (12), 2016, 7834–7842.

(11) S. Du, W. Tang, Y. Guo, A. Binder, E.A. Kyriakidou, T.J. Toops, **S. Wang**, Z. Ren, S. Hoang, P.X. Gao, "Understanding low temperature oxidation activity of nano-array based monolithic catalysts: from performance observation to structural and chemical insights," Emission Control Science and Technology, 2016, 1, 18-36.

(12) W. Tang, Z. Ren, X. Lu, **S. Wang**, Y. Guo, S. Hoang, S. Du and P.X. Gao, "Controlling redox reaction between $KMnO_4$ and $Co(NO_3)_2$ for scalable integration of highly uniform $MnxCo_{3-x}O_4$ nano-sheet array onto ceramic monolithic substrates." ChemCatChem, 2017, DOI:10.1002/cctc.201700795.

(13) B. Zhang, R. Vinluan, **S. Wang**, X. Lu, W. Tang, Z. Ren, J. Zheng, P.X. Gao, "Toward Ultra-sensitive and Selective NO_2 Detection in Multi-gas Mixture Stream at Elevated

Temperature using Polycrystalline Au Nanoparticles Sensitized ZnO Nanorod Arrays," 2017, to be submitted.

(14) S. Du, W. Tang, X. Lu, **S. Wang**, Y. Guo, P.X. Gao, "Cu-supported ZnO Nanoarray Integrated Structured Catalysts for Low-pressure CO_2 Hydrogenation to Methanol," 2017, Adv. Mater. Int., in submission.

(15) S. Du, P.X. Gao, Y. Guo, **S. Wang**, "Nano-array integrated honeycomb monoliths as gasoline and diesel particulate filters," 2017, US Provisional Patent application, 3D Array Technology LLC.

(16) P.X. Gao, **S. Wang**, "Perovskite-Pt nanotube array based monoliths," 2017, US Provisional Patent application, University of Connecticut.